A MEASUREMENT OF THE TAU LIFETIME IN e^+e^- ANNIHILATIONS AT HIGH ENERGIES

John McCardle

Imperial College, London

A thesis submitted for the degree of Doctor of Philosophy

of the University of London

May 1985

ABSTRACT

The tau lifetime has been measured in e^+e^- annihilations at a mean centre of mass energy of 42.5 GeV using the TASSO detector at the PETRA storage ring at DESY.

The installation of a high resolution pressurized drift chamber close to the interaction region enabled increased precision in measuring the lifetime. The design, construction, calibration and performance of this detector are described. In addition, a general description of the TASSO detector and data reduction procedures are given.

The lifetime is found to be $(2.7 \pm {}^{0.7}_{0.6} \pm 0.5) \times 10^{-13}$ s. The charged weak tau coupling constant relative to that of the muon is found to be $G_\tau/G_F = 1.04 \pm {}^{0.24}_{0.28} \pm 0.20$, in good agreement with lepton universality.

ACKNOWLEDGEMENTS

The successful completion of this project would not have been possible without the combined efforts of a number of people.

In particular, I wish to thank David Garbutt my supervisor for his encouragement during my post-graduate research and his careful reading of this manuscript. I also wish to thank Brian Foster for his help and advice during my stay at TASSO.

I am grateful to David Saxon whose work on vertex constraint methods provided an important basis to this analysis. I should also like to thank David Binnie for his guidance and support throughout this project.

Finally, I should like to thank my colleagues in the TASSO collaboration for an enjoyable stay in Hamburg.

CONTENTS

LIST OF TABLES

LIST OF FIGURES

Chapter 1

INTRODUCTION

The study of electron positron annihilations has provided a wide range of new experimental results in particle physics. The basic annihilation process and subsequent production of point-like charged spin ½ quarks or leptons is described by the theory of quantum electrodynamics (QED). This theory is capable of making predictions for cross sections to an accuracy that exceeds experimental uncertainty. Consequently, a good way to search for new charged quarks and leptons, and to study any deviations from QED prediction is particle production via e^+e^- annihilation.

1.1 PAIR PRODUCTION

The simplest production process is lepton pair production (electron, muon, tau) represented by the annihilation diagram shown in Figure 1.1a. The electromagnetic interaction is mediated by the exchange of a virtual photon, the concept on which QED theory is based.

The differential cross section predicted for this process to the lowest order in α, the electomagnetic coupling constant, after neglecting threshold factors for the masses of the final state particles which are negligible at PETRA beam energies, is given by:

$$d\sigma / d\Omega = Q^2 \alpha^2 (1 + \cos^2 \theta) / 4 s$$

where s is the square of the centre of mass energy, θ is the angle between the incoming positron and the outgoing positive charged particle, and Q is the charge of the particles. The total cross section for muon and tau pair production (Q = 1) after integrating the above expression over θ is given by:

$$\sigma = 4 \pi \alpha^2 / 3 s$$

If s is expressed in GeV^2 and σ in nanobarns, the total cross section is given by:

$$\sigma = 87.6 / s \quad nb$$

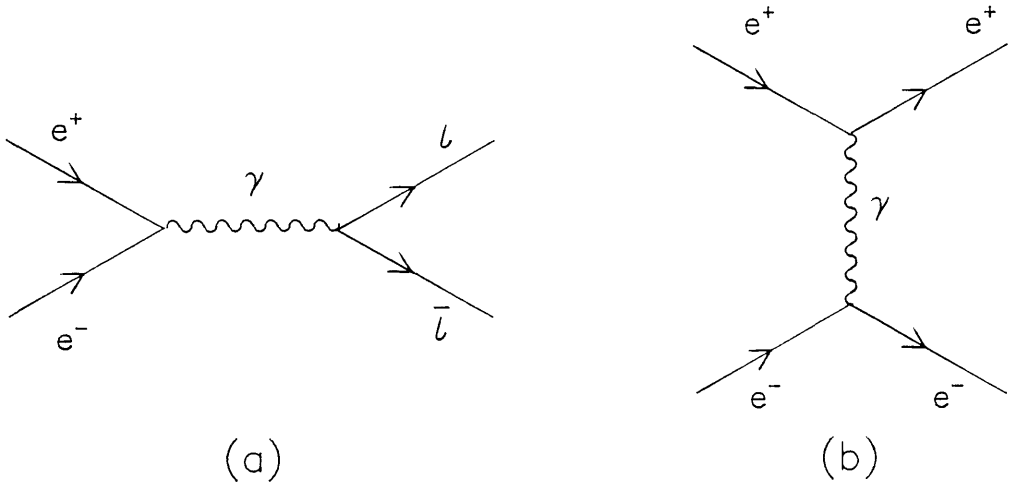

Figure 1.1: One Photon Annihilation and Scattering Diagrams

When the final state particles are also an electron positron pair (Bhabha scattering), there is another diagram, shown in Figure 1.1b, which contributes to the process. The incoming electron positron pair can scatter instead of annihilating. Consequently, the cross section is much larger than that for muon pair production and is very strongly peaked in the forward direction, as the major contribution is scattering through a small angle (θ).

1.2 RADIATIVE CORRECTIONS

So far, only the lowest order diagrams have been considered, those with the exchange of a single virtual photon. However, when comparing experimentally measured cross sections to theory, corrections from higher order diagrams need to be considered. These higher order diagrams, some of which are shown in Figure 1.2, arise from the emission of real photons (Figure 1.2a), virtual photons (Figure 1.2b), and vacuum polarisation (Figure 1.2c) into electron, muon, tau or quark pairs. The largest of these radiative corrections is due to initial state radiation before the e^+e^- annihilation. This has the effect of lowering the centre of mass energy and hence increasing the measured cross section due to its $1/s$ dependence. As the size of these corrections are dependent on the direction of the final state particles and the resulting detection efficiency for a given direction, the correction factor is obtained from a Monte Carlo program where

events are generated with the appropriate radiative spectrum and then passed through a detector simulation program. Typically these radiative corrections are of the order of 10 % of the contribution from the lowest order diagrams.

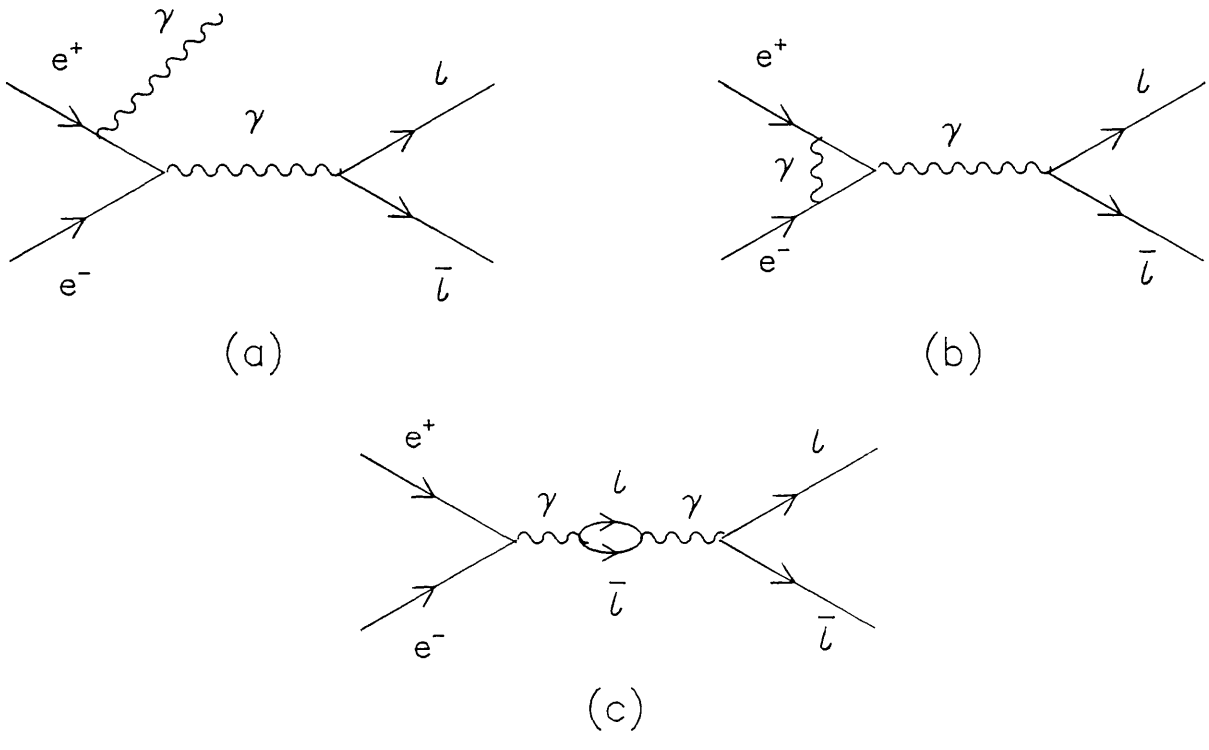

Figure 1.2: Radiative Correction Diagrams

1.3 OTHER PAIR PRODUCTION PROCESSES

There does not have to be an e^+e^- annihilation to produce additional final state particles. Lepton or quark pair production can occur via the two photon collision reaction shown in Figure 1.3. Usually, the colliding electron and positron are scattered through a small angle with only a

small energy transfer to the virtual photons. Hence the energy available for the production of the lepton pairs or the hadronic system is only a small fraction of the total beam energy.

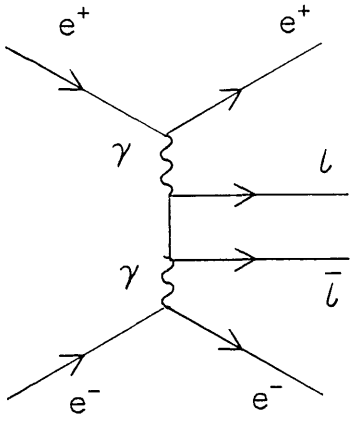

Figure 1.3: Two Photon Collision Diagram

So far only production processes due to the electromagnetic interaction have been described. However, the standard theory of weak interactions predicts a weak neutral current contribution to the lepton pair production process via the exchange of a virtual Z^0. At PETRA energies the deviation in the cross section from QED prediction is too small to be experimentally noticeable. However, a forward backward asymmetry (relative to the colliding beams) is introduced into the muon pair differential cross section, where the μ^- is produced preferentially in the opposite direction to the electron beam. This asymmetry has been observed at PETRA energies. Weak interactions will be considered further in Chapter 4 when discussing the theory concerning tau lepton decay.

1.4 HADRON PRODUCTION

The production of hadrons in e^+e^- annihilations can be described by the quark model. A quark anti-quark pair is produced via the single photon annihilation diagram in a similar manner to the muon pair production described earlier, and subsequently fragments into hadrons. The expression for the total cross section for quark pair production is similar to the muon pair cross section except that the differing quark charges (Q) and the three quark colours have to be taken into account. The ratio (R) of the hadronic cross section to the muon pair cross section is given by:

$$R = \frac{\sigma(\text{hadron})}{\sigma(\mu^+\mu^-)} = 3 \sum_{q=d,u,s,c,b} Q_q^2$$

At PETRA energies, the five observable types of quark are (d, u, s, c, b) with charges (-1/3, 2/3, -1/3, 2/3, -1/3) which give a value of $R = 11/3$.

In the search for the sixth quark (top), there has been an energy scan at PETRA with increasing available centre of mass energy. There will be enhancements in the value of R at the top quark pair bound state energies and a permanent step of 4/3 in the value of R at an energy where particles that contain one top quark are produced.

Corrections to the experimentally observed value of R need to be made to take account of hadron production from

tau decay and from two photon collision processes. In addition, the prediction for the hadronic cross section needs to be modified as the quarks can emit gluon bremsstrahlung. In the theory of quantum chromodynamics (QCD), gluons mediate the quark interactions. The first order QCD radiative correction to the R value is given by:

$$R_{QCD} = R \left(1 + \alpha_s/\pi \right)$$

where α_s is the strong interaction coupling constant.

1.5 HADRON FRAGMENTATION

At centre of mass energies high above the threshold for quark pair production, hadronic events are observed containing two back-to-back isolated cones of particles (jets). Events with three hadron jets have also been observed. The mechanism for the fragmentation of the primary quark pair into these jets is not fully understood. However, various fragmentation models exist that suppose that further quark pairs are produced in the field between the primary quark pair. These quarks and anti-quarks subsequently combine to form hadrons with the short lived hadrons decaying into secondary particles. Thus a jet of particles is formed in the direction of the two primary quarks. The explanation for the observation of a third jet is the radiation of real gluon Bremsstrahlung by one of the primary quarks, with the gluon also fragmenting into a hadron jet.

The details of the fragmentation process, such as the type of secondary quarks produced and the momentum distribution of the fragmentation products relative to the primary quark direction, are represented by free parameters in Monte Carlo simulations. By altering these free parameters to produce Monte Carlo events that describe the observed data, it is hoped to find some understanding of the fragmentation process and make comparisons between the data and QCD predictions.

Chapter 2

THE EXPERIMENT

The data for this analysis were obtained with the TASSO detector at the PETRA (Positron Electron Tandem Ring Accelerator) storage ring at DESY in Hamburg, West Germany.

2.1 PETRA

The construction of the 2.3 km PETRA ring (see Figure 2.1) was completed in autumn 1978. The four experimental detectors are situated in the four short straight sections. The four longer straight sections contain the radio frequency (r.f.) accelerating cavities.

The electrons are accelerated to 50 MeV in a linear accelerator LINAC I and then injected into the synchrotron DESY to be further accelerated to the 7 GeV PETRA injection energy. In LINAC II, a low energy electron beam strikes a tungsten target, the positrons that are produced in the electromagnetic shower are accelerated to 400 MeV and accumulated in the PIA (Positron Intensity Accumulator). Then, like the electrons, they are transferred to DESY for acceleration to 7 GeV and injected into PETRA.

When the current of the electron and positron beams accumulated in PETRA is around 4 mA, the beams are accelerated

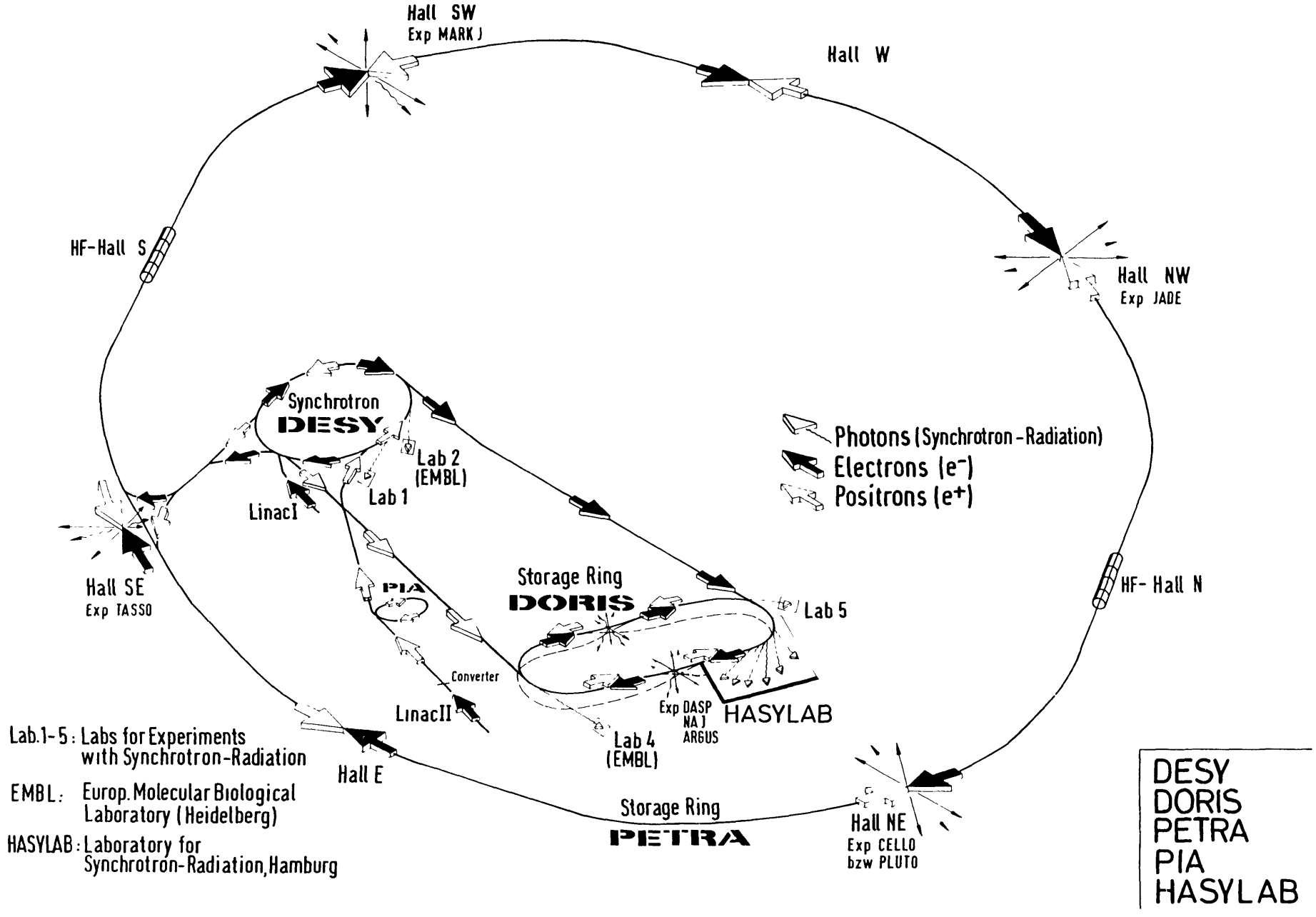

Figure 2.1: Layout of the PETRA Ring

to the required energy. PETRA operates in a bunch mode, the two bunches of electrons and two bunches of positrons circulate around the ring in opposite directions and collide at the centre of the four experimental regions.

Until 1982, the maximum centre of mass energy (W) obtainable was 36.8 GeV. The energy is limited by the power of the r.f. cavities which must replace the energy lost in the synchrotron radiation that the electrons radiate when under circular acceleration. Since 1982, the r.f. power and the number of accelerating cavities have been doubled.

The performance of the accelerator is measured by the average luminosity delivered per day. With a luminosity (L) of the colliding beams, the event rate (R) for a reaction with cross section (σ) is given by:

$$R = \sigma L$$

The luminosity for head on collisions can be expressed in terms of the beam parameters:

$$L = f B n^- n^+ / 4 \pi X Y$$

where

f	is the revolution frequency of the beams.
B	is the number of bunches per beam.
n^-,(n^+)	is the number of electrons (positrons) per bunch.
X ,(Y)	is the standard deviation of the horizontal (vertical) particle distribution in the bunch.

As all these beam parameters cannot be measured accurately enough, the luminosity is calculated from the rate of Bhabha scattering ($e^+e^- \rightarrow e^+e^-$) at small angles and hence small 4-momentum transfer (q^2). The cross section for this process is relatively large, is calculable using QED and has been experimentally well tested in this low q^2 region.

In 1982, when the machine was running with W = 34.0 GeV for many months, an integrated luminosity of 400 nb^{-1} per day was collected, (1 $nb^{-1} = 10^{33}\ cm^{-2}$). However, in scanning mode, where the energy was increased in steps of 0.030 GeV between W = 39.8 GeV and W = 45.2 GeV, each experiment collected 60 nb^{-1} per energy point at an average rate of 50 nb^{-1} per day. The large decrease in luminosity is mainly due to a lack of understanding of the machine parameters which change for each new energy point. There is not enough time to optimise the machine before the energy is increased to the next point in the scan.

2.2 TASSO

The TASSO (Twin Arm Spectrometer Solenoid) experiment was designed as a general purpose detector covering the complete available solid angle around the interaction region. It is able to detect charged particles and photons and is also capable of some charged particle identification. A collaboration of over 100 physicists take part in this experiment.

The layout of the detector is shown in Figures 2.2 and 2.3. The central detector, which is used for measuring the momenta of charged particles, consists of a high precision drift chamber (vertex detector), a proportional chamber, a large drift chamber and time-of-flight counters. Around the central detector is an aluminium solenoid which produces a uniform magnetic field.

Two Hadron-Arms on either side of the coil in the horizontal plane allow charged particle identification over a wide momentum range. They consist of planar drift chambers, three threshold Cerenkov counters, time-of-flight counters and lead-scintillator shower counters.

The lead-liquid argon shower counters above and below the coil provide photon and electron identification. Proportional tube chambers outside the iron return yoke of the magnet allow the detection of muons. At either end of the detector close to the beam pipe is the luminosity monitor and forward detector. It is a system of shower and coincidence counters able to detect the electrons and positrons scattered through small angles to the beam direction.

A short description of each detector component follows below.

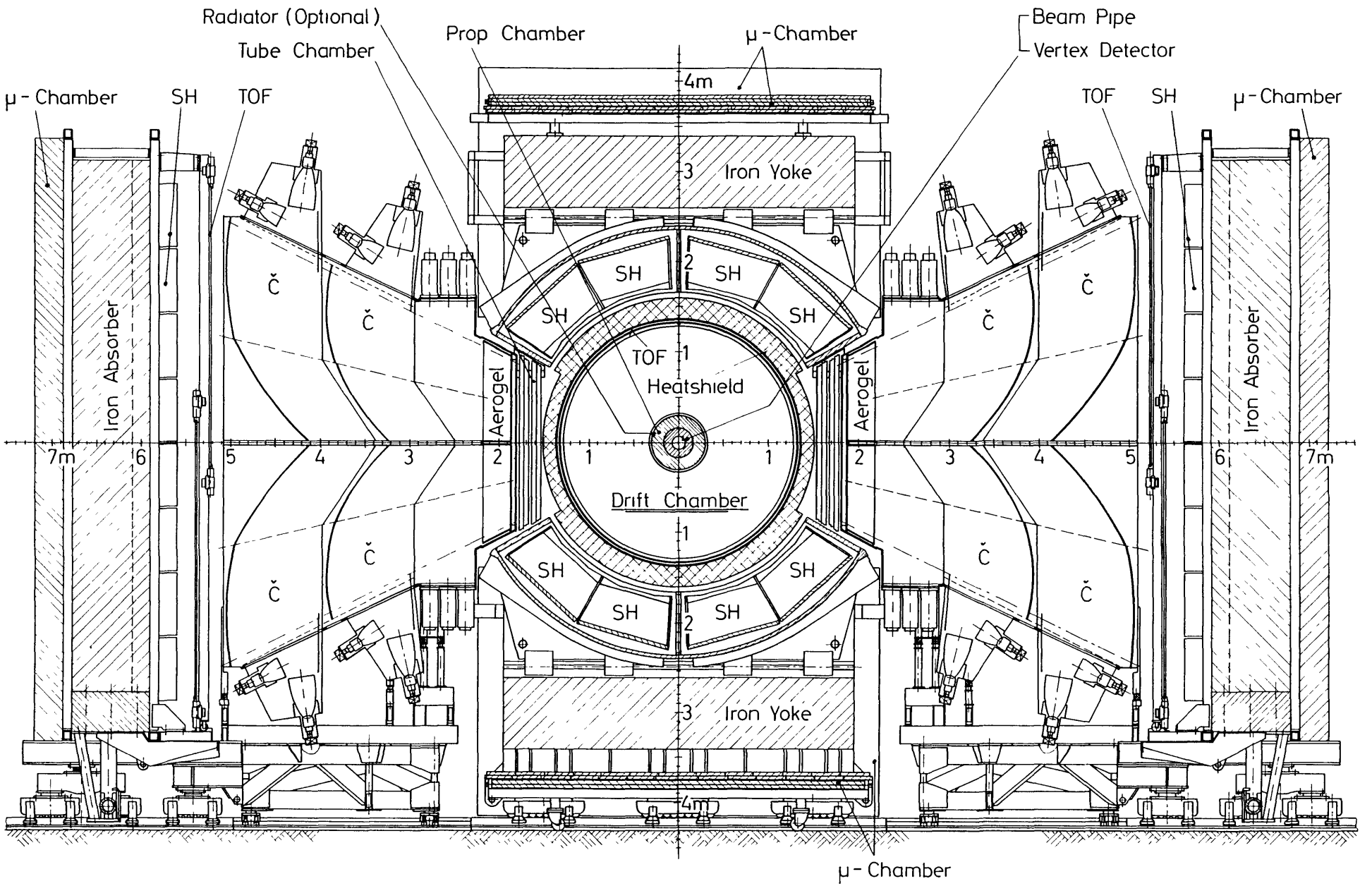

Figure 2.2: X-Y View of TASSO Detector

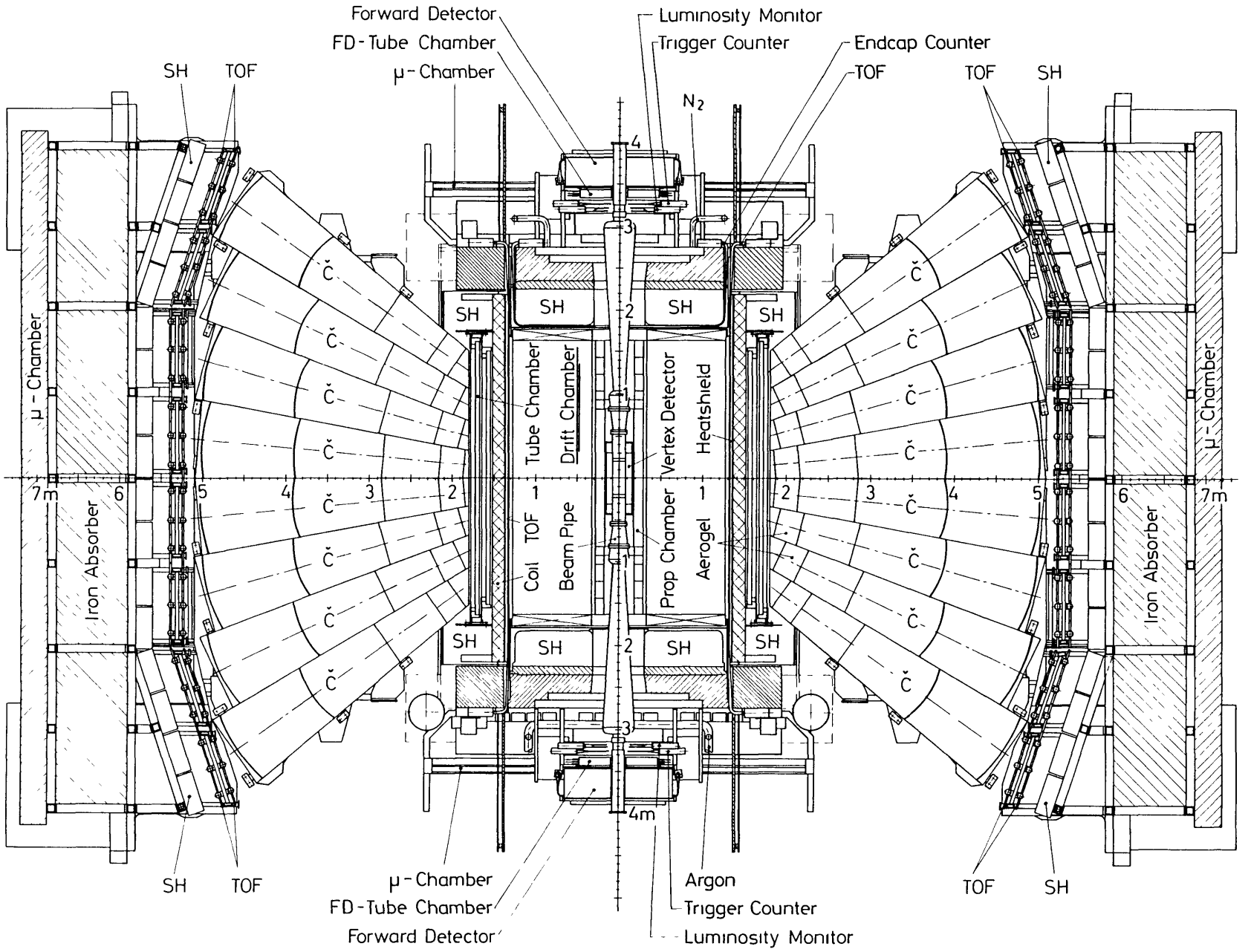

Figure 2.3: X-Z View of TASSO Detector

2.2.1 Beam Pipe and Vertex Detector

A detailed description of the vertex detector construction around the beam pipe, calibration and performance will be given in the next chapter.

2.2.2 Proportional Chamber

The cylindrical multi-wire proportional chamber /1/ (CPC) provides information used online in the experimental trigger and later offline in the charged track reconstruction. The chamber is 140 cm long with an inner radius of 18 cm and an outer radius 29 cm. There are four concentric layers of anode wires, each layer containing 480 wires mounted parallel to the beam axis. Each layer of wires lies between two cathode surfaces which consist of 120 helical strips with a 36.5° pitch angle. These strips are made by etching copper coated Kapton film. The chamber is filled with a gas mixture of 75 % Argon, 25 % Isobutane and 0.25 % Freon.

The anodes provide position information in the r-ϕ plane (see Appendix A for a description of the TASSO co-ordinate system) and have an efficiency of 98 %. The cathodes provide the z position information with a resolution of 0.35 cm and have an efficiency of 92 %. These efficiencies were measured using 2 track events by extrapolating the tracks reconstructed in the drift chamber into the CPC.

2.2.3 Drift Chamber

The cylindrical drift chamber /2/ (DC) provides the information used in the charged track reconstruction. It has an active length of 323 cm and consists of 15 concentric layers of wires 6.1 cm apart between radii of 36.6 cm and 122.2 cm. In 9 layers the sense wires are parallel to the beam axis and measure positions in the r-ϕ plane. In 6 layers the sense wires are at an angle of 4° to the beam axis to enable the z position of the track to be measured. Each of the 2340 drift cells, which consists of three field wires opposite one sense wire, has radial and azimuthal dimensions of 1.2 cm and 3.2 cm respectively. The common cell size allows the same voltage setting for each layer, all the sense wires are held at 1800 V and all the field wires at - 600 V. The chamber is filled with a gas mixture of 50 % Argon and 50 % Ethane.

The chamber is 96 % efficient with an average resolution over the whole cell of 200 μm. Tracks reconstructed just using the drift chamber have a momentum resolution of:

$$\sigma_p / p = 0.016\ p$$

where p is the momentum in the r-ϕ plane in units of GeV/c, as determined from muon pair events.

2.2.4 Inner Time of Flight Counters

Between the drift chamber and the coil at a radius of 132 cm are the 48 Inner Time of Flight scintillation counters (ITOF) /3/ covering 82 % of the total solid angle. Each scintillator is viewed at both ends by a photomultiplier connected to a discriminator. The time of flight is measured using a TDC system, the TDC stop being provided by the discriminator output and the start signal being provided by a signal from the beam pick-up probe. This probe is close to the beam axis and detects the arrival of the positron bunch.

The logical AND of the discriminator output at each end of the scintillator is used to set one of the 48 bits in the mean timer latch used in the trigger.

After offline corrections to the TDC information, the timing resolution at the end of the counters is about 270 ps and at the centre of the counters is 450 ps. Pions and Kaons can be separated in the momentum range 0.3 - 1.0 GeV/c. Protons can be separated from Pions and Kaons in the momentum range 0.4 - 1.4 GeV/c. The counters are also used to find cosmic ray tracks.

2.2.5 Coil

Between radii of 135 cm and 145 cm is the aluminium magnet solenoid coil. The coil is approximately one radiation length thick and provides a uniform field of 4.94 kG parallel to the beam axis.

2.2.6 The Hadron Arms

2.2.6.1 Planar Drift Chamber

Outside the coil are the hadron arms, the first element of which is the planar drift chamber. This consists of one layer of horizontal anode wires and vertical cathode strips. It is used to detect the position of charged particles which have travelled through the coil. A track reconstructed in the drift chamber is considered to have penetrated the coil if there is a hit in the planar chamber within three times the average multiple scattering distance from the projected track.

2.2.6.2 Cerenkov Counters

Behind the planar drift chambers are a series of three threshold Cerenkov counters /4/ covering 19 % of the total solid angle. The radiators are Silica Aerogel (n=1.024), Freon (n=1.0014), and carbon dioxide (n=1.00043), where n is the refractive index. Each counter is divided into 16 cells per arm and each cell covers an angular range $\Delta\theta$ of 10° and $\Delta\phi$ of 26°, the gas counters are further divided into half cells with $\Delta\phi$ of 13°. Light from the gas cells is focused by elliptical mirrors on to photomultipliers. In the Aerogel focussing is not a suitable method as the radiator diffuses the light, instead each cell is lined with highly reflective Millipore paper and viewed by six photomultipliers.

Pions can be separated from Kaons and Protons above momenta of 0.6 GeV/c. Kaons and Protons can be separated in the momenta ranges of 2.2 - 4.2 GeV/c and 9.3 - 17.8 GeV/c.

2.2.6.3 Hadron Arm Time of Flight Counters

Behind the Cerenkov counters at a distance of 5.5 m from the beam axis are the hadron arm time of flight counters (HTOF) /5/ covering 19 % of the total solid angle. Each HTOF consists of 48 scintillators viewed at each end by photomultipliers. Like the ITOF counters, the TDC system digitizes the time between the start signal from the beam pick-up and the stop signal from the discriminators connected to the photomultipliers.

These counters enable Pion and Kaon separation up to a momentum of 1.1 GeV/c, and Proton separation from Pions and Kaons up to a momentum of 2.2 GeV/c.

2.2.6.4 Hadron Arm Shower Counters

Behind the HTOF counters at a distance of 5.7 m from the beam axis are the shower counters /6/ for the identification of electrons and photons. They consist of stacks containing alternate layers of lead and plastic scintillator. The counters are 7.4 radiation lengths thick and cover 19 % of the total solid angle. The energy resolution is given by:

$$\sigma_E / E = 17\ \% / \sqrt{E}$$

averaged over the range $2 \leq E \leq 15$ GeV.

2.2.7 Liquid Argon Shower Counters

Above and below the coil is the liquid argon calorimeter /7/. It consists of eight separate modules covering the polar (ϕ) ranges 30° - 150° and 210° - 330°, and the azimuthal (θ) range 42° - 138°. Each module consists of a stack of thirty-five 2 mm lead plates which are separated by 5 mm gaps filled with liquid argon. The front of the stack is 179 cm from the beam axis.

The electrons and photons produce showers in the lead plates (which are 14 radiation lengths thick) causing ionization in the liquid argon. The ionization, collected by the lead plates which are at a high voltage, is proportional to the energy of the incident electron or photon. To enable position measurement of the shower, layers of printed circuit board with 2 cm wide copper strips were inserted between the plates over the first few radiation lengths. These strips enable position measurement in the ϕ and z directions. For electrons, the angular resolution was found to be $\sigma_\theta = \sigma_\phi = 2$ mrad and the energy resolution is given by:

$$\sigma_E / E = 15\ \% / \sqrt{E}$$

at E = 1 GeV.

2.2.8 Muon Chambers

Muons that penetrate the iron surrounding the detector are identified by four layers of proportional tube chambers /8/. These tubes are each 4 cm x 4 cm in cross section and contain a single wire. The wires in the two inner layers are at right angles to the wires in the two outer layers and planes of wires in the same direction have a relative shift of 2 cm. This gives a grid with 2 cm granularity and 0.6 cm resolution. The chambers cover 45 % of the total solid angle and are in six separate regions on all sides of a box surrounding the detector. The iron thickness in front of the chambers varies between 80 cm and 50 cm depending on the region of coverage.

A particle is considered to be a muon if there are hits in at least three layers within 3 standard deviations of the extrapolated track reconstructed in the cylindrical drift chamber. The error on the extrapolated position is calculated from the tracking resolution and the multiple scattering in the iron. The detection efficiency is greater than 99 % for tracks with momenta above 2 GeV/c .

2.2.9 Luminosity Monitor and Forward Detector

The forward detector and luminosity monitor /9/ are used to detect particles scattered through small angles to the beam axis and provide a luminosity measurement. There are two identical modules on either side of the central detector

covering the angular range $0 \leq \phi \leq 2\pi$ and 25 mrad $\leq \theta \leq$ 115 mrad. The modules are divided into eight sub-modules at $\Delta\phi = \pi/4$ intervals. Each module consists of a system of plastic scintillator counters, three layers of planar proportional tubes and lead-scintillator shower counters. The scintillation counter closest to the interaction point is used to define the acceptance area for the luminosity measurement. It has a smaller surface area than all the other counters and its position is accurately surveyed. Bhabha scattering events are triggered by coincidences between sets of sub-modules on both sides of the interaction region.

2.3 EXPERIMENTAL TRIGGERS

A trigger is the signal to the data acquisition computer that the apparatus is to be read out. The beam crossing rate at the interaction is 260 kHz and must be reduced by a series of triggers to 4 Hz, so that the computer has time to record the events which are of interest.

There are many different triggers in this experiment. The main ones are produced by hard-wired trigger processors reconstructing charged tracks in the central drift chamber and proportional chamber. There are other triggers, which have a smaller rate than the central detector triggers, provided by the liquid argon calorimeter, the hadron arm shower counters and the forward detector. They also provide an independent source of Bhabha scattering events and hence use-

ful in checking the efficiency of the central detectors triggers.

2.3.1 Central Proportional Chamber Processor

The CPC processor /10/ looks for radial tracks by searching for coincidences between adjacent anode planes. A coincidence occurs if the polar angular separation ϕ between the wires that are hit in the two planes is sufficiently small. If the track is coming from the origin, the acceptable separation is effectively a cut on the radius of curvature and hence the transverse momentum of the track. The minimum acceptable momentum is programed to be 220 MeV/c. The chamber is divided into 48 sectors providing 48 trigger bits. If there is an acceptable coincidence between three or more planes in a sector it is considered a track and the appropriate bit is set.

2.3.2 Drift Chamber Processor

The drift chamber processor (DC Prepro) provides track recognition for use in the trigger. The CPC 48 trigger bits, the ITOF 48 mean timer bits and hit information from six of the nine drift chamber layers used for measurements in the r-ϕ plane are combined in this track search. There is a track candidate in the drift chamber when hits are found in five out of six layers which have a curvature satisfying one of the fifteen curvature masks. A track candidate that can

be associated with an ITOF mean timer bit and one of the CPC bits is accepted as a track.

2.3.3 Central Detector Triggers

The three main triggers which used the tracking chamber information were:

1. the 'majority' trigger requiring at least four tracks found by the DC Prepro with transverse momentum greater than 320 MeV/c. This trigger was used to detect hadronic final state events.
2. the 'coplanarity' trigger requiring two DC Prepro tracks that are collinear to within 27° as defined by the set ITOF counters. Its purpose was to detect Bhabha scattering, muon pair and tau pair events.
3. the 'cathode' trigger requiring two DC Prepro tracks and an event vertex within 15 cm of the interaction point in the z direction. The z position was calculated using the information from the CPC cathodes.

2.4 DATA ACQUISITION SYSTEM

Data taking and online monitoring /11/ are performed by Norsk Data NORD 10 and NORD 100 computers respectively. When the computer receives a trigger, the data from the experiment are read out using a CAMAC system, reformatted and stored on a local disc buffer. Data on this buffer are transferred via a link to a 100 Mbyte IBM disc at the DESY

computer centre. In turn, when this disc becomes 75 % full, it is copied to a 6250 bpi tape called a dumptape.

During the 35 ms readout time, the experiment cannot detect any further events. Therefore it is important to minimise the background events which are mainly due to off beam axis particles striking the beam pipe or synchrotron radiation photons converting in the detector. As a measurement of the accelerator performance, the current drawn by the drift chamber, the noise rate in the luminosity monitor and the online measurement of luminosity are sent to the PETRA machine operators. Small changes can be made to the beam orbit which can significantly decrease the rate of background events.

The individual detector components are monitored during data taking in several ways:

1. 10 % of all events are analysed by a histogramming program which produces ADC, TDC, and wire hit distributions for the components. Any of the histograms can be displayed on a colour video monitor.
2. if the high voltage or gas supply to a component fails, data taking is inhibited and there is an audible alarm.
3. at the end of a PETRA fill (run), usually lasting two to four hours, all the histograms are printed together with the trigger rates in an end-of-run summary.

Some components are calibrated at the start and end of each data taking run for later offline corrections to the data.

2.5 EVENT RECONSTRUCTION

The data on the dumptape are mostly background events from beam-gas, beam-pipe or cosmic ray interactions. A way is needed to select events of interest using the minimum amount of computer time. A fast track finding program called FOREST is run on all events to reconstruct charged tracks in the drift chamber. Events which pass the selection criterion on these FOREST tracks are then fully reconstructed using a more accurate but much slower track-finder program called MILL.

2.5.1 FOREST Track Reconstruction

The FOREST track finding program finds tracks just using the drift chamber hit information. A linear relation (space-drift time relation) between the drift time measured and the distance of the track from the sense wire is assumed. First a circle fit in the r-ϕ plane is performed on hits found using a tree search algorithm /12/. If more than one track is reconstructed, a fit to the z information from the stereo wires is attempted. In the co-ordinates s-z, where s is the arc length of the track circle in the r-ϕ plane measured from the point of closest approach to the origin, the fit is a straight line.

2.5.2 MILL Track Reconstruction

The MILL track finding program finds tracks using information from the drift chamber as well as the CPC anodes. A non-linear space-drift time relation is used with corrections for the entrance angle of the track in the drift cell and distortions to the drift path due to the magnetic field. A circle fit in the r-ϕ plane is performed using the same tree search algorithm as FOREST to find the hits. When a track candidate is found, all the near-by hits in the drift chamber and CPC are located and fits to all possible permutations are performed to find the best possible fit. Then an s-z fit, as described for FOREST, is attempted. MILL uses a much more efficient algorithm than FOREST but the event reconstruction is a factor of forty slower.

2.6 DATA REDUCTION

The data reduction and event selection is done in a series of steps called PASS1, PASS2, PASS3, and PASS4. These steps together with the selection criteria are described below. Most of the selection criteria are based on the reconstructed track parameterisation, see Appendix A for a definition of the parameters.

2.6.1 PASS1

The FOREST program is used to process the dumptape and produce the PASS1 tape. There is no event selection.

2.6.2 PASS2

Events which satisfy the following conditions are written to a PASS2 tape:

1. events with two or more tracks fitted in the r-ϕ plane with $|d_0| \leq 2.5$ cm and at least one of the tracks reconstructed in three dimensions with $|z_0| \leq 15.0$ cm.
2. events with the luminosity counter trigger bit set.
3. events with exactly two of the ITOF 48 mean timer bits set. These counters must be opposite each other within ± 3 counters.
4. events with trigger bits set from the liquid argon or shower counters if enough energy was found deposited in the component.

Criterion (1) selects hadronic, muon pair, tau pair, two photon scattering and Bhabha scattering events. Criterion (2) selects events used to measure the luminosity. Criterion (3) selects cosmic ray events, these are useful for component calibration and efficiency measurements.

2.6.3 Two Prong

The two prong data tapes which contain events with two tracks in the final state or Bhabha scattering events are produced using the following selection conditions:

1. events must have between two and four tracks fitted in the r-ϕ plane with $|d_0| \leq 2.5$ cm and at least one of the tracks reconstructed in three dimensions with $|z_0| \leq 15.0$ cm. If there are more than two tracks, they must lie within two cones such that the angle between the tracks in a given cone is less than 5°. This selects Bhabha events which have produced showers in the beam pipe.
2. events with two tracks each with P_t less than 1 GeV/c must have opposite charge.
3. the fastest track in each cone must have the difference in their respective time of flight less than 5.0 ns as measured by the ITOF system.

Criterion (1) and (2) reduce the number of beam-gas and beam-pipe interactions. Criterion (3) selects tracks originating from the centre of the detector.

These selected events are reconstructed using the MILL track-finder.

2.6.4 PASS3

Events on the PASS2 tape are preselected using the following selection conditions before being fully reconstructed using the MILL track-finder:

1. at least three tracks fitted in the r-ϕ plane with $|d_0| \leq 2.5$ cm.
2. at least two of the tracks reconstructed must be reconstructed in three dimensions with $|z_0| \leq 15.0$ cm.

2.6.5 PASS4

In PASS4 the $e^+e^- \rightarrow$ hadron events are isolated from the others due to beam-gas interactions, beam-pipe interactions, tau pairs, Bhabhas which have produced showers, and two photon scattering. These non-hadronic backgrounds are removed from the data sample with following selection conditions:

1. the track was reconstructed in three dimensions with $|d_0| \leq 5.0$ cm and $|z_0| \leq 15.0$ cm.
2. $P_t > 0.1$ GeV/c.
3. $|\cos\theta| < 0.87$

Then only considering the tracks which satisfied the above three conditions, the event was required to have:

1. at least 5 tracks.
2. $|z_0| \leq 15.0$ cm.
3. the sum of the magnitudes of the momenta of the tracks greater than 0.265 W.

4. if there were exactly three particles in each hemisphere with respect to the sphericity[1] axis, the effective mass of either of the three particle systems assuming pion masses had to be greater than the tau mass (1.78 GeV/c^2).

These cuts remove beam-gas scattering (2,3), tau pair production (1,4), Bhabha scattering and muon pair production (1), and two photon collisions (1,3). Finally the remaining events were visually scanned. About 3 % are rejected, most of these being due to Bhabha scattering events producing showers in the material before the tracking chamber.

Table 1 shows the typical data reduction factors due to each selection procedure, starting with 12500 events on a dumptape.

---

[1] The direction of the sphericity axis is defined so that the square of the transverse momentum relative to this axis is minimized.

TABLE 1

Data Reduction Factors

Data Sample	Number of events
PASS1	12500
PASS2	2770
PASS3	220
PASS4	2
Two Prong	240

2.7 LUMINOSITY MEASUREMENT

The luminosity is determined by measuring the rate of Bhabha scattering events at small angles using the luminosity monitor /9/ and at wide angles in the drift chamber. The measurement with each component is done separately and the results are later combined /13/.

For the analysis with the luminosity monitor, the statistical error is negligible due to the large number of Bhabha events detected. However, there are a number of sources of systematic error:

1. random hit coincidences in the scintillation counters.
2. hits due to electrons showering in the material between the counters and the interaction region.

3. uncertainties in the higher order radiative corrections to the Bhabha scattering cross section.
4. uncertainties in the exact position of the scintillation counters.
5. uncertainties in the beam position and inclination.

These errors combine to give an uncertainty of 4 % on the luminosity measurement.

For the analysis with the drift chamber, Bhabha events were collected over many data taking runs. The source of systematic errors are:

1. uncertainties in the event trigger, selection and reconstruction efficiencies.
2. uncertainties in the calculation of interactions of the electrons between the beam and the drift chamber.
3. uncertainties in the higher order radiative corrections.

These errors combine to give a 5 % uncertainty on the luminosity measurement.

Chapter 3

THE VERTEX DETECTOR

3.1 INTRODUCTION

In September 1982, as part of an upgrade to the TASSO detector, the original aluminium beam pipe was removed to enable the installation of a beryllium beam pipe and high precision pressurised drift chamber (vertex detector) /14/. The aim was to increase the precision in measuring the tracks to obtain the vertex position. This was achieved by reducing the amount of material between the interaction point and the tracking chambers so that the amount of multiple scattering was decreased, and by having accurately measured space points close to the interaction region.

With the ability to locate an event vertex to the order of a millimetre, it becomes possible to detect short lived particles with lifetimes around 10^{-13} seconds. This enables the study of the decays of the tau lepton and mesons containing charm or bottom quarks.

In this chapter the design, construction, calibration and performance of the vertex detector will be discussed.

3.2 BEAM PIPE

In addition to being part of the PETRA vacuum system, the beam pipe forms the inner wall of the vertex detector. The pipe must be leak tight as a vacuum of 10^{-9} torr is needed within PETRA to reduce beam absorption and to keep the noise hits in the drift chambers, due to beam gas scattering, at a reasonable rate. The pipe material should be the smallest number of radiation lengths in thickness but also as absorbent as possible to the background synchrotron radiation. It must be strong enough to withstand the 3 bar pressure within the detector and must not buckle under the 2.5 kN tension of all the wires. The metal beryllium with its low atomic number (Z = 4) and its high strength has all these properties except that it is almost transparent to low energy photons.

A pipe of 6.5 cm radius was constructed from a 1.8 mm thick sheet of beryllium. The chosen radius was considered the smallest possible in order to keep the background noise in the chamber from synchrotron radiation and off-beam axis particles acceptable. In order to reduce the background flux of synchrotron photons, collimators were installed several metres from the interaction region. However, reflected photons from Compton scattering in the collimators could enter the chamber. This low energy flux of photons was attenuated by a 15 μm layer of copper that had been deposited on the inner surface of the beam pipe but results in a flux of 8 keV pnotons from copper fluorescence.

In case this copper fluorescence caused excessive background in the chamber, a small compartment 6.4 mm in thickness was built around the beam pipe. The wall of this compartment was a cylinder of Kapton glued to the larger diameter end sections of the beam pipe. This compartment if filled with xenon at 3 bar would absorb most of these 8 keV photons but would increase the thickness of the pipe from 0.6 % to 0.85 % of a radiation length. The use of the xenon chamber has so far been unnecessary.

3.3 CHAMBER DESIGN

The inner and outer radii of the vertex detector were constrained by the space available between the beam pipe and the inner radius of the CPC at 18 cm, as is shown in Figures 3.1a and 3.1b.

The 57 cm active length of the detector was chosen to match the polar angular acceptance of the CPC and the cylindrical drift chamber.

The number of sense (anode) wires per layer must be large enough to enable measurements on individual tracks in hadron jets or a tau lepton decay. However, the total number of wires is limited by the space available for connection of the high voltage and electronic readout cables. Measurement over the longest possible length of track was achieved by having two groups of drift cells. Each group consisted of 4 layers of wires, the group close to the beam pipe had 72

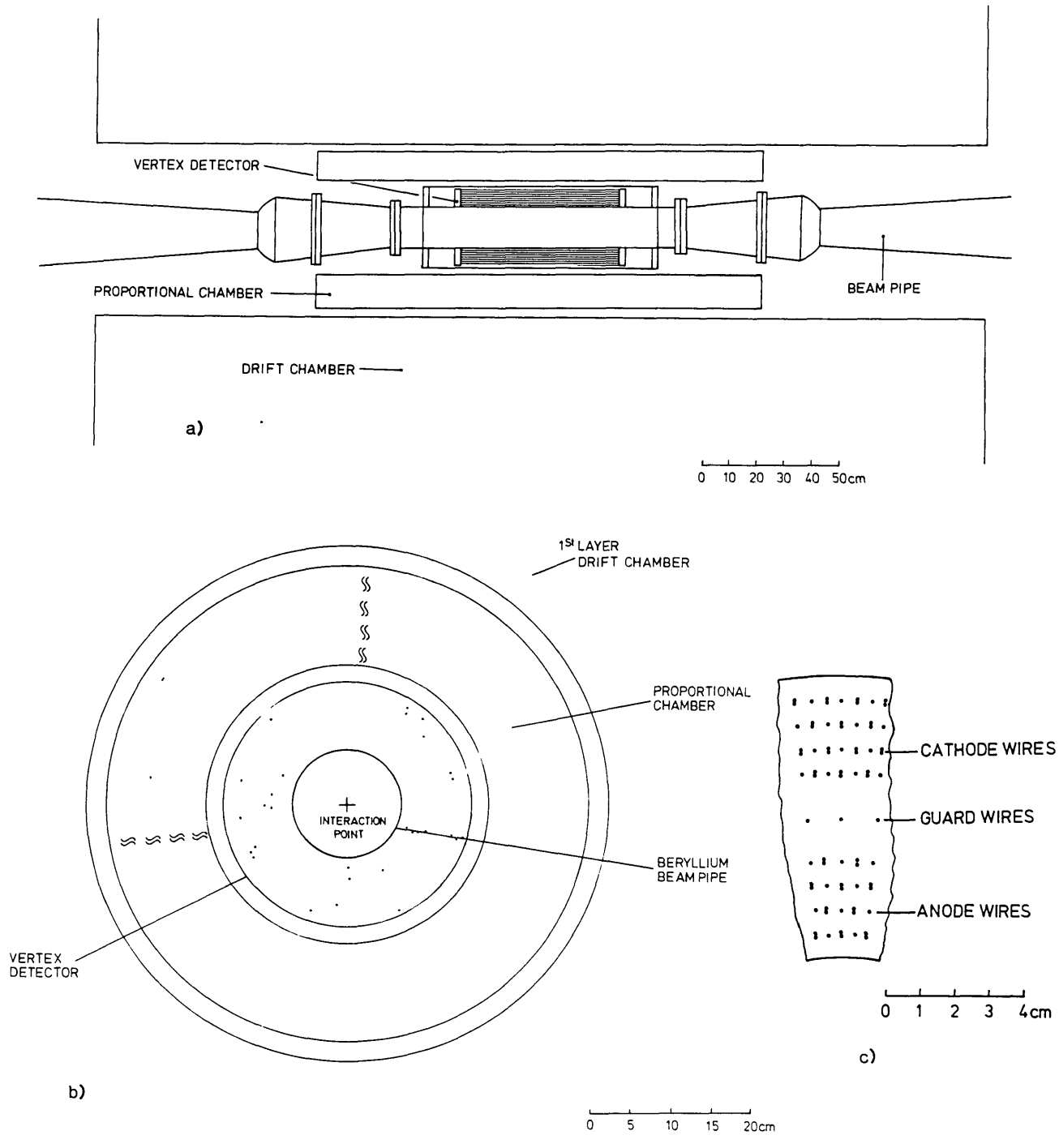

Figure 3.1: (a) Y-Z View (b) X-Y View (c) Drift Cell Design

sense wires per layer and the group close to the outer wall of the chamber had 108 sense wires per layer. Figure 3.1c shows the design of these drift cells and Table 2 gives the radii of the planes together with the maximum drift distance.

TABLE 2

Sense Wire Parameters

Radius of sense wire planes (cm)	Number of sense wires	Maximum drift distance (cm)
8.1	72	0.353
8.8	72	0.384
9.5	72	0.415
10.2	72	0.445
12.8	108	0.372
13.5	108	0.393
14.2	108	0.413
14.9	108	0.433

The choice of drift cell was motivated by the fact that for good timing resolution only those electrons produced around the point of closest approach of the track to the sense wire should be collected. Better localization in the electron collection is achieved with a pair of closely

spaced field (cathode) wires than with a single wire. The electrostatic forces are only radial and any radial movement of the sense wires does not cause a significant worsening in resolution.

The sense wires that register the hits from a radial track are alternately to the left and the right of the track. This means any common offset in the timing or drift velocity determination results only in a worsening in resolution and not in the displacement of the track. Furthermore, two closely spaced tracks that went through the same cell each produce two hits in both the inner and outer groups of wires. Between the two groups of cells was a layer of guard wires to attract any stray ionization.

3.4 CHAMBER CONSTRUCTION

The inner equipotential for the chamber was formed by wrapping a sheet of 75 μm thick aluminium foil around the Kapton cylinder that was the outer wall of the xenon compartment.

The wires were to be strung between two 12 mm thick aluminium alloy and flanges. It was much more important to position the sense wires accurately in the azimuthal direction than the radial one for accurate vertex reconstruction. The key to the wire positioning was in the accurately milled radial grooves that were machined into the flanges to an accuracy of ± 10 μm. The design of the end flange is shown in Figure 3.2.

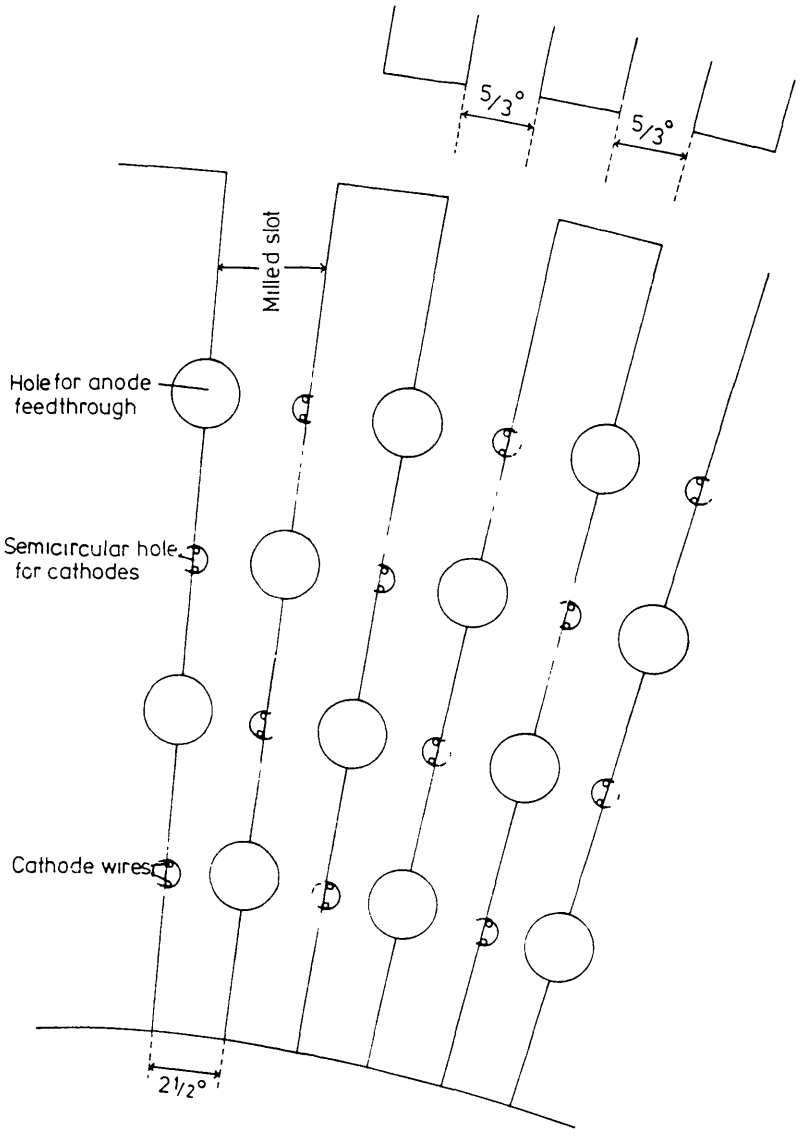

Figure 3.2: End Flange Design

The width of each groove was equal to their separation. Holes centred on the edge of the grooves were drilled for the field wires and the feed-throughs which insulated the sense wires. The holes for the field wires did not completely penetrate the plate but intersected the milled edges with a semicircular shaped hole. The feed-throughs for the sense wires were designed to allow the sense wires to be brought into the plane of the field wires by their rotation.

Each sense wire lay at the base of a v-shaped section that was eccentrically positioned by 0.2 mm within the feed-through, as is shown in Figure 3.3.

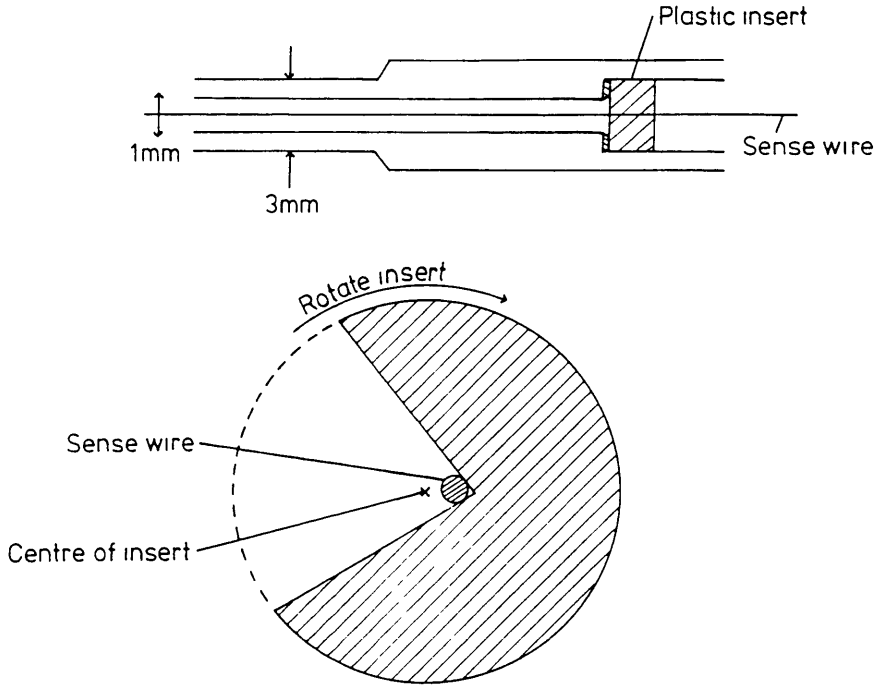

Figure 3.3: Feed-through Cross Section

As this whole procedure relied on the accuracy of the milling of these radial edges, their positions were checked. Each end flange was centred on a turntable and viewed from above through a travelling microscope at a constant distance from the centre of the plate. The distance normal to the edge from its actual position to its nominal position was measured to an accuracy of ± 2 μm. Figure 3.4 shows the results from a series of such measurement on one of the end flanges. The fact that the measurements were distributed on

a sine function with a 50 μm amplitude was explained by the plate having been mounted with its centre offset by 50 μm. Figure 3.5 shows the spread of all these measurements after removing the effects due to the plate having been offset, the grooves were milled to an accuracy of 7 μm.

The two end flanges were separated from the beam pipe with an insulating ring. The relative alignment was performed by rotating the end flanges until a groove on each flange was parallel to and the same height above an optical bench to an accuracy of ± 50 μm.

Due to a lack of space around the end flanges, the field wires were maintained at ground potential. Consequently the high voltage and readout cables only had to be connected to the sense wires, thus halving the number of connections needed to be made to the flange. The field wires were a 100 μm diameter silver plated beryllium copper alloy and the sense wires were a 20 μm diameter gold plated tungsten rhenium alloy. They were soldered under tension between the two flanges. The tension for each layer differed to allow for the bending of the flanges under the combined wire tension but at the completion of wiring, the field and sense wire tensions were 1.5 N and 0.4 N respectively.

It was important to find any slack wires after soldering, otherwise a short circuit could occur during operation of the chamber. The tensions of the wires were measured after installation by vibrating the end flange and measuring their resonant frequencies. Slack wires were replaced.

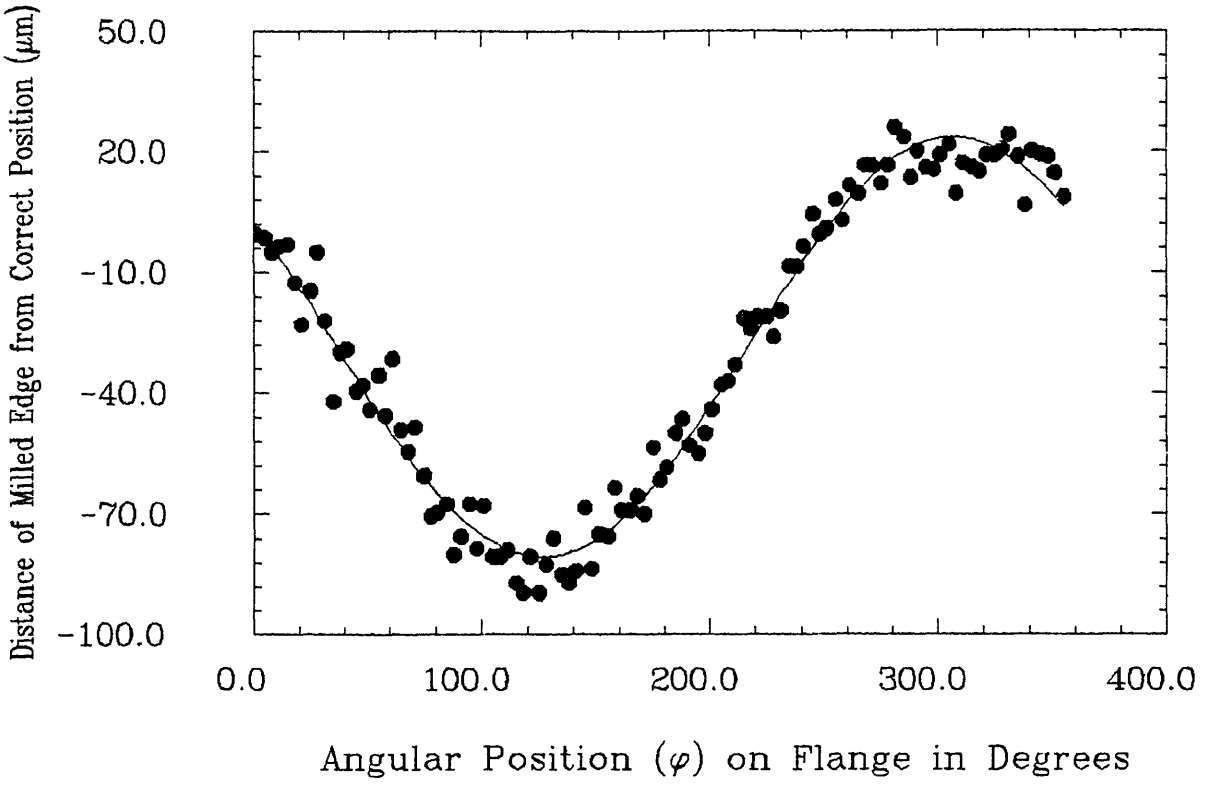

Figure 3.4: Measurements of the Groove Positions

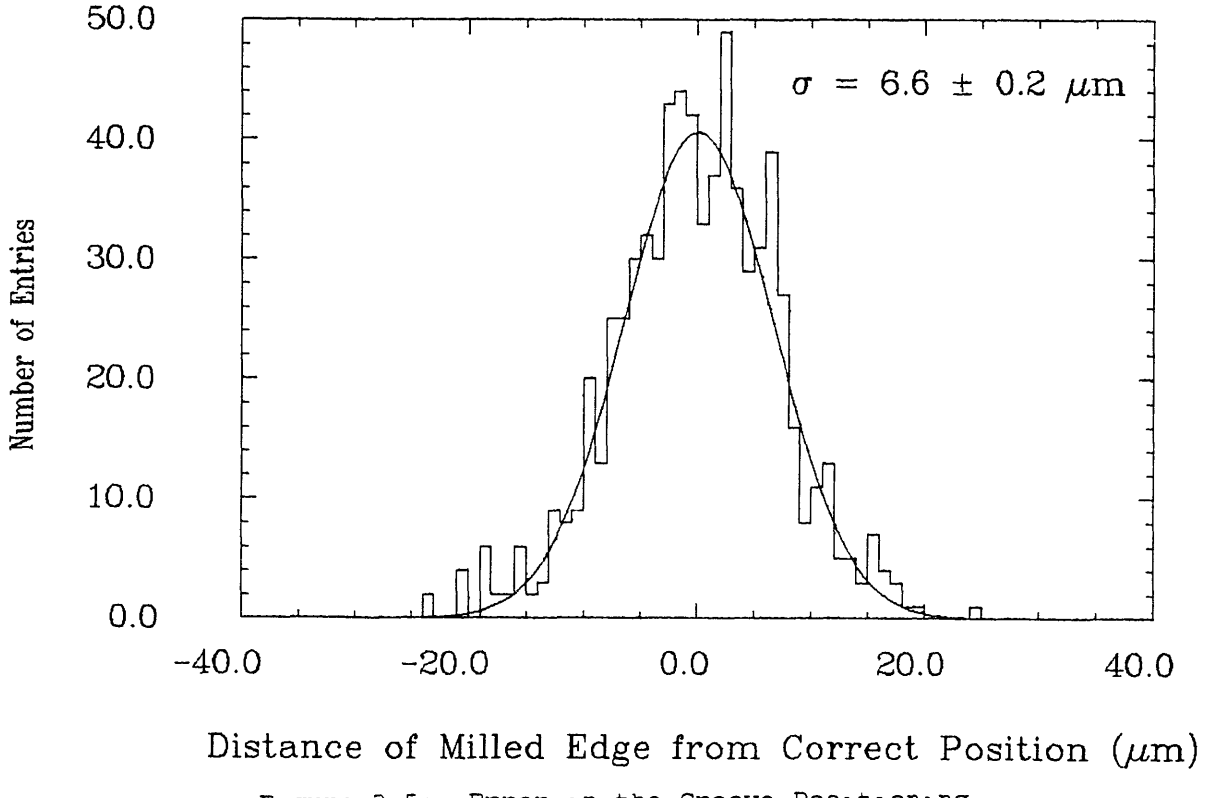

Figure 3.5: Error in the Groove Positioning

When the wiring was complete, the sense wires were aligned to an accuracy of ± 50 μm by rotating the feed-throughs while viewing planes of field wires through a travelling telescope.

The chamber was surrounded by a 125 μm Kapton sheet coated with a 30 μm layer of copper to form the outer equipotential. Finally, it was enclosed in a pressure vessel consisting of an aluminium cylinder 1.5 mm in thickness and two 2 cm thick fibreglass end flanges. The system could be pressurized to 4 bar.

3.5 HIGH VOLTAGE SUPPLY

For the voltage distribution, the chamber was divided into 48 independent sectors, 4 (radial) x 12 (azimuthal). Each contained 12 sense wires in the inner layers and 18 sense wires in the outer layers. The connection to each wire was made through a 22 MΩ resistor. During the operation of the chamber, when a sector drew more than 6 μA, the high voltage supply to that sector was automatically interrupted. Furthermore, a sector could be permanently switched off with only a small loss in the angular coverage if a short circuit developed from a broken wire or if there were bad background conditions in part of the chamber.

The operating voltage for each of the four radial high voltage groups was set at the value where the efficiency stopped increasing with increasing voltage. These settings

were determined by scanning cosmic events online and counting the missing hits. Figure 3.6 shows this efficiency curve and Table 3 the chosen voltage settings. The efficiency at the edge of the plateau was almost 100 %.

TABLE 3

High Voltage Settings for the Vertex Detector

Layer	High Voltage (kV)
1,2	2.70
3,4	2.80
5,6	2.70
7,8	2.85

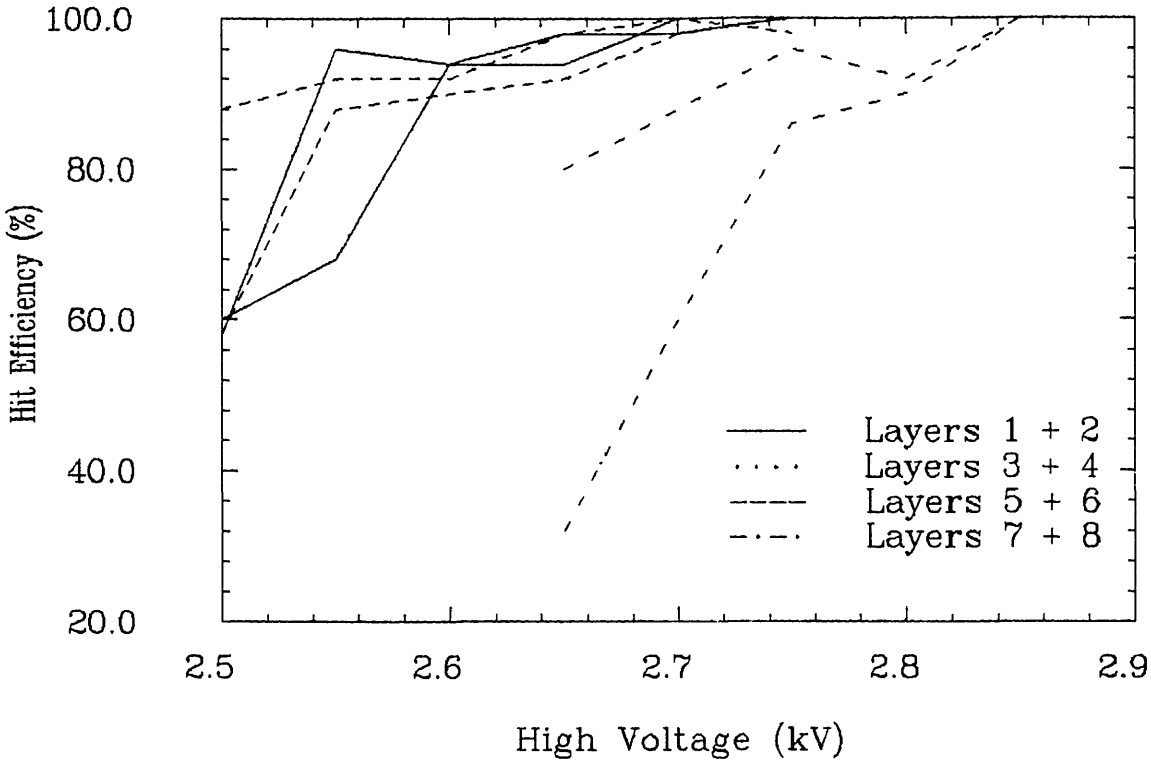

Figure 3.6: High Voltage Plateau

3.6 GAS SUPPLY

The chamber used a 95 % argon 5 % carbon dioxide gas mixture at a pressure of 3 bar. The argon is the ionizable medium and the carbon dioxide is required for quenching the fluorescence photons from the argon so stopping the spread of the ionization and the subsequent breakdown of the gas.

As the drift velocity of the electrons produced by the track is dependent on the gas density, it was important to compensate for changes in the gas temperature due to heating of the beam pipe during a data taking run. The density of the gas within the chamber was regulated using a feedback system by the gas rig and was kept at a constant value.

Originally a gas mixture of 50 % argon and 50 % ethane at 4 bar was chosen. Unfortunately due to the 50 - 60 kV cm^{-1} field strength at the field wire, carbon filaments grew spontaneously from the field wires to sense wires. This phenomenon did not occur with the present gas mixture.

3.7 ELECTRONICS

The electronics attached to each sense wire is shown in Figure 3.7. The pulse produced from the arrival of the drifting electrons propagates down the sense wire which had a characteristic impedance of 380 Ω. The pulse is transmitted between the aluminium and the fibre glass end flanges by a 180 pF coupling capacitor and a parallel earth wire to a 390 Ω resistor. All 720 sense wires were read out in this manner at one end of the detector. The wires in layers 3, 4, 7, 8 which were also to be used to make charge division measurements, to find the z position of the track, were read out at both ends.

Outside the chamber end flange, emitter-follower transistors were used to drive the 11 m coaxial cable to the discriminator and amplifier cards. The discriminator was designed to reduce the dependence of the digitized times on the incoming pulse height. The signal from the sense wire was fed through a 5 ns delay into the normal input and through a resistive divider into the inverting input of a differential comparator. The timing decision was made on

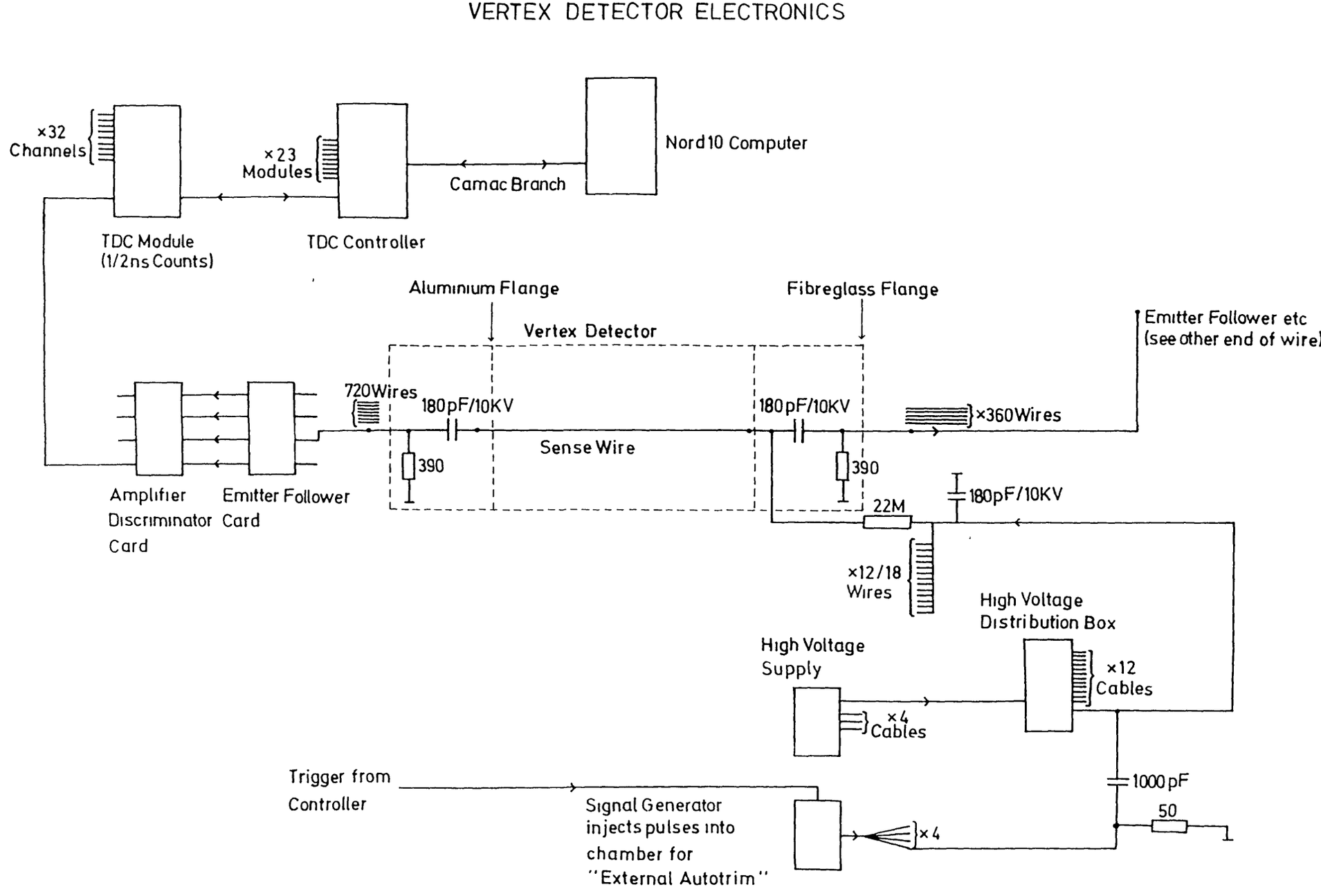

Figure 3.7: Vertex Detector Electronics

the differential cross-over point of these two signals. A second comparator stage was used to set the discriminator threshold and signals above this threshold triggered an ECL line driver. The ECL pulses were 450 ns long to prevent a channel in the TDC system receiving two start signals in an event. A diagram of the discriminator and pulse shapes is shown in Figure 3.8.

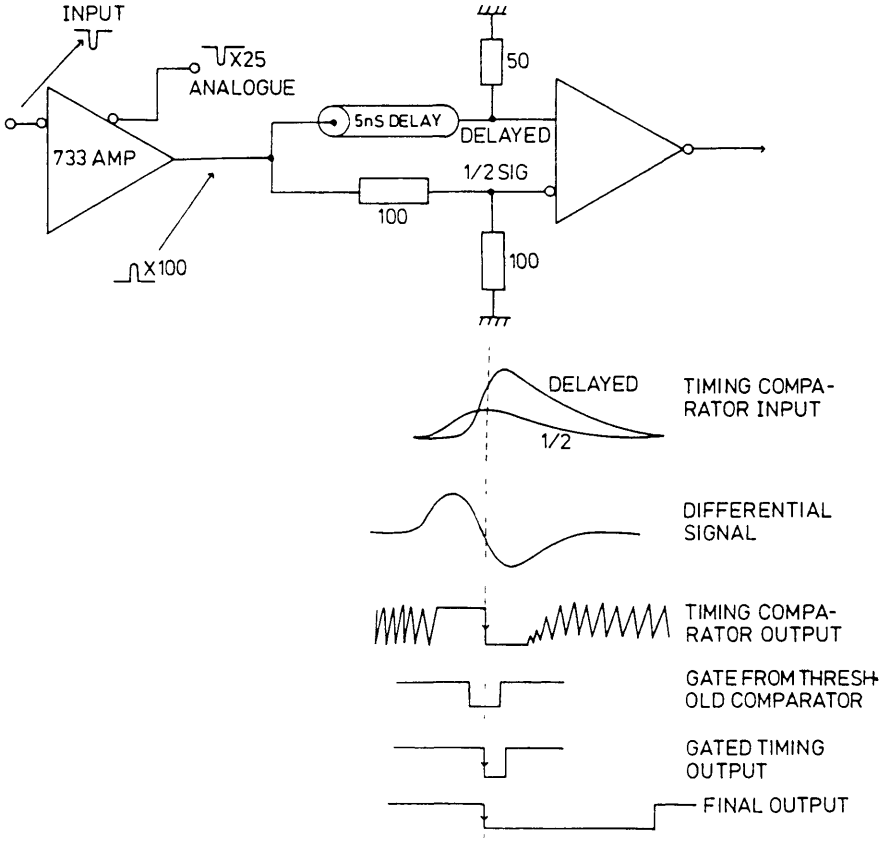

Figure 3.8: Discriminator and Pulse Shapes

The drift time was measured with ½ ns resolution by a Lecroy 4290 TDC system used in 'common stop' mode. The TDC stop signal for all channels was derived from the beam

pick-up signal, while the start signal for a given channel was provided by the leading edge of the ECL pulse from a sense wire discriminator. In this mode, the TDC's were continuously being started and reset after counting to full scale. Only when the common stop signal coincided with a valid trigger were the times digitized and read out through the CAMAC system to the NORD 10 computer.

3.8 CALIBRATION OF THE TDC SYSTEM

In order to find a single space-drift time relation for each layer of sense wires, it was essential that each TDC had the same calibration. Variations can occur in the propagation time of a signal from the sense wire to the start input of the TDC module. There can also be variations in the scaling constant to convert a physical time into a digital value. Therefore, at the start of each data taking run, a calibration sequence was performed. Start and stop pulses with a separation corresponding to a zero and full scale digitized time were generated by the TDC system controller and fed into each TDC channel. The offset and scaling constant for each channel were automatically adjusted until the digitized time from each channel was the same to within ½ ns. Then, to correct for differences in channel to channel time delays from the sense wires to the start inputs, calibration pulses were injected along the high voltage cables into the chamber to simulate data pulses on the sense wires. The offset in

each TDC channel was again adjusted until the digitized time from each channel was the same to within ½ ns.

This calibration sequence was able to align all channels to within ± ½ ns, the success of the method was ultimately reflected in the measured chamber resolution. However, as the delays were being set each data taking run, a method was needed to monitor any systematic shifts in the delays chosen by the TDC system controller over long periods of time. Advantage was taken of the fact that one high voltage sector had to remain switched off due to excessive current being drawn from those wires. A signal derived from the beam pick-up signal, which is the timing reference for the whole experiment, was feed directly into the TDC channels for this sector. Figure 3.9 shows the digitized time for this calibration check over many data runs. A clear discontinuity can be seen in this scatter plot which happened to correspond to the time of replacement of the TDC system controller. By looking for such discontinuities, which always occured when parts of the hardware were replaced, a decision was made on the run number for which a new space-drift time relation needed to be determined.

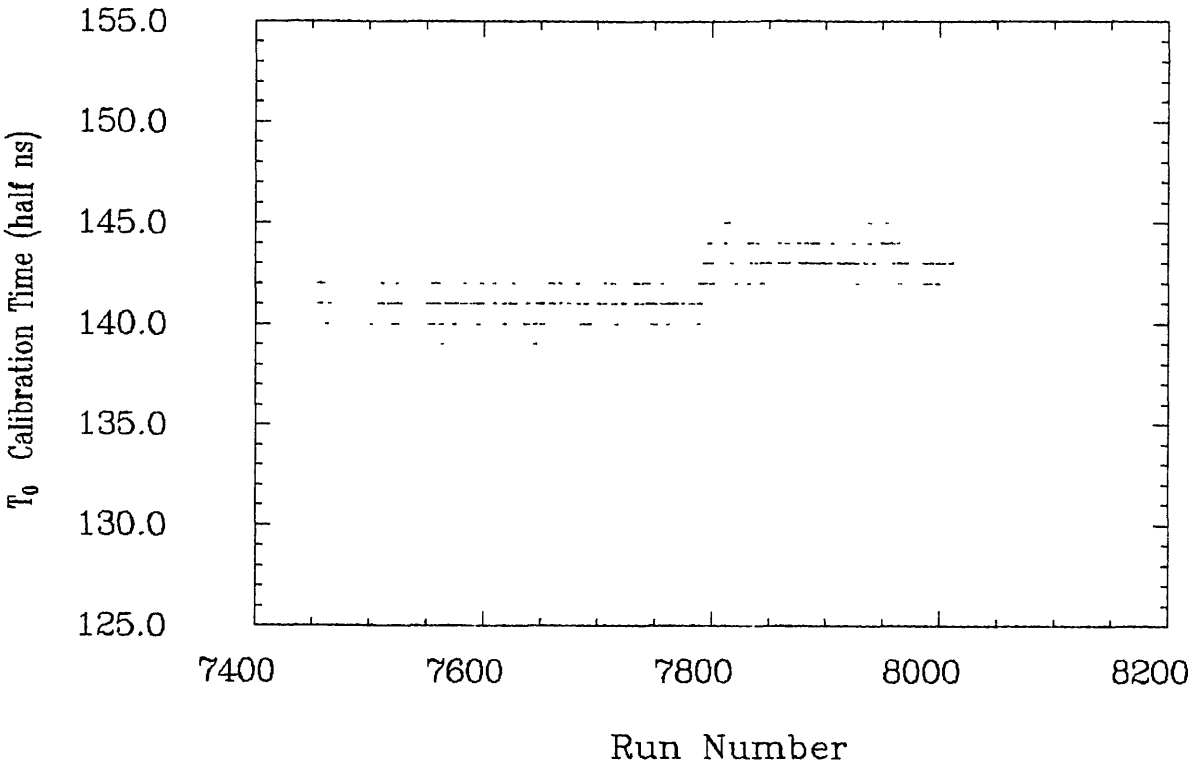

Figure 3.9: TDC Stability Over Many Runs

3.9 SPACE-DRIFT TIME RELATION

In order to convert the measured drift time into the position at which the particle went through the drift cell, a relation between the TDC value and the distance in the azimuthal direction from the sense wire had to be determined.

The principles of the procedure were as follows. Events that originated from beam-beam interactions were selected from the two prong data. These events contained only two tracks that were reconstructed in 3 dimensions in the large drift chamber. Cosmic ray events were rejected using the time of flight counter information.

Initially, a linear space-drift time relation was assumed. The drift velocity was estimated to be 43 μm/ns using the range of TDC values and the width of the drift cell. Tracks in the r-ϕ plane were reconstructed using only the hit information from the 8 layers of the vertex detector, with the track curvature in the large drift chamber as a constraint. Then, for each space point used in the track fit, a residual was defined as the distance between the track and that space point. For each layer, the drift distance (x) was parameterized in terms of the drift time (t) as a third degree polynomial:

$$x = a + b\,t + c\,t^2 + d\,t^3$$

The paramaters (a, b, c, d) were then fitted to minimize the sum of the squares of the residuals. The whole procedure was then iterated using the new estimate of the space-drift time relation until convergence. No dependence of these constants on the entrance angle of the track in the cell was found. Figure 3.10 shows the space-drift relation for each layer of sense wires.

The resolution shown in Figure 3.11 was measured by combining the residuals from all layers. From the spread of calibration times that is shown in Figure 3.9, the timing resolution on a given layer was about 1 ns. With a gas drift velocity of 43 μm/ns the ultimate resolution achievable was than around 43 μm. However, there were a number of factors that caused a worsening in resolution:

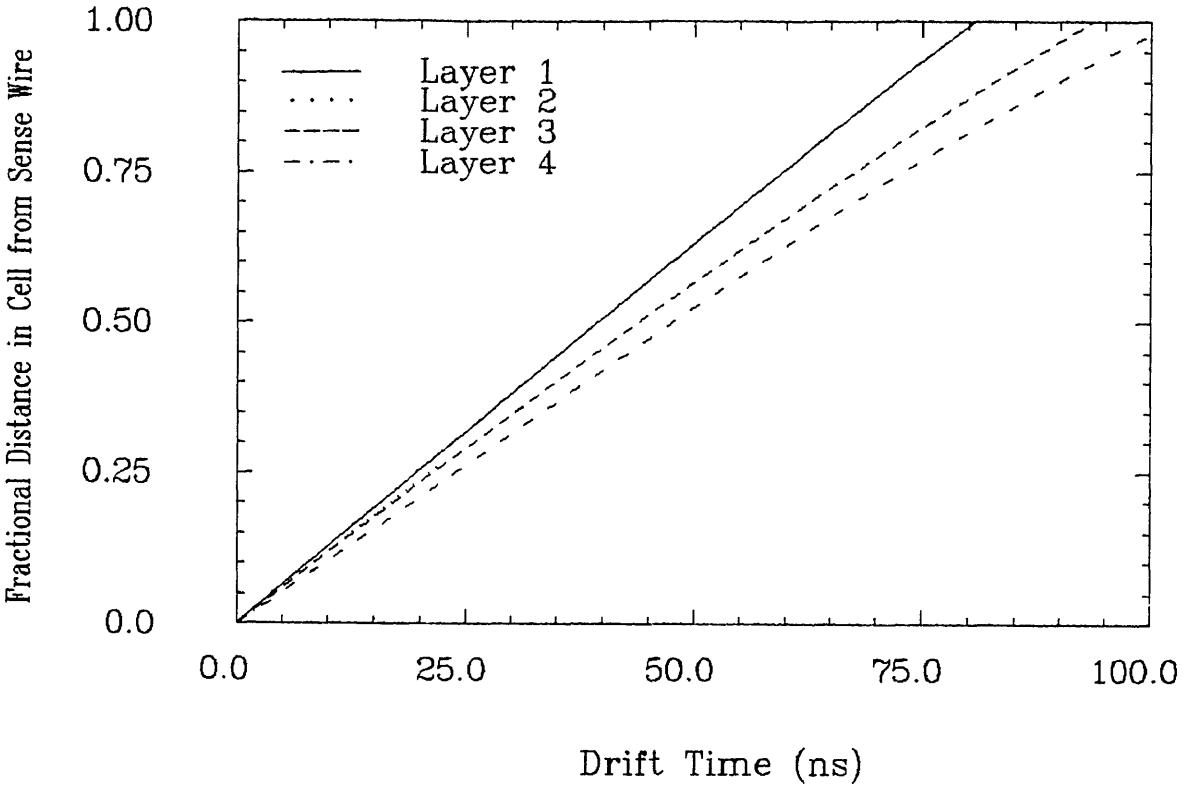

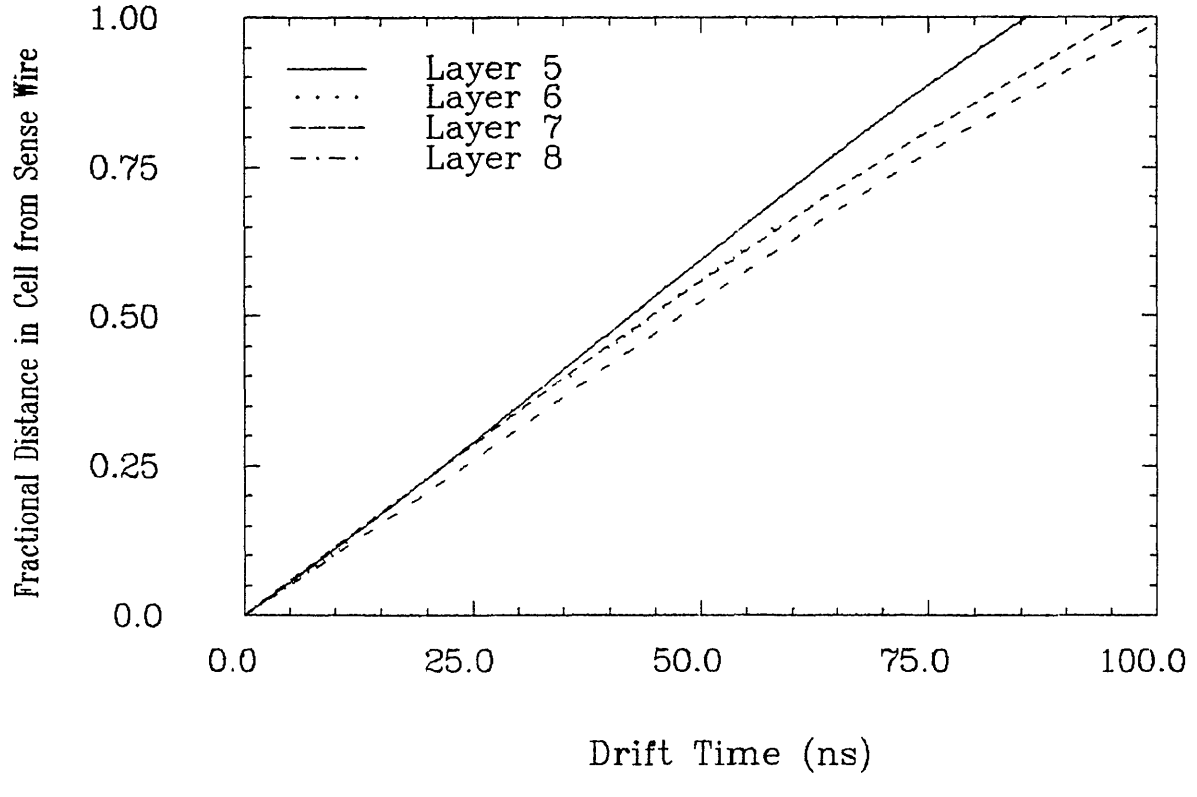

Figure 3.10: Space-Drift Time Relation

1. variations in the timing decision from wire to wire.
2. inaccuracies in the determination of the space-drift time relation.
3. mistakes in the hits assigned to tracks.
4. uncertainty in the relative position of the sense wires.

All these factors combined to give a measured resolution of 104 μm.

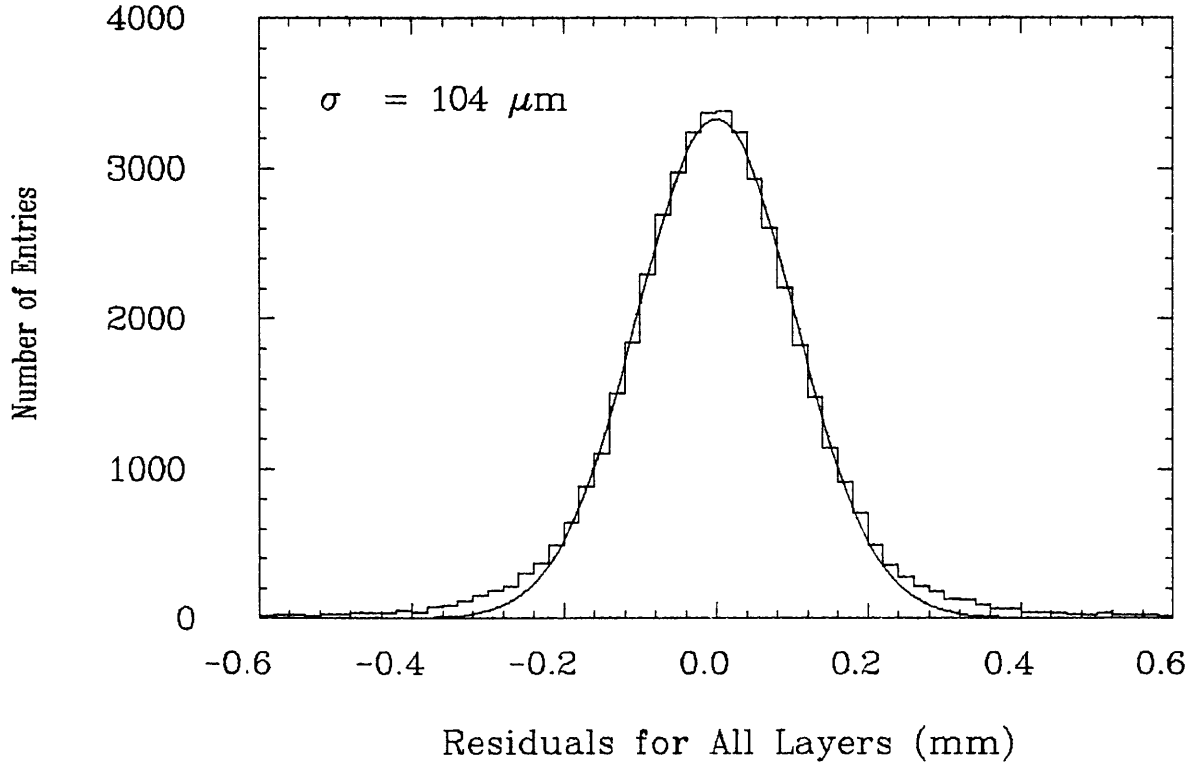

Figure 3.11: Residuals for All Layers

3.10 CHAMBER ALIGNMENT

In order to use the vertex detector hit information in a combined fit with the information from the large drift chamber, it was necessary to determine the relative alignment of the vertex detector to an accuracy comparable to its resolution.

The relative alignment of the two chambers was determined by minimizing the differences between corresponding tracks reconstructed separately in the large drift chamber (MILL-tracks) and in the vertex detector (VXD-tracks). The effect of multiple scattering in the material between the chambers was minimized by only using tracks with high momenta. Muon pair events produced at around 40 GeV centre of mass energy were used as they had this property. A MILL-track was projected into the outermost layer of the vertex detector at radius R. The angular difference $\Delta\alpha$ between the extrapolated track and the VXD-track at angle ϕ in the outermost layer is given by:

$$\Delta\alpha = \Delta\phi + (- \Delta x \sin \phi + \Delta y \cos \phi) / R$$

where Δx and Δy are the differences between the true and assumed vertex detector positions in the x and y directions respectively, (see Appendix A for TASSO co-ordinate system). $\Delta\phi$ is the difference between the true and assumed relative rotation of the two chambers about the z-axis. The sine and cosine terms just resolve the effect of an x or y shift at

an angle ϕ to the x-axis. By a summation of this expression for tracks over many events, contributions from the sine and cosine terms average to zero so $\Delta\phi$ can be found. Similarly, by summation over the appropriate angular quadrants, the Δx and Δy terms can also be found. The centre of the chamber was found in the drift chamber co-ordinate system to be at:

$$x = 0.34 \pm 0.01 \text{ cm}$$

$$y = -0.13 \pm 0.01 \text{ cm}$$

$$\phi = -0.0293 \pm 0.0001 \text{ rad}$$

In order to check if the vertex detector was skew relative to the drift chamber, it was divided into 4 sections by planes normal to the z-axis. The (x,y) shift for each section was found to be dependent on z. The distance between the measured (x,y) shift at the centre and at the ends of the chamber at $z = \pm 28$ cm was (730,-200) μm. This z dependent shift did not significantly effect the efficiency of the track finding programs in associating space points with tracks. As the final track parameterisation was dependent on this skew, the track finding strategy chosen was to use the vertex detector position described by x,y and ϕ when searching for a track. Then, using the z co-ordinate information available for the track found in the large drift chamber, the track parameters were refitted with the skew position described by an (x,y) shift and three Euler rotations. The z position of the vertex detector could not be

determined but was not needed. This method had the advantage that the space points only needed to be transformed once into the drift chamber co-ordinate system during the track finding procedure.

The Euler angles and shifts were determined, by minimizing the residuals between MILL-tracks projected into the vertex detector and the space points within the detector.

Chapter 4

THE TAU LEPTON

4.1 LEPTONS

In 1936, a new short lived particle was observed with nuclear photographic emulsion in a cosmic ray experiment. The discovery that this particle, called the muon had similar properties to the electron except that its mass was about two hundred times larger than the electron mass, provided a new problem in particle physics. The problem of why the muon exists is hoped to be solved by the search for and study of new heavier electron-like particles.

The electron and its associated neutrino (e, ν_e) form the first generation of a family of particles known as leptons. The second generation is formed by the muon and its associated neutrino (μ, ν_μ). Through a study of the properties of electrons, muons and their associated neutrinos, a particle is classified as a lepton if it has the following properties.

1. The particle does not interact through the strong interaction.
2. The particle interacts through the weak interaction and also, if charged, through the electromagnetic interaction.

3. The particle does not show internal structure, that is, it interacts as a point-like object.

In addition, the known leptons have the following properties.

1. The particles have spin ½.
2. The particles in each generation obey a lepton conservation law. The leptons have an intrinsic property called lepton number which can only be transferred between particles in a given generation or cancelled on annihilation of a particle with its anti-particle.

4.2 PROPERTIES OF THE TAU LEPTON

4.2.1 Discovery

The first evidence for a new lepton was found at SPEAR /15/ in 1975. An anomalously large number of events were observed in e^+e^- collisions that contained only a high energy electron and muon. These events could be explained by the production of a pair of heavy leptons, called taus (τ), via the pair production process:

$$e^+ e^- \rightarrow \tau^+ \tau^-$$

and the subsequent decay of the taus via the sequences:

$$\tau^+ \rightarrow e^+ \nu_e \bar{\nu}_\tau$$

$$\tau^- \rightarrow \mu^- \bar{\nu}_\mu \nu_\tau$$

4.2.2 Mass

The proof that these electron-muon events were not due to charmed meson decay came from the measurement of the tau mass. The mass was determined by measuring the threshold energy for tau pair production /16/. The tau mass was found to be 1.78 GeV/c^2. Hence, the 3.56 GeV threshold for tau pair production lay below the 3.74 GeV threshold for charmed meson production.

4.2.3 Spin

The cross section for pair production of spin ½ point-like particles is predicted from QED to be:

$$\sigma = \tfrac{1}{2}\beta(3-\beta^2)\, 4\pi\alpha^2 / 3\, s$$

where β = v/c, v being the velocity of the tau in the centre of mass system and c being the velocity of light. The β factor in this expression, which was omitted in a similar expression given in Chapter 1, has a value close to unity at energies well above the threshold for pair production. The effect of this threshold factor is negligible for the tau data at PETRA energies. From a study /17/ of the value and behaviour of this cross section near the production threshold, the tau was found to have spin ½. The cross section would be a factor of four smaller if the tau had spin 0 and the threshold behaviour would differ if the tau had spin 1.

4.2.4 Coupling

The discovery of a new lepton provided another way of testing the GWS standard model /18/ of weak interactions. In this theory, the form of the τ-ν_τ weak interaction current is given by:

$$j = g\ \bar{u}(\nu_\tau)\ \gamma^\lambda\ (1 - \gamma_5)\ u(\tau)$$

where u are the Dirac spinors, the γ's are the Dirac matrices and $\sqrt{2}g^2 = G_F$ the Fermi constant /19/. The vector (V) and axial vector (A) nature of this current has been studied by the DELCO collaboration /20/. The momentum spectrum of the electrons produced from the leptonic decay of the tau were in agreement with V-A theory and in disagreement with a V, A, or V+A theory.

After the establishment of all these properties, the tau and its associated neutrino were taken as the third generation in the family of leptons /21/. The fact that the electron, muon and tau differ only in their different masses and separately conserved lepton numbers is known as e-μ-τ universality.

4.3 DECAY OF THE TAU

The tau can decay leptonically to produce an electron or muon and semi-leptonically to produce hadrons. The decay diagrams are shown in Figure 4.1.

The decay rate for the process:

$$\tau^- \rightarrow \nu_\tau\ e^-\ \bar{\nu}_e$$

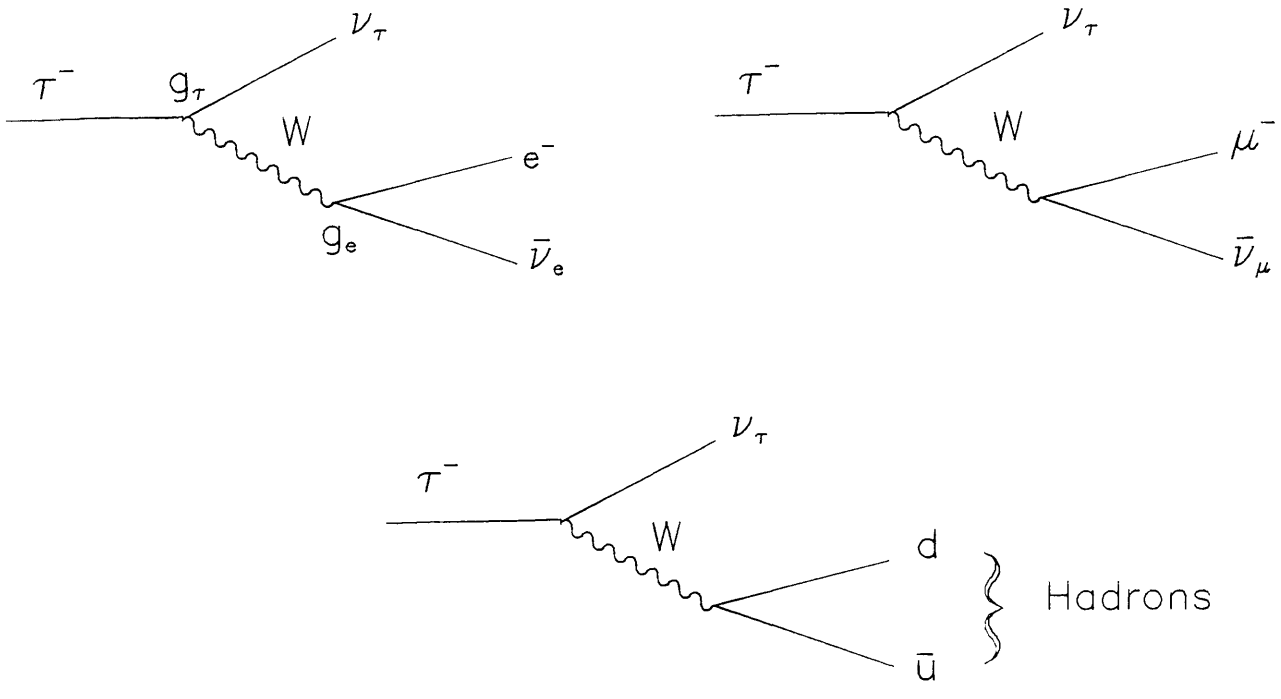

Figure 4.1: Tau Decay Diagrams

is predicted by weak interaction theory /19/ to be:

$$\Gamma_e = 2\ g^2\ g_\tau^2\ m_\tau^5\ /\ 192\ \pi^3$$

where $g^2 = G_F/\sqrt{2}$, g_τ is the τ-ν_τ-W coupling constant and m_τ is the tau mass. Similarly, the decay rate for the muon into electron and neutrinos is predicted to be:

$$\Gamma_\mu = G_F^2\ m_\mu^5\ /\ 192\ \pi^3$$

where m_μ is the muon mass. The lifetime of the tau (T_τ) is then given by:

$$T_\tau = B_e/\Gamma_e = B_e\ (g/g_\tau)^2\ (m_\mu/m_\tau)^5\ T_\mu$$

where B_e is the branching fraction for the process $\tau^- \rightarrow \nu_\tau e^- \bar{\nu}_e$ and T_μ is the lifetime of the muon.

The experimentally measured branching fraction /22/ $B_e = 0.176 \pm 0.011$ is used together with the assumption that $g_\tau = g$ to obtain the theoretical prediction for the tau lifetime:

$$T_\tau \text{ (theory)} = (2.8 \pm 0.2) \times 10^{-13} \text{ s}$$

The only significant contribution to the uncertainty in this value comes from the error on the measurement of the branching fraction.

Alternatively, the experimentally measured value of the lifetime can be used to compare the tau weak coupling constant with the Fermi constant:

$$T_\tau \text{ (theory)} / T_\tau \text{ (measured)} = g_\tau^2 / g^2 = G_\tau / G_F$$

where G_τ is defined as $\sqrt{2} g_\tau^2$. If the value of G_τ is shown to be consistent with the value of G_F, the concept of e-μ-τ universality is shown to be reasonable.

4.4 PREVIOUS MEASUREMENTS OF THE TAU LIFETIME

A number of experiments, limited by the resolution at the event vertex, have put upper limits on the tau lifetime /23/. Previous measurements /24/ of the tau lifetime have been made by:

MARK II $(4.6 \pm 1.9) \times 10^{-13}$ s

MAC $(4.9 \pm 2.0) \times 10^{-13}$ s

CELLO $(4.7 \pm {}^{3}_{2}{}^{.}{}^{9}_{9}) \times 10^{-13}$ s

Recently, MARK II have measured the tau lifetime to be $(3.20 \pm 0.41 \pm 0.35) \times 10^{-13}$ s using a high resolution drift chamber /25/ which improved the vertex resolution.

Chapter 5

TAU EVENT SELECTION

5.1 INTRODUCTION

The position of the tau decay point was found by reconstructing a vertex using the tracks from its decay products. In this chapter, the selection procedure for obtaining a tau data sample, containing events with a suitable topology for vertex reconstruction, is described. The backgrounds from other processes that can simulate the tau event topologies are estimated. The number of tau events found is compared to the number expected using QED theory, the known topological branching fractions and the estimated detector acceptance. Finally, two different methods for reconstructing tracks using the hit information from the vertex detector are compared.

5.2 TAU EVENT SELECTION

At PETRA energies, far above the tau pair production threshold, the signature for $e^+e^- \rightarrow \tau^+\tau^-$ is very distinctive. Each tau decay can produce one or three well collimated charged tracks. Events were selected that contained one charged track opposite three charged tracks (referred to as 1+3 topology) or three charged tracks opposite three charged

tracks (referred to as 3+3 topology). A 1+1 topology is not useful for vertex reconstruction.

Events were selected using only the charged track information available from the large drift chamber. The procedure, which had been previously developed for an analysis of the tau branching fractions /26/, will be briefly described.

The events were selected from the PASS3 data sample as up to this point in the data reduction chain, tau pair events had not been specifically excluded. The following selection criteria had two aims, firstly to select a specific event topology and secondly to reduce the background contamination.

5.2.1 1+3 Topology

The following conditions had to be satisfied to select a 1+3 topology event.

1. There must be only four charged tracks reconstructed in three dimensions with $|d_0| < 5$ cm, and $P_t > 0.1$ GeV/c.

Then considering only those four charged tracks.

2. One track must be separated from the other three by more than 120°.
3. The angle between any pair of tracks in the three track system must be less than 45°.
4. The summed charge (ΣQ) of the 3 track system must be ± 1 and the summed charge of the considered tracks must be 0.

5. The summed track momentum must be greater than 6 GeV, with the single isolated track having a momentum greater than 0.2 GeV/c.
6. The effective mass of the 3 track system assuming pion masses had to be less than 2 GeV/c^2.
7. The effective mass of each pair of oppositely charged tracks assuming electron masses had to be greater than 0.15 GeV/c^2.
8. These oppositely charged tracks must intersect in the r-ϕ plane at a distance of less than 8 cm from the beam axis.

Conditions (1 to 4) selected the 1+3 topology with the appropriate charges for the decay of a tau pair system. The events were allowed to contain other low momentum tracks that did not come close to the interaction region. These tracks were due to the back-scattering of the outgoing particles in the material of the magnet coil. Condition (5) reduces the background from two photon processes, condition (6) reduces the background from hadronic events. The background from radiating Bhabha events was reduced by conditions (7 and 8).

After this selection procedure and subsequent visual scan (to be discussed further in the section on backgrounds), 45 events remained.

5.2.2 3+3 Topology

The following conditions had to be satisfied to select a 3+3 topology event.

1. There must be only six charged tracks reconstructed in three dimensions with $|d_0| < 5$ cm, and $P_t > 0.1$ GeV/c.

Then considering only those six charged tracks.

2. Two 3 track systems must exist where the angle between the summed momentum vectors of each system is greater than 120°.
3. The conditions (3 to 8) for the 1+3 topology selection, except those that specifically refer to single isolated tracks, must be satisfied.

After this selection procedure and subsequent visual scan 11 events remained. Figure 5.1 shows a tau event with a 1+3 topology and Figure 5.2 shows a tau event with a 3+3 topology.

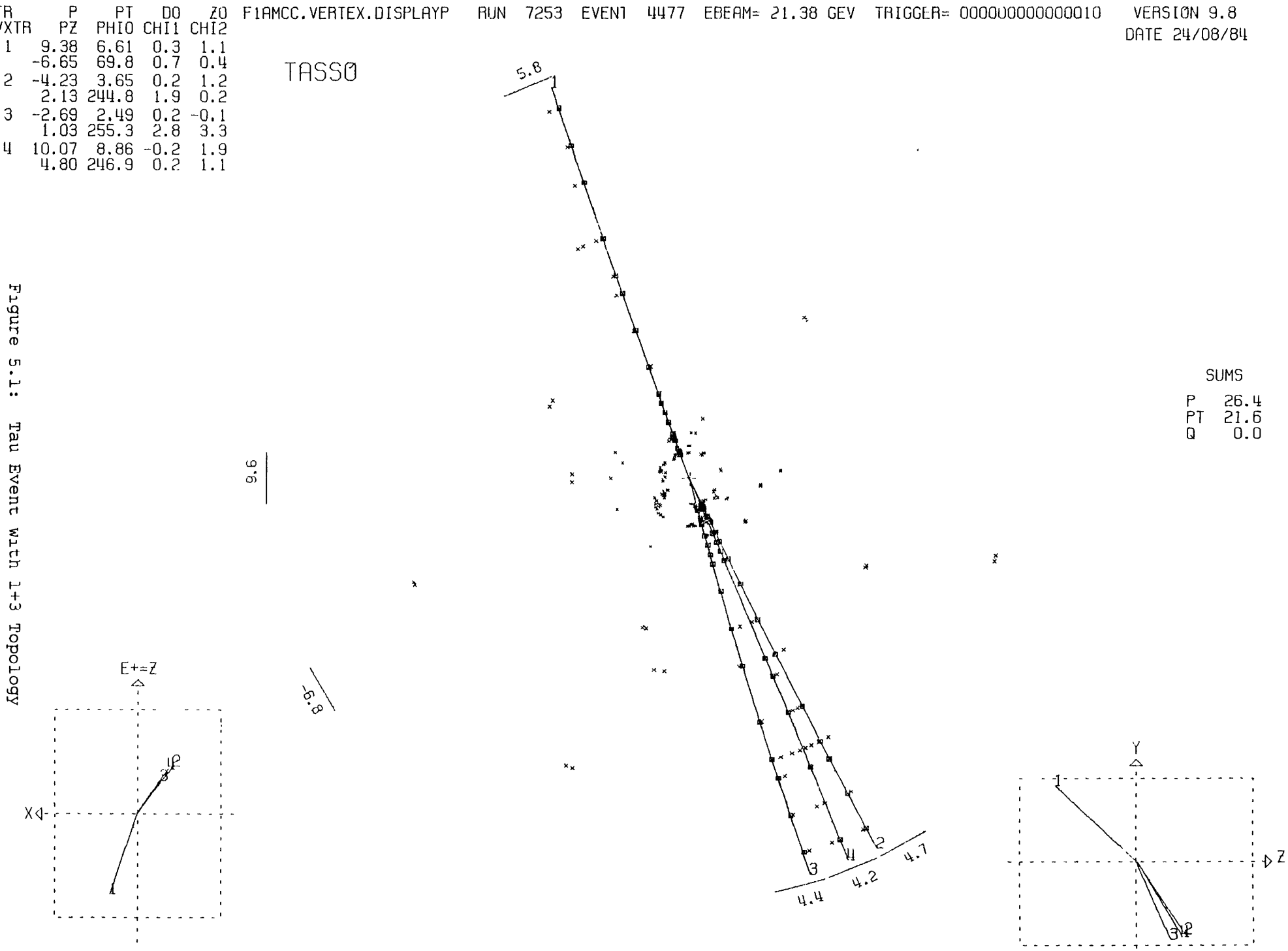

Figure 5.1: Tau Event With 1+3 Topology

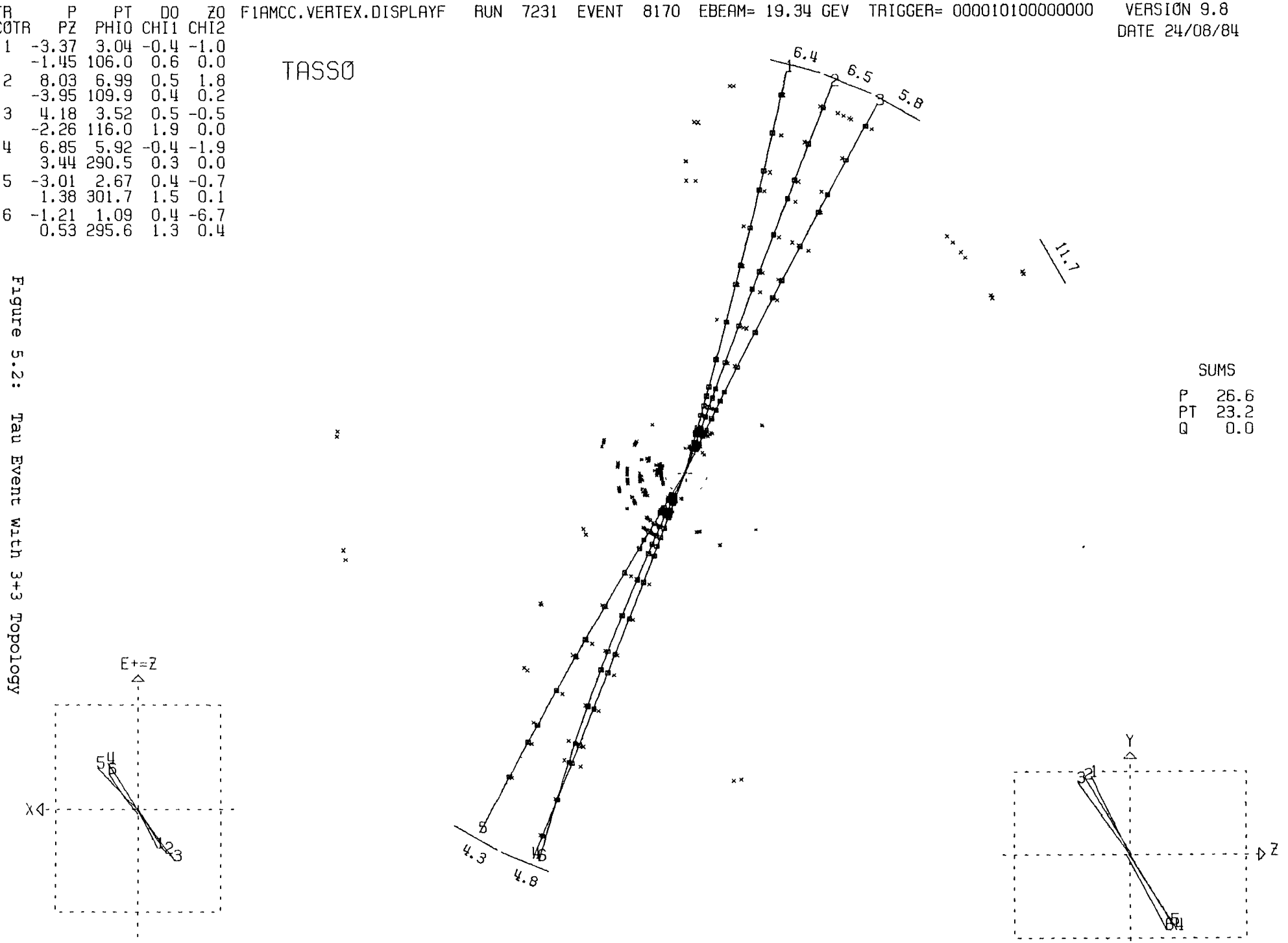

Figure 5.2: Tau Event with 3+3 Topology

5.3 ESTIMATION OF THE NUMBER OF EVENTS EXPECTED

The total number of tau pair events (N) that occured is given by:

$$N = \sigma L C$$

where σ is the cross section for tau pair production, L is the integrated luminosity over the data taking period from which the events have been selected and C is the radiative correction to this cross section.

The number of tau pair events of a given topology (n) that are detected is given by:

$$n = N A \epsilon B$$

where A is the detector acceptance, ϵ is the experimental trigger efficiency and B is the branching fraction to a given topology.

5.3.1 Cross Section and Luminosity

The tau data were collected during an energy scan from 39.8 GeV to 45.2 GeV centre of mass energy. The average energy, weighted with the luminosity measured at each point, was 42.5 GeV. The integrated luminosity collected over this period was 10.5 pb^{-1}. The tau pair cross section, calculated using this weighted average energy and the equation for the cross section of lepton pair production to order α^2 discussed in Chapter 1, is 48.5 pb.

5.3.2 Tau Pair Event Generator

Tau pairs were generated using an event generator of Berends and Kleiss /27/ which took account of higher order QED radiative corrections. At 42.5 GeV centre of mass energy, the radiative correction factor to the cross section from initial state Bremsstrahlung, vertex and virtual loop corrections, was 1.36. Each tau was allowed to decay via the channels that produced a 1+3 or 3+3 topology ($\tau \rightarrow 3\pi\pi^0\nu$, $\tau \rightarrow 3\pi\nu$). The momentum spectrum of the neutrino emitted during the leptonic or semi-leptonic decay was generated according to the predictions of V-A theory. The four momentum vectors of the produced particles were output from the event generator and used in the detector simulation.

5.3.3 Detector Simulation

All generated particles that had not decayed before reaching the beam pipe were passed through the detector simulation /28/. Only those parts of the simulation relevant to this analysis will be discussed in detail.

The production points of the tau pairs could all be generated at a common point, or chosen to lie on a distribution that represented the size of the beam spot in the x and y directions. The lifetime of the tau could be specified and the decay channels chosen.

The charged hadrons could interact in the detector material with the production of secondary particles. The secon-

dary multiplicity was set empirically to represent that observed in the TASSO data. Photons could convert and electrons lose energy on passing through the detector material. Multiple scattering could occur in each layer of material with the modified momentum vector of the scattered particle being traced through the tracking chambers. If a particle decayed, the trajectories of the daughter products were followed.

As a particle travelled through a drift chamber, its position at each layer of wires was recorded and smeared with the detector resolution. A mirror image hit on the opposite side of the sense wire was also generated to produce the left-right ambiguity found in the drift chambers. Random noise hits, cross talk hits between adjacent wires and the hit efficiency were simulated such that the Monte Carlo events represented the observed data.

An event trigger simulation decided if a generated event would produce a valid trigger and then these events could be subjected to the PASS1, PASS2 and PASS3 selection conditions. Events output from this Monte Carlo program could be processed with a track-finder and analysed as though they were real data.

5.3.4 Detector Acceptance

The acceptance of the detector, for a given event type, is defined as the ratio of the number of events seen with the real detector, with its imperfect tracking information and incomplete angular coverage, to the number of events that would be seen with a perfect detector covering the complete solid angle. The simplest way to find this ratio is to pass a known number of tau events through a Monte Carlo detector simulation. 2700 events were generates with the tau decaying with a 1+3 topology. The 1+3 topology candidates were selected by requiring these events to satisfy the event trigger, the standard data reduction conditions to PASS3 and the 1+3 topology selection conditions. 33 % of the generate events remained. A similar exercise was carried out with 2100 events generated with a 3+3 topology, 20 % of these events remained.

The number of events generated with a 3+3 topology that were only recognized as events with a 1+3 topology was 1 %. These misidentified events were ignored, as the error introduced in doing so was small compared to the error on the topological branching fractions.

5.3.5 Trigger Efficiency

The 'coplanarity' trigger had been estimated to be 94 ± 0.2 % efficient when triggering on 2 track events. Essentially, this was measured by selecting 2 track events in-

dependently which had liquid argon or shower counter triggers and then checking if there was also a 'coplanarity' trigger. From this, the trigger efficiencies for a 1+3 topology and a 3+3 topology were calculated to be 96.8 ± 0.1 % and 99.9 ± 0.1 % respectively.

5.3.6 Branching Fractions

The branching fraction for a tau to one charged track (B_1) and three charged tracks (B_3) have been measured at TASSO /26/ as:

$$B_1 = 0.847 \pm 0.011 \text{ (stat)} \pm 0.015 \text{ (sys)}$$

$$B_3 = 0.153 \pm 0.011 \text{ (stat)} \pm 0.015 \text{ (sys)}$$

Using these values, the branching fractions to a 1+3 topology ($2B_1B_3$ as two possible combinations) and a 3+3 topology (B_3B_3) are calculated to be:

$$B_{1+3} = 0.259 \pm 0.015 \text{ (stat)} \pm 0.021 \text{ (sys)}$$

$$B_{3+3} = 0.023 \pm 0.003 \text{ (stat)} \pm 0.005 \text{ (sys)}$$

5.3.7 Number of Events

All these results are summarised in Table 4 together with the number of events expected and the number found.

The errors on the number of events expected are dominated by the 33 % error on the branching fraction to the 3+3 topology and the 14 % error on the branching fraction to the 1+3 topology. A more detailed discussion on the discrepancy between the numbers expected and the numbers found will be discussed after the backgrounds have been estimated.

TABLE 4

Events Expected and Events Found

Cross section	48.5 pb	
Luminosity	10.5 pb^{-1}	
Radiative Correction	1.36	
	1+3 topology	3+3 topology
Acceptance	0.33	0.20
Trigger Efficiency	0.97	1.00
Branching Fractions	0.259	0.023
Events Expected	57 ± 8	3 ± 1
Events Found	45	11

5.4 BACKGROUND ESTIMATION

An estimation needs to be made of other background processes that have the same event topology as the tau events. These background processes are radiative Bhabha events, tau production by two photon collisions, and low multiplicity hadronic events.

5.4.1 Radiative Bhabha Events

If one or two photons are radiated in a Bhabha scattering event and subsequently convert into electron positron pairs, an event with a 1+3 topology or, much less likely, a 3+3 topology can be produced. This background has already been

suppressed by making an effective mass cut of 0.15 GeV/c^2 for oppositely charged pairs of tracks, assuming electron masses. However, some events were not removed by this cut due to imperfect tracking. These events were distinctive due to the almost zero opening angle between the tracks. All events in the selected sample were scanned visually and rejected if a gamma conversion was recognized. A typical radiative Bhabha event is shown in Figure 5.3.

The effectiveness of this scan was verified by the fact that suspected background events whose tracks lay within the liquid argon acceptance were identified as electrons. As further confirmation, a plot of the angle θ between the single isolated track and the incoming beam of the same charge, for the selected tau events, showed no peaking in the forward direction; such peaking would be expected for Bhabha events. The scan rejected 5 events with a 1+3 topology, none of the events with a 3+3 topology were rejected.

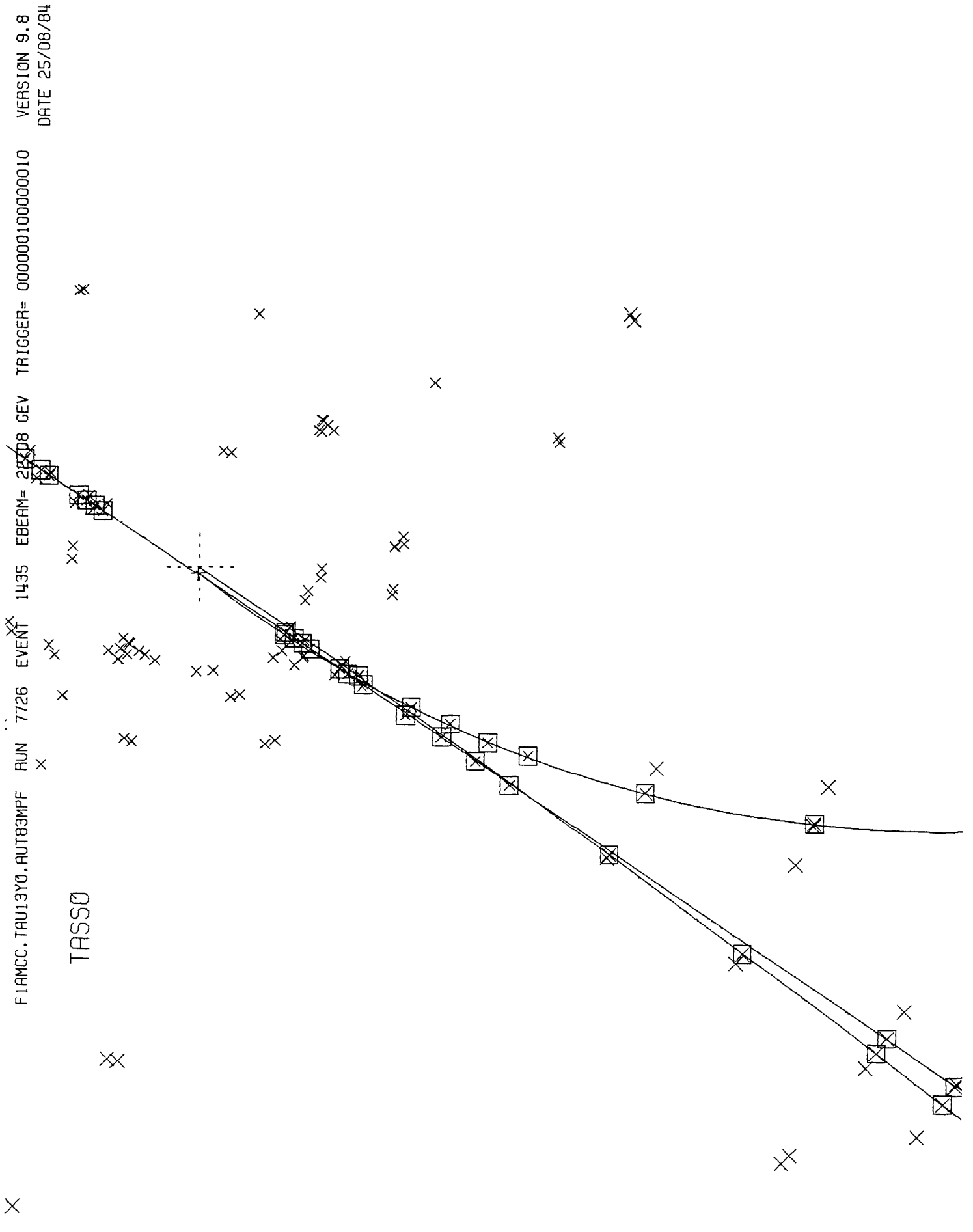

Figure 5.3: Radiative Bhabha Event

5.4.2 Tau Pair Production by Two Photon Collisions

Tau pair production from two photon collisions are considered as a background. The reason is that the relativistic boost of the tau needs to be known when converting a measured decay length into a proper decay time. The boost is calculated from the tau mass and the beam energy with appropriate radiative correction, this will be further discussed later. However, for two photon collisions, the boost cannot be estimated as only a small fraction of the beam energy is acquired by the tau system.

To estimate this background, a two photon generator of Berends et al. /29/ was used to generate 3400 events of the type $e^+e^- \rightarrow e^+e^-\gamma\gamma \rightarrow e^+e^-\tau^+\tau^-$ at a centre of mass energy of 42.5 GeV. The cross section for this process at this energy was 110 ± 1 pb so 3400 events correspond to a luminosity of 30.9 pb^{-1}, a factor of 3.0 more than that collected experimentally. After these generated events had been passed through the detector acceptance and event selection procedure, five events with 1+3 topology and one with 3+3 topology remained. This gave a background in the tau data sample with a 1+3 topology of 1.7 ± 0.7 events, and with a 3+3 topology of 0.34 ± 0.34 events.

5.4.3 Hadronic Events

Another source of background was hadronic events that had a low charged track multiplicity and a similar topology to the tau events. The Lund generator /30/ was used to generate 12900 events of the type $e^+e^- \rightarrow q\bar{q}$ and $e^+e^- \rightarrow q\bar{q}g$ at a centre of mass energy of 42.5 GeV. This corresponded to a luminosity of 67 pb^{-1}, a factor of 6.4 more than that collected experimentally. After selecting events from this data sample using the usual tau selection procedure, one event with a 1+3 topology and six events with a 3+3 topology remained. Hence the hadronic background to the 1+3 and 3+3 topology tau data was estimated to be 0.2 ± 0.2 and 0.9 ± 0.4 events respectively.

TABLE 5

Comparison of Hadronic Monte Carlo and Data

	Data	Monte carlo
1+3 topology	1	0
3+3 topology	0	0.2 ± 0.2

As a check to whether this Monte Carlo represented the data well at these low track multiplicities, the 1+3 and 3+3 topology events were reselected demanding the effective mass of at least one 3 track system to be greater than 2 GeV/c^2.

The results of this selection are shown in Table 5. The statistical significance of these results are poor but it does show the Monte Carlo is not inconsistent with the data.

5.4.4 Background in Tau Events

When the two sources of background that are not negligible are combined, low multiplicity hadronic events and tau production via two photon collisions, the backgrounds to the 1+3 and 3+3 topology events were found to be 1.9 ± 0.7 and 1.2 ± 0.5 events respectively. The total background to the tau event sample of any topology was 3.1 ± 0.9 events.

After the background was subtracted from the number of tau events found, the number of events expected and the number found could be compared. The results are summarised in Table 6.

TABLE 6

Comparison of Tau Events Expected and Found

	Expected	Found
1+3 topology	57 ± 8	43
3+3 topology	3 ± 1	10

The number of tau events with a 1+3 topology is in reasonable agreement to the number expected, but this is not

the case for events with a 3+3 topology. On a detailed visual scan of the 3+3 events, nothing unusual was found in the event topology. The effective mass distribution of those few events was compatible with the Monte Carlo distribution. When similar background calculations had been performed for the tau data at 35 GeV /26/, using a larger data sample which was taken at a time before the installation of the vertex detector, there was no discrepancy between the number of events found and the number expected. Therefore, unless there is some new form of background that has appeared around 42.5 GeV, these 3+3 events must be assumed to be taus. However, as a check, the tau lifetime will also be calculated using each data sample separately.

5.5 TRACK-FINDERS

Two track finding programs had been developed that were able to reconstruct charged tracks within the vertex detector. One, called FELIX /31/, searched for tracks using the hit information from the large drift chamber, CPC, and vertex detector. The other, called PASS5 /32/, took the curvature of the track found by the MILL track reconstruction program and only used the vertex detector information to define the track's position in the r-ϕ plane. Both track-finders had advantages and will now be discussed in further detail.

5.5.1 PASS5 Track-finder

A MILL track was extrapolated into the vertex detector and a 'road' was defined around this track such that all hits within a set distance normal to the track in the r-ϕ plane were located. A circle fit with fixed curvature was performed on all combinations of the located hits that lay within this 'road' to find the track with the lowest χ^2 per degree of freedom. The track was defined by d_0 and ϕ_0 found from the fit together with its curvature r_0 taken from the projected MILL track.

Once a hit had been associated with a track, it was not used any more during the search for further tracks. This saved computer time by reducing the number of combinations of hits to be examined, but it meant that it was necessary to find the cleanest tracks first. If the chamber was noisy, or the tracks were close together, or the tracks passed through the same cell, a fake track could take hits from the genuine ones.

This problem was overcome by having multiple passes through the track searching procedures. A high momentum track is scattered less in the material between the large drift chamber and vertex detector, so a narrower road can be defined around the extrapolated track. By searching first for tracks with high momentum, tracks with good z reconstruction in the drift chamber, and tracks with many hits before those with few, the problem of fake tracks was mini-

mized. Two tracks passing through the same drift cell could be resolved with hits alternately being assigned to each track.

5.5.2 FELIX Track-finder

FELIX used a tree search algorithm to find tracks. An acceptable track consisted of a number of hits that were linked together by a path that satisfied certain conditions. Before the search started, chains of adjacent hit wires were removed from the list of available hits; they were considered to be noise. Then starting with a first hit in the outermost layer of the large drift chamber, a link was made to an adjacent hit that was in the direction of an acceptable track. The path was extended by making a link to a third hit, a circle fit was performed, and a check was made to see if the track was acceptable. If the track was acceptable, another link was made to extend the path. If the track was unacceptable, the last link on the path was broken and another link considered. Each time a link was added, the track was refitted and checked to be acceptable. If and when a path was found that satisfied the required conditions and all layers of hits had been considered, a track had been reconstructed. Then the search for the next track began with a new first hit.

Once a track had been found, a check was made to find any hit closer to the track than the selected ones, if one was

found, it replaced the appropriate selected hit. If this new hit lay on another track, it was assigned to the closer track. Once a hit was assigned to a track, it was removed from the list of available hits used in the tree search procedure.

The search for tracks was performed in several passes with the conditions for an acceptable track being altered after each pass. Tracks were first searched for that had few missing hits, small d_0 and a low χ^2 per degree of freedom. This enabled the more easily recognizable tracks to be found first so reducing the number of available hits quickly.

5.5.3 Advantages of each Track-finder

The FELIX track-finder took advantage of the longer track length when measuring the track's momentum. However, in this lifetime analysis the tracks are going to be refitted to a common vertex using the hit information in all chambers. Therefore, the track-finders need only be compared on their ability to assign the correct hits to tracks. In this respect, the PASS5 track-finder is at a disadvantage as it requires at least 4 hits within the vertex detector to find a track. For events with the tau decay topology, two tracks can pass through the same cell, reducing the number of hits on the track, making it impossible for PASS5 to find a track. However, the use of two track-finders that have com-

pletely different algorithms helped to check for any bias in the track finding methods.

The more complex search procedure used in FELIX made the program a factor of 30 slower in reconstructing an event. If track reconstruction was required for a large data sample, for example the selected PASS2 events used to find the beam spot (the method is described in the next chapter), the speed of the PASS5 program was required as computer resources were limited.

TABLE 7

Comparison of FELIX and PASS5

	FELIX	PASS5
3 track system reconstructed	86 %	77 %
1 track system reconstructed	100 %	100 %
Resolution	136 μm	117 μm

The efficiency and resolution at a point in the vertex detector when using each track-finder to reconstruct tau events are summarised in Table 7. The resolution is defined as the distance between the reconstructed track and the associated hit position. The events are split into the three track system and the isolate single track to take account of

the difficulty in reconstructing closely spaced tracks. The resolution measured using FELIX tracks is slightly worse than using PASS5 tracks. This is probably due to an inaccuracy in the assumed position of the vertex detector. For FELIX tracks this will worsen the measured resolution as the track fit is a combined fit using the hits in both the vertex detector and the large drift chamber.

Chapter 6

TAU LIFETIME ANALYSIS

6.1 INTRODUCTION

The measurement of the tau lifetime using the data from the vertex detector is described in detail in this chapter. The decay length was calculated from the position of the tau production point and decay vertex. As the accuracy of this measurement depended on how well these positions could be determined, a detailed study was made on both the ability of the vertex constraint program to reconstruct the correct decay vertex and the position of the colliding beams. Effects that could artificially generate a finite lifetime were investigated.

6.2 DECAY LENGTH EXPRESSION

If the production point and decay vertex could be determined without error, the decay length would simply be the distance between these points. However, consider the projection of the event in the r-φ plane shown in Figure 6.1. The centre of the beam spot (b) is known with an accuracy given by the error matrix σ_b, such that the error on b in the x direction is much larger than in the y direction, and the decay vertex (v) is known with an accuracy given by the error matrix σ_v.

The line (t) shows the direction of travel of the tau before decay. As the decay length is found from the position of v relative to b, v can be taken as a known point (x_v, y_v), with the error matrix,

$$\sigma = \sigma_b + \sigma_v$$

centred at b. The origin of the co-ordinate system is taken to be at b.

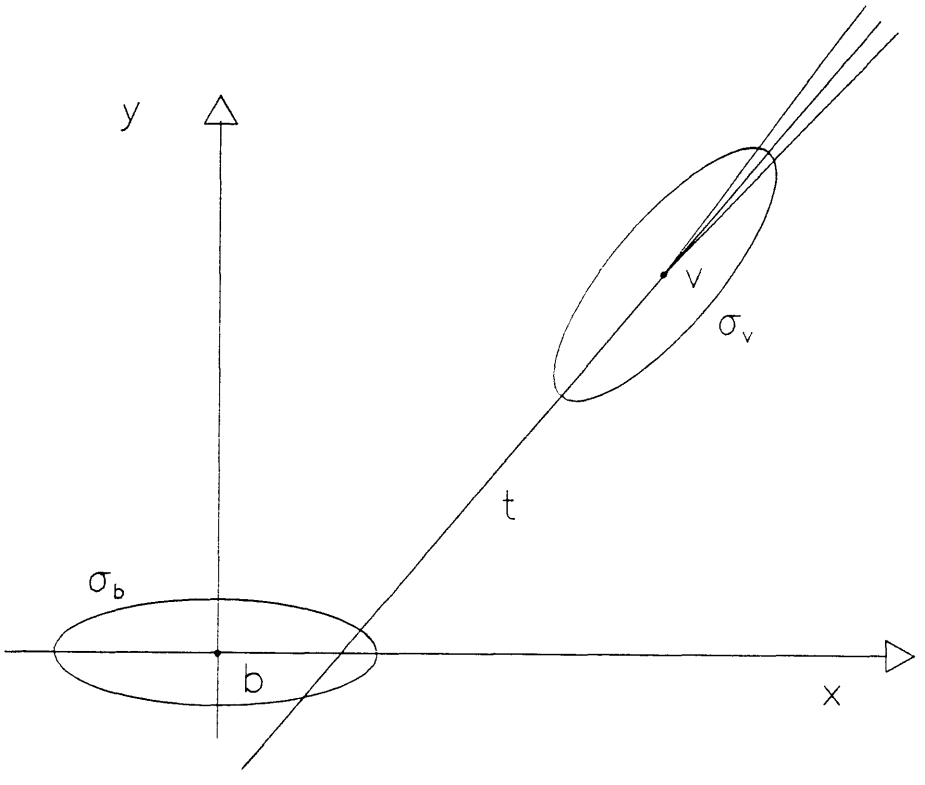

Figure 6.1: Errors on the Tau Decay Length

The simplest idea that the decay length is the separation between b and v, ignores the fact that the production point can occur anywhere within the finite sized beam spot. If the production point were constrained to lie on the line t, the direction of the tau could be used to find a better es-

timate of the production point within the beam envelope. The point of closest approach of the line t to point b is not the best estimate of the production point as the relative size of the errors at b are different in the x and y directions.

The best estimate of the production point p(x,y) within the beam spot is given by minimizing the quantity:

$$\chi^2 = [x,y]\ \sigma^{-1} \begin{bmatrix} x \\ y \end{bmatrix}$$

subject ot the constraint condition that the point also lies on the line t, given by:

$$t_y(x-x_v) = t_x(y-y_v)$$

where t_x and t_y are the direction cosines of the tau's direction of travel. When the χ^2 expression is minimized subject to this constraint condition, the decay length projected in the r-ϕ plane is found to be given by:

$$l = \frac{\sigma_{yy}x_v t_x + \sigma_{xx}y_v t_y - \sigma_{xy}(x_v t_y + y_v t_x)}{t_x^2\ \sigma_{yy} - 2\sigma_{xy}t_x t_y + t_y^2\ \sigma_{xx}}$$

where σ_{xx}, σ_{xy}, and σ_{yy} are the elements of the error matrix σ.

The geometric interpretation of this result is that the point p lies at the position where the line t is a tangent to one of the family of ellipses:

$$[x,y]\ \sigma^{-1} \begin{bmatrix} x \\ y \end{bmatrix} = \text{constant}$$

The error on the projected decay length (σ_l) is calculated from the expression for l and is found to be given by:

$$\sigma_l^2 = \frac{\sigma_{xx}\sigma_{yy} - \sigma^2_{xy}}{t_x^2\,\sigma_{yy} - 2\sigma_{xy}t_x t_y + t_y^2\,\sigma_{xx}}$$

6.3 VELOCITY OF THE DECAYING TAU

The expression for the projected decay length required the direction cosines of the decaying tau in the r-ϕ plane. The angle between the tau direction and the z-axis was needed for resolving this projected distance into the decay length in three dimensions. Then to convert the decay length into a proper decay time, the average γ factor of the taus needed to be estimated.

The direction of the tau in the r-ϕ plane was taken as the resultant momentum vector of the 3 track system in this plane. The angle between this vector and the z-axis was used to calculate the decay length from its projection on the r-ϕ plane. The direction of this 3 track system only gave the approximate direction of the tau due to missing momentum in the undetected neutrino and possible neutral particles. From Monte Carlo studies, the average separation

between this vector and the true direction of the tau, if there was only a missing neutrino, was 0.02 rad. A missing neutral pion increased this average separation to 0.03 rad. The distribution of this angle is shown in Figure 6.2. However, this approximation will be shown not to introduce a significant error into the calculated lifetime.

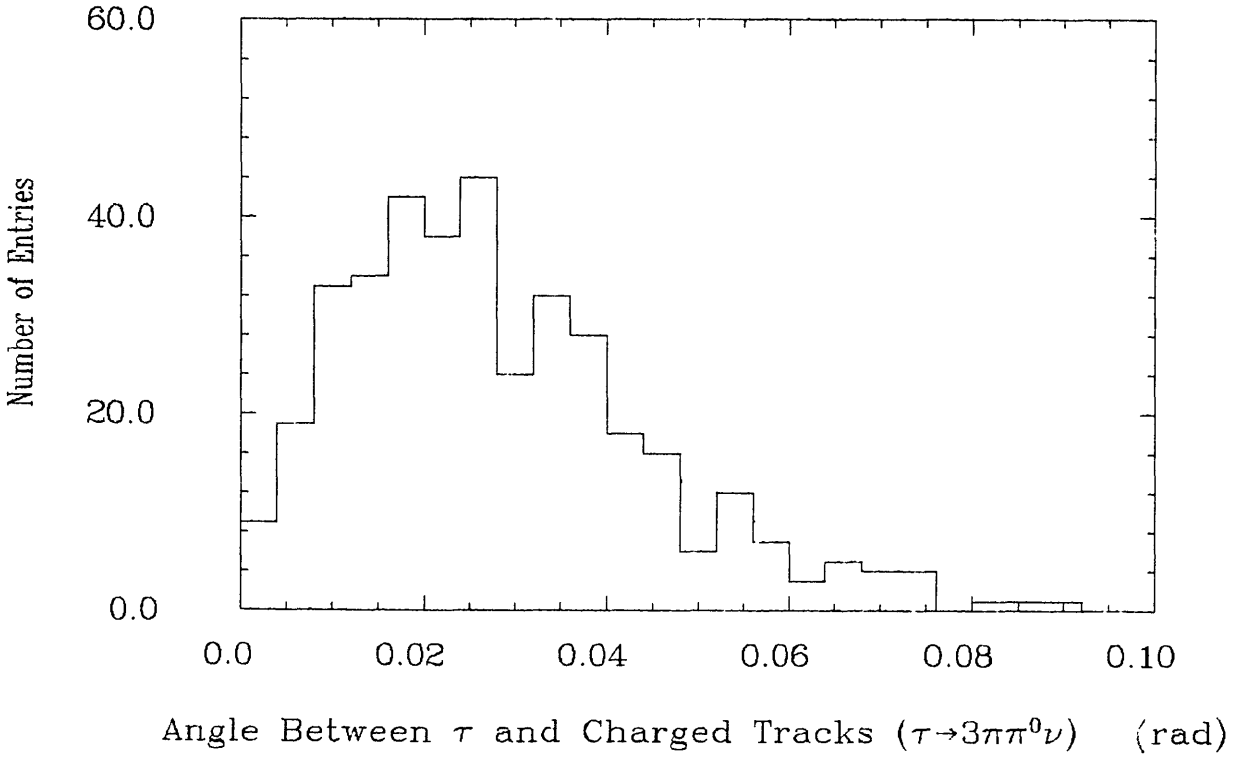

Figure 6.2: Angle Between Tau and 3 Track System

Due to radiative corrections, the energy of the tau system is on average less than twice the beam energy. As the energy cannot be measured from the charged decay products alone, the γ factor must be estimated using Monte Carlo events. Tau pair events were generated with radiative cor-

rections and selected using the same conditions as imposed on the data. Only those events that had a vertex successfully reconstructed were used when calculating the correction factor r which is given by:

$$r = E_t / E_b$$

where E_b is the beam energy and E_t is the energy of the tau. The γ factor is then given by:

$$\gamma = r\ E_b / m$$

where m is the mass of the tau. For the range of beam energies $20 \leq E_b \leq 22.5$ GeV, the correction factor was found to be 0.965.

6.4 LIFETIME DISTRIBUTION FUNCTION

A method is needed to extract the lifetime of a particle from a series of measurements of the decay length, each with its associated error. First it is necessary to convert each measured decay length (L) and error into a proper decay time and error (t,σ). These two quantities are related by the expression:

$$t = L / \beta\gamma c$$

where βc is the velocity of the particle and γ is the relativistic boost factor.

If the error on each measurement of the decay length was small, the times would be distributed with an exponential distribution:

$$g(t') = \exp(-t'/\tau) \; / \; \tau$$

and the maximum likelihood estimator of the mean lifetime τ is the arithmetic mean of the measured times (t') /33/.

However, the measured decay lengths were comparable to the experimental resolution, so for a given event the measured length could be positive or negative, as is shown in Figure 6.3.

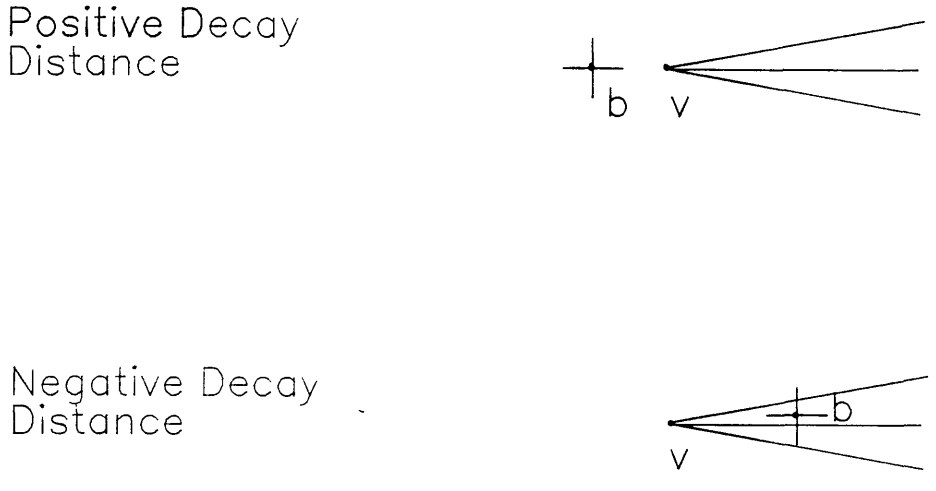

Figure 6.3: Positive and Negative Decay Lengths

Assume that the errors on the decay times (σ) are normally distributed and not dependent upon t. Then for each 'true' value of the decay time (t'), there is a measured value (t) which lies on the normal distribution function:

$$h(t,t') = \exp\left[-((t-t')/\sigma)^2 / 2\right] / \sqrt{(2\pi)}\,\sigma$$

The distribution which describes the measured decay times is then the convolution of these exponential and resolution functions:

$$f(t) = \int_0^\infty g(t')\, h(t,t')\, dt'$$

This integral can be evaluated /33/ to give the probability density function:

$$f(t) = \tfrac{1}{2}\exp[\sigma^2/2\tau^2 - t/\tau]\ \mathrm{erfc}[(\sigma/\tau - t/\sigma)/\sqrt{2}] / \tau$$

where the function erfc[x] is defined by:

$$\mathrm{erfc}[x] = (2/\sqrt{\pi}) \int_x^\infty \exp[-y^2]\, dy$$

The form of this function is shown in Figure 6.4 for various ratios of the resolution (σ) to the lifetime (τ). When the resolution to lifetime ratio is large, the function approaches a Gaussian distribution, but when the resolution is comparable to the lifetime, a clear exponential tail to the distribution is observable.

The maximum likelihood estimator of τ for n measurements of (σ,t) is given by minimizing the log likelihood function:

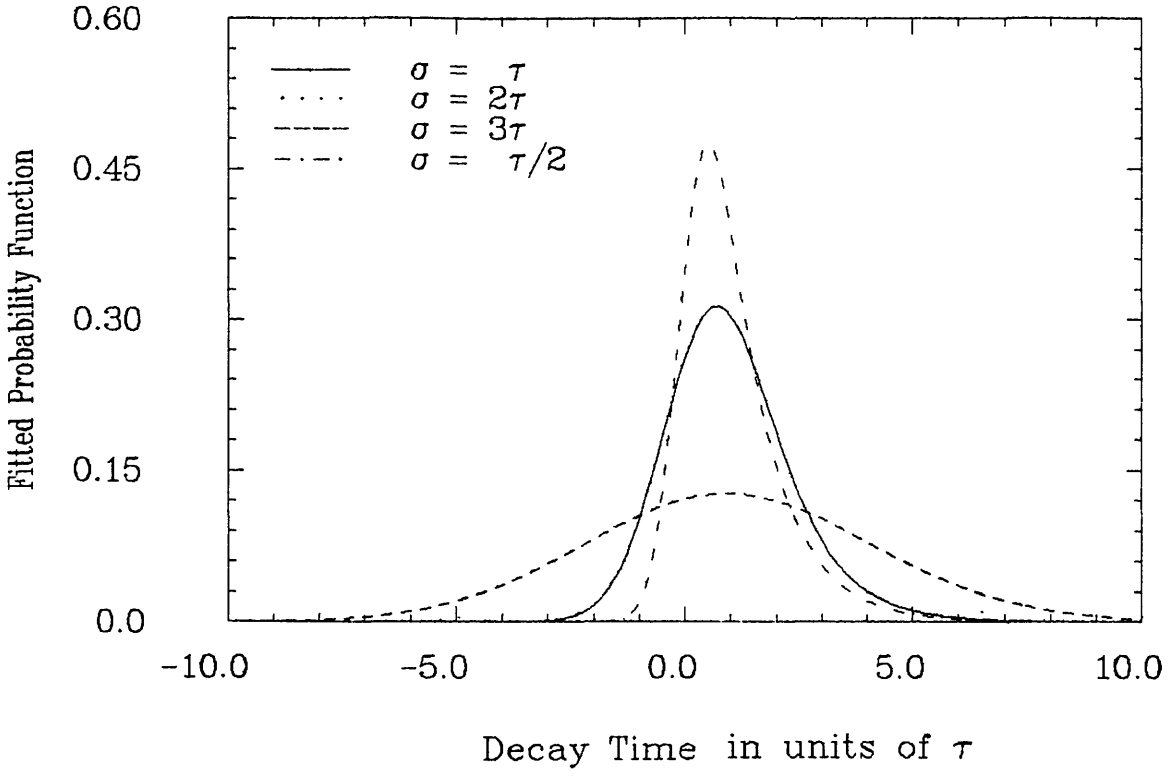

Figure 6.4: Lifetime Distribution Functions

$$L = - \ln \prod_{i=1}^{n} f(t_i)$$

This minimization was performed numerically using the minimization and error analysis program package MINUIT /34/. The one standard deviation likelihood interval σ_τ on the fitted parameter τ, was obtained by following the function out of the minimum to the point where its value was 0.5 greater than at the minimum /33/. In general this method produces asymmetric errors, whereas the method of assuming a parabolic shaped likelihood function calculated from the curvature at the minimum, produces positive and negative errors of the same magnitude.

6.5 BEAM SPOT

6.5.1 Introduction

A method was needed to find the position of the tau production point. The accuracy with which this point could be found depended on three factors: the size of the beams (σ_x,σ_y) in the x and y directions, the ability to track systematic shifts in the centre of the beam position (x_b,y_b) over a long time, and the precision (Δx_b,Δy_b) with which the centre of the beam could be determined.

The procedure to find the beam spot centre was based on fitting a common vertex to tracks from a number of events originating from the interaction region. The common vertex was taken as the production point, with the spread of distances of closest approach for horizontal and vertical tracks to the vertex being used to obtain an estimate of the beam spot dimensions in the y and x directions.

6.5.2 Event Selection

Data from the Two Prong selection procedure were used as the basis for further event selection because they provided the largest available source of low multiplicity events where the background from beam-gas and beam-pipe interactions had been suppressed. There was a need to eliminate beam-pipe interactions where all the tracks had $d_0 \leq 2.5$ cm. The point of intersection of each pair of tracks within the event was calculated and only those events that had all

tracks intersecting within 5 cm of the origin were selected. This removed track vertices that originated from the beam pipe.

The PASS5 track-finder was used to search for tracks within the vertex detector. This track-finder had the advantage over FELIX that the tracks which were found were not biased by any error in the assumed relative chamber alignments. The beam spot was measured relative to the vertex detector and any subsequent improvement in the determination of relative chamber alignments was used when transforming the beam spot into the co-ordinate system of the large drift chamber.

6.5.3 Track Selection

Groups of 50 tracks from successive events over several experimental runs were selected using the following conditions.

1. Each track must have $d_0 \leq 0.3$ cm and be reconstructed in three dimensions.
2. The difference between the measured and predicted time of flight to the ITOF counters must be less than 3 ns.
3. At least 4 hits in the vertex detector must be associated with each track.

The d_0 used in condition (1) was the d_0 relative to the estimated beam spot position (i.e. the point of closest ap-

proach of the track to the beam spot). This cut was loose enough not to bias the final beam spot position but helped to remove tracks not coming from the interaction point, and spurious tracks from errors in the track finding procedure. Condition (2) removed cosmic ray events with the track passing close to the origin. Condition (3) was a requirement of the PASS5 track-finder to reconstruct a track within the vertex detector.

With 50 tracks, the beam spot centre could be determined to the order of 100 μm. However, this required tracks to be taken from a period covering more than a single data taking run. This was necessary as a run lasting several hours was required to produce 50 selected tracks and many runs lasted a much shorter time.

6.5.4 Vertex Constraint Fit

A vertex constraint program package /35/ was used to estimate the beam spot centre for each group of 50 tracks. Rather than simply finding a vertex that minimized the sums of the distances to all the tracks, an expression for the χ^2 probability was constructed which also took account of the size of the beam spot. From PETRA machine group studies, the beam spot at the interaction region was estimated to have a σ_x of 500 μm and a σ_y of 60 μm. Therefore, the interaction vertex is more likely to be further from the beam spot centre in the x direction than in the y direction.

Using the variables shown in Figure 6.5, the following χ^2 expression is formed:

$$\chi^2 = \sum_{i=1}^{\text{tracks}} \frac{d_i^2}{\sigma_r^2 + \sigma_i^2} + \frac{(x_i - x_b)^2}{\sigma_x^2} + \frac{(y_i - y_b)^2}{\sigma_y^2}$$

where $v(x_i, y_i)$ is the vertex position calculated for track (T) and d_i is the shortest distance from this vertex to the track. σ_r is the resolution at the origin due to tracking and chamber resolution. The resolution at the origin due to multiple scattering in the beam pipe material (σ_i) is calculated for each track as it is dependent on the momentum of the track. Hence the first term in this χ^2 expression is a measure of the probability that the vertex is a distance d from the reconstructed track. The second and third terms in the expression are a measure of the probability that the vertex is a certain distance in the x and y directions from the centre of the beam spot $b(x_b, y_b)$.

The beam spot position was found by minimizing this χ^2 expression with respect to x_b and y_b. As an analytic solution exists for the position of the vertex that minimizes this χ^2 expression for a given beam spot position, x_i and y_i could be eliminated from the expression. The χ^2 expression was then numerically minimized with respect to x_b and y_b. The errors on x_b and y_b were calculated from the second derivatives of the χ^2 expression.

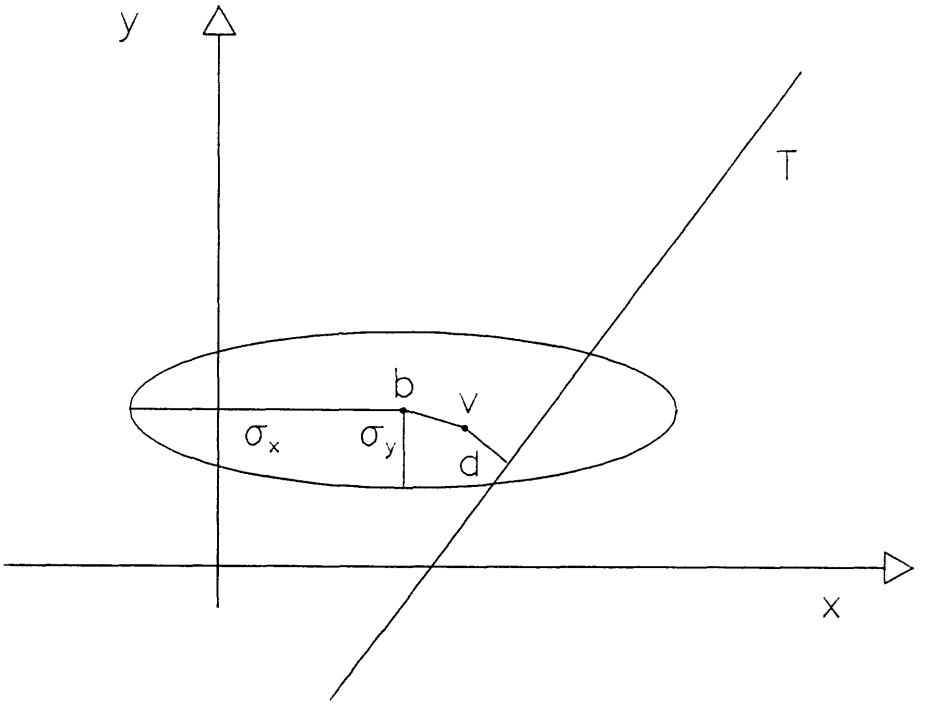

Figure 6.5: Variables Used to Find Beam Spot

The values given to σ_x and σ_y in the χ^2 expression were those measured by the PETRA machine group. Later, when the beam size is estimated from the spread of distances of closest approach of tracks to the calculated beam position, these values are shown to be reasonable.

6.5.4.1 Multiple Scattering Term

One factor that worsened the d_0 resolution of a track was the multiple scattering in the material between the interaction point and the vertex detector. An estimation of the effect of this scattering on the d_0 resolution was obtained using a Monte Carlo method. Single pion events were gener-

ated with a similar momentum distribution to the selected data and passed through the TASSO detector simulation. The tracking chambers were given perfect resolution, all tracks were generated at a common point and were scattered in the beam pipe material. The momentum distribution of the data was described reasonably well by an exponential distribution with a 0.5 GeV/c decay constant and a lower cut off point of 0.25 GeV/c. The d_0 distribution for all generated tracks, had a standard deviation of 140 ± 10 μm.

6.5.4.2 Resolution Term

The d_0 resolution is also dependent on the vertex detector point resolution and effects from errors in the track finding procedure. An estimation of these effects was made using the Monte Carlo method previously described except that the scattering simulation was removed and the point resolution in the vertex detector was set to 150 μm. The d_0 distribution relative to the beam spot for all generated tracks, had a standard deviation σ_r = 270 ± 10 μm.

6.5.5 Results

Figures 6.6 and 6.7 show the position of the beam spot centre in the x and y directions against run number. The 1500 runs shown covered data taking over a period of 9 months. There is one entry in each figure for each determination of the beam spot, even if the data spanned several runs. The

beam position was considerably more stable in the y direction than the x direction. The movement of the beam in the x direction may have been due to small changes in the radius of the beam orbit. The sharp discontinuity around run 7400 corresponded to a long shut-down of the experiment when both the focussing quadrapoles and the detector could have been moved. However, there is a clear systematic drifting of the x position by about 1 mm over long periods. The average over all groups of tracks of the error on the beam spot centre was 85 μm in the x direction and 60 μm in the y direction.

TABLE 8

Dependence of Beam Spot Error on Assumed Beam Size

σ_x	σ_y	Δx_b	Δy_b
500	60	85	60
500	100	80	60
300	40	60	55
800	150	110	70

To check the effect of the assumed beam size on the average value of Δx_b and Δy_b, various values of σ_x and σ_y were input into the χ^2 expression. Table 8 shows the results. The effect of varying the assumed beam size in the y direc-

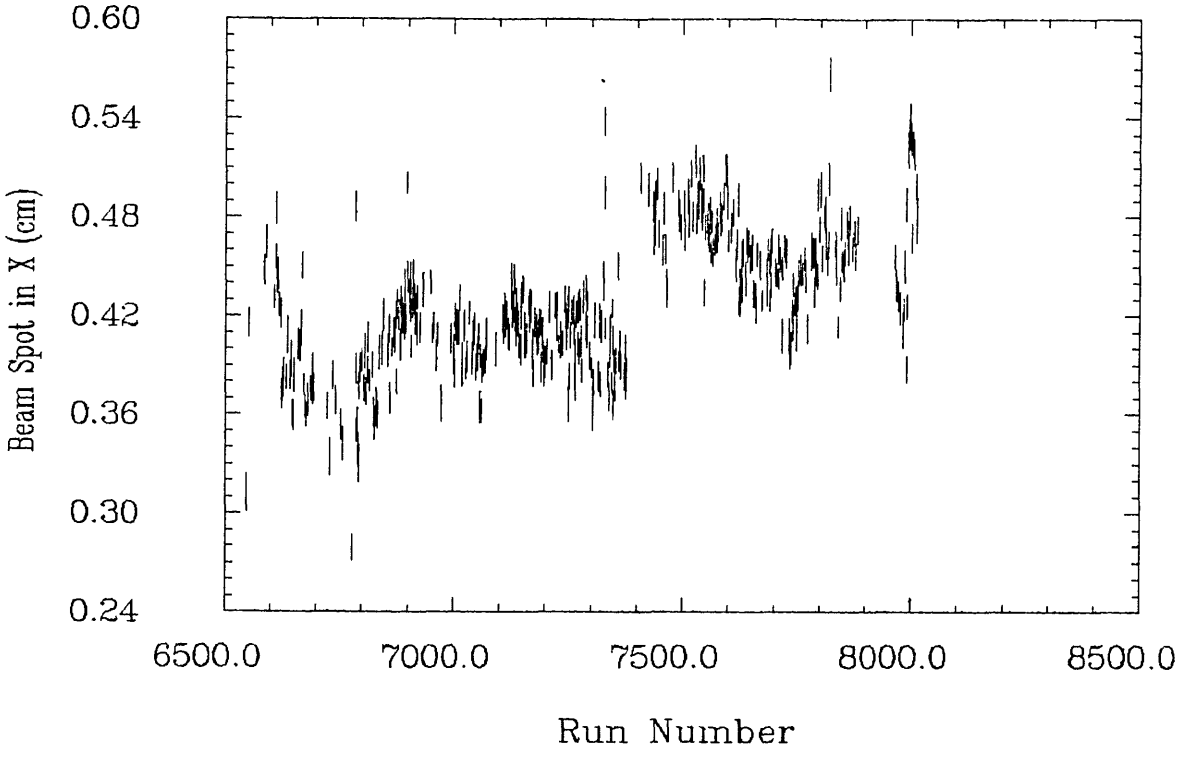

Figure 6.6: x Beam Position against Run Number

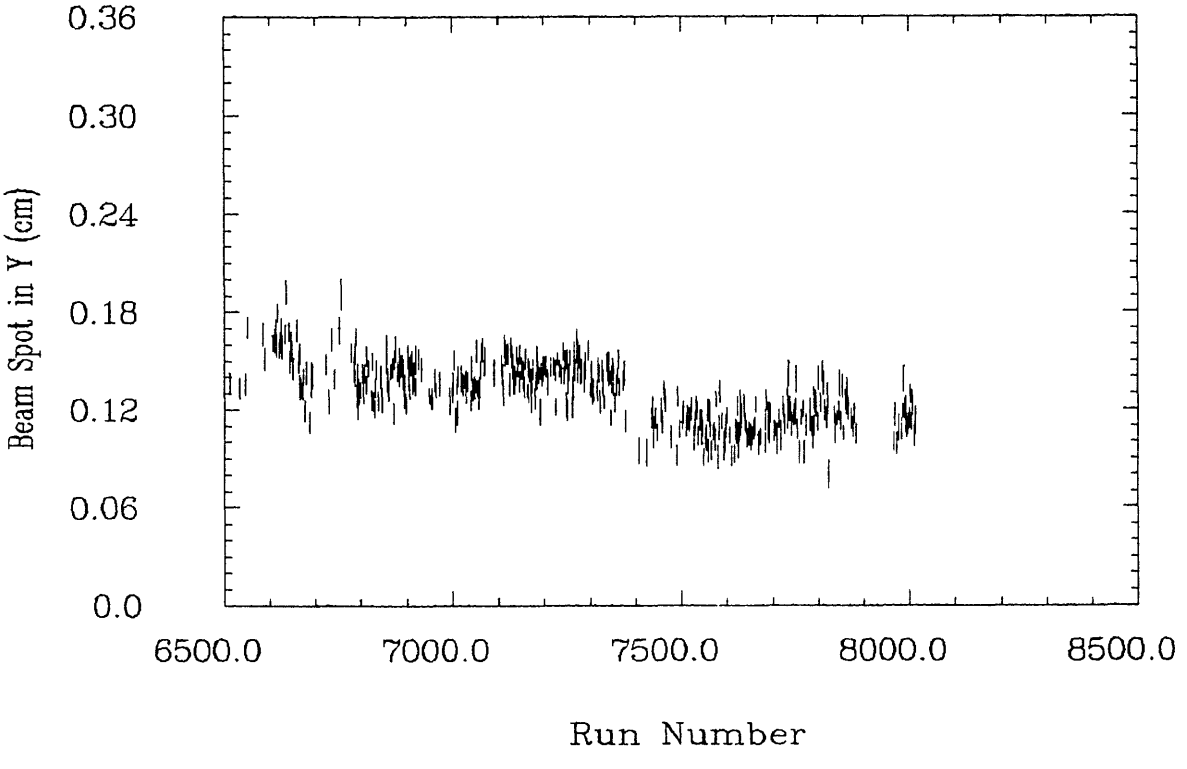

Figure 6.7: y Beam Position against Run Number

tion had little effect, while the errors scaled with changes in the assumed beam size in the x direction. This is to be expected as the size of the beam in the y direction is small compared to the chamber resolution, while in the x direction the beam size and chamber resolution have similar values.

Finally, as a check that the method could find the beam spot position correctly, Monte Carlo events were generated as previously described from a beam spot with σ_x = 350 μm and σ_y = 150 μm, and then passed through a detector simulation that included the effects of scattering and resolution. The vertex constraint program was run on groups of 50 tracks. The RMS difference between the reconstructed beam spot centre and its true centre was 95 μm and 69 μm in the x and y directions respectively, showing that the method worked and the errors produced were reasonable.

6.5.6 Beam Size

The beam size in the x (y) direction was measured by analysing the distance of closest approach (d_0) of the vertical (horizontal) tracks to the beam spot centre. For a truly vertical track, d_0 is a measurement of the x co-ordinate of the interaction vertex relative to the beam centre. However, for the purpose of selecting tracks, a tolerance (ω) needed to be set for the allowed angular deviation from the vertical (horizontal) plane. Using the estimate of the beam dimensions provided by the machine group, values of ω could

be chosen such that no significant extra error was introduced in determining the beam dimensions.

Consider the track shown in Figure 6.8 that is at an angle ω to the horizontal plane. The maximum possible deviation of the interaction vertex (δy) from the measured d_0 position such that the vertex still occured within the beam envelope is given by:

$$\delta y = \sigma_x \tan \omega$$

Therefore, using the estimate that σ_x = 500 μm, δy was limited to ± 25 μm by setting the upper limit on ω to be 50 mrad. In a similar calculation for the vertical tracks with σ_y = 60 μm, δx was limited to ± 15 μm by setting the upper limit on ω to be less than 250 mrad.

The horizontal and vertical tracks were selected from Bhabha scattering events that were produced during the standard data reduction procedures. The advantage in using this data, instead of the data used to find the beam position, was that the errors on d_0 due to scattering in the beam pipe material were negligible. The smaller quantity of data was acceptable as only one measurement of the beam size was being made for the whole range of runs. For tracks with a momentum of 2 GeV/c, there is only a 40 μm uncertainty in d_0 from multiple scattering.

This data sample was selected from PASS2 events containing only two tracks using the following criteria.

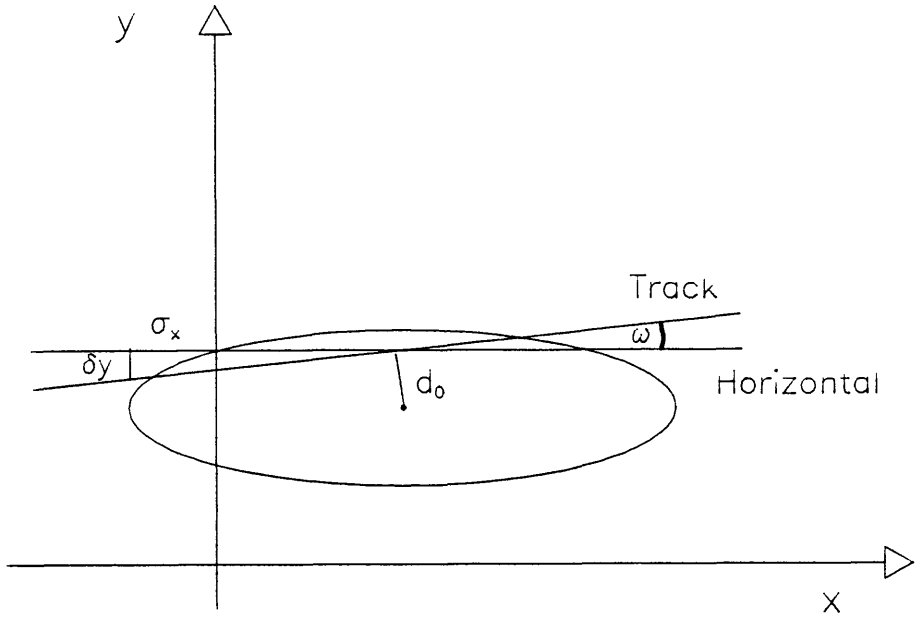

Figure 6.8: Selection of a Horizontal Track

1. Each track had to have $d_0 \leq 0.4$ cm and $|\cos\theta| \leq 0.8$. The two tracks had to have a mean z_0 of 4 cm and be collinear within 10°.
2. The difference between the measured and predicted time of flight to the ITOF counters must be between -3 ns and 2 ns.
3. Each track had to have $P > 0.2\ E_b$, where E_b is the beam energy. The sum of the magnitudes of the momenta of the tracks had to be greater than $0.7\ E_b$.

Criterion (1) selects tracks from the interaction region within the detector acceptance, criterion (2) removes cosmic ray events and criterion (3) demands that most of the available beam energy is seen in the tracks.

Figure 6.9 and Figure 6.10 show the d_0 distribution for the selected horizontal and vertical tracks relative to the previously determined beam position. The standard deviations of the fitted Gaussian functions give:

$$\sigma_x = 436 \pm 9\ \mu m \qquad \sigma_y = 298 \pm 13\ \mu m$$

However, the d_0 resolution of the chamber is folded into these values. To estimate the d_0 resolution for these events with a method that is independent of the beam centre, the difference in d_0 between the two tracks was plotted. This gave a Gaussian distribution with a standard deviation of 395 ± 3 μm. Thus, the d_0 resolution on a single track was 280 ± 2 μm.

If the d_0 resolution contribution to the above value for σ_x is removed, the size of the beam spot in the x direction is 335 ± 12 μm. The beam size in the y direction is unable to be measured with the present detector resolution. In conclusion, the known position of the interaction vertex is limited in the x direction by the size of the beam envelope and in the y direction by the accuracy with which the beam centre has been determined.

Combining the errors on the beam position and the beam size, a value of:

$$\sigma_x = 350\ \mu m \qquad \sigma_y = 100\ \mu m$$

will be used as the errors on the position of the tau production point.

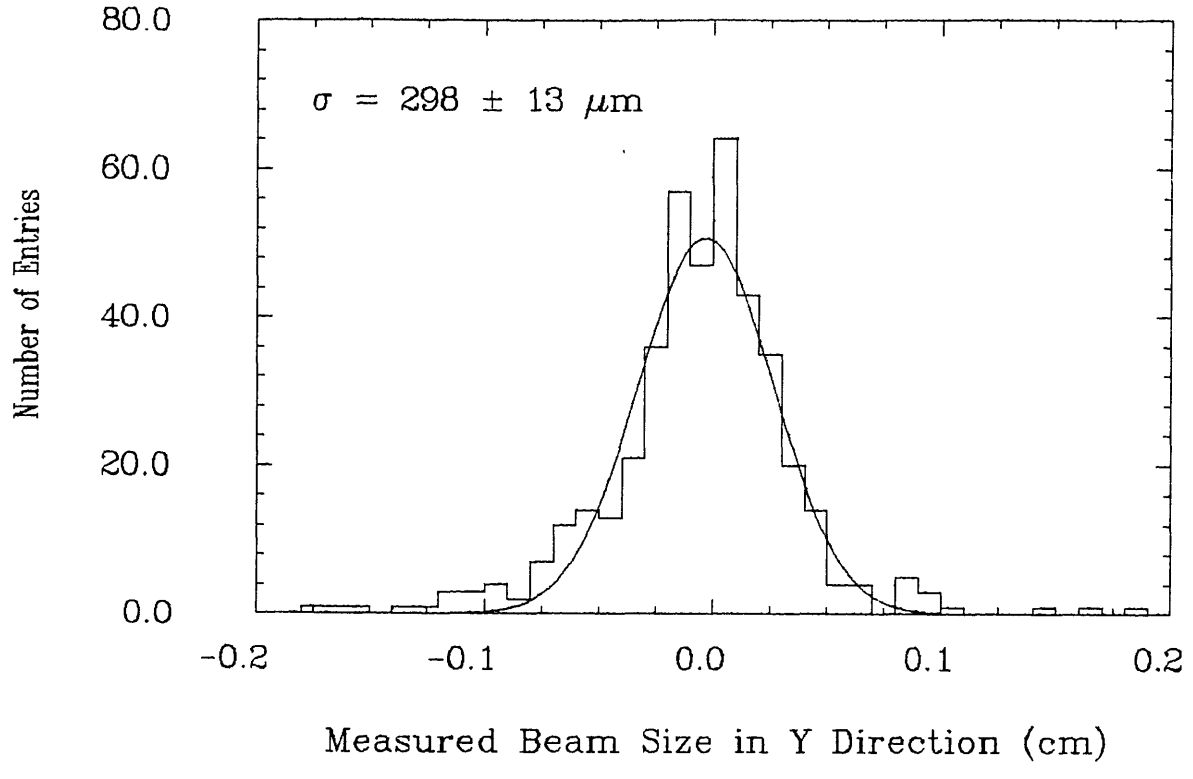

Figure 6.9: d_0 Distribution for Horizontal Tracks

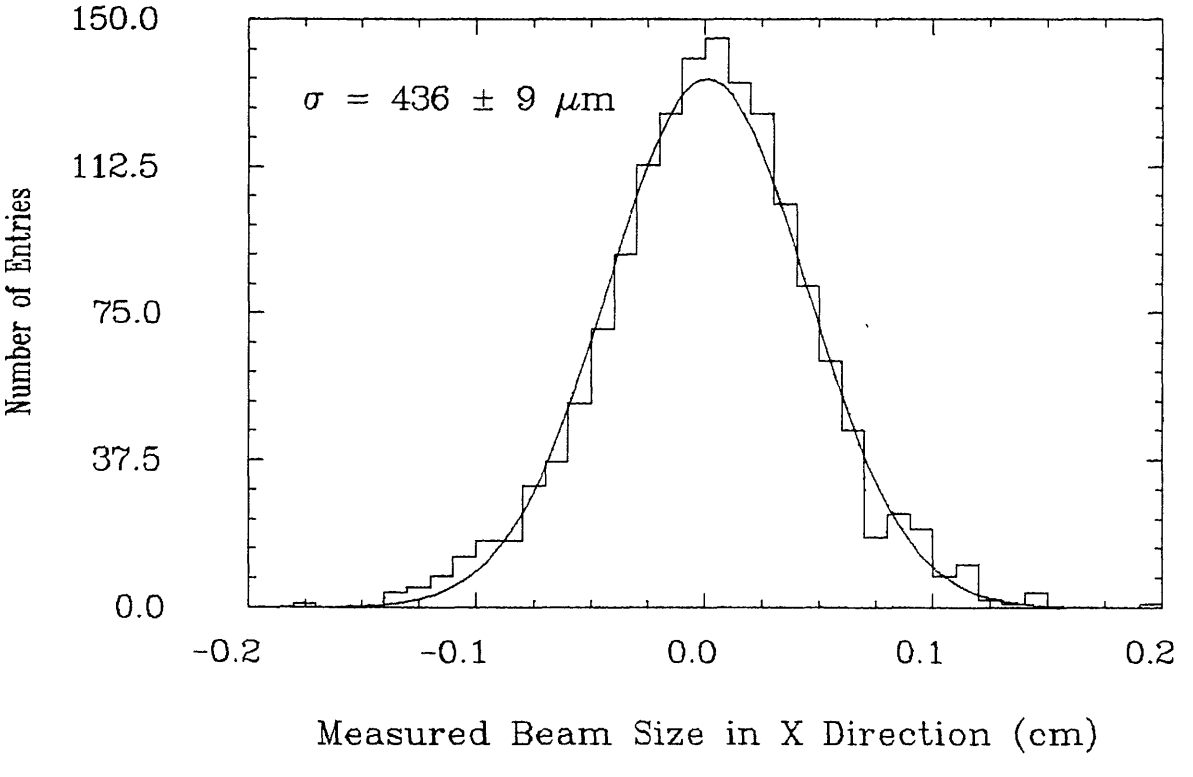

Figure 6.10: d_0 Distribution for Vertical Tracks

6.6 VERTEX FITTING

The tau decay point was found by fitting three charged tracks to a common vertex. The procedure used by the vertex constraint package /35/ will be described briefly. Basically, the program took hits that had been associated to tracks in the large drift chamber and vertex detector, refitted the tracks allowing a kink in the circle fit between the two detectors to account for multiple scattering, rejected hits if they were considered incorrectly associated to a track, and then constrained the tracks to a common point.

Hits were associated to tracks by the FELIX track finding program in both the large drift chamber and vertex detector, or alternately, the results from the hit association of MILL in the large drift chamber and PASS5 in the vertex detector were combined.

To model scattering in the r-ϕ plane in the material between the two detectors, 0.06 radiation lengths of material was assumed to be concentrated at a radius of 16 cm from the interaction region, the position of the vertex detector pressure vessel.

Each track was refitted in two dimensions by minimizing the following χ^2 expression with respect to the track's curvature, d_0, ϕ_0 and scattering angle θ:

$$\chi^2_t = \sum_{j=1}^{hits} d_j^2 / e_j^2 + \theta^2/s^2$$

where d_j is the distance of a hit to the fitted track, e_j is the error on the hit position and s is the RMS scattering angle given by /36/:

$$s = 0.015 \sqrt{l} / P_t$$

where l is the thickness of the material in radiation lengths and P_t is the transverse momentum of the track. If there were less than 3 hits in the vertex detector, the scattering term was not included in the χ^2 expression.

The χ^2/NDF distribution, where the number of degrees of freedom (NDF) was the number of hits minus the number of free parameters, peaked around 1.0. If the track had a χ^2/NDF $\geq$ 2.0, up to three hits could be removed from the track in an attempt to reduce the value below 2.0. Bad point rejection was only done at this stage, as rejecting points during a vertex constraint fit would help to form a vertex from tracks that did not originate from a common point.

The χ^2 expression to be minimized for the vertex fitting procedure was similar to the one used for track fitting except now due to the extra constraint, the minimization was with respect to each track's curvature, ϕ_0, scattering angle θ and the (x,y) co-ordinates of the vertex position. The χ^2 expression is given by:

$$\chi^2_v = \sum_{i=1}^{\text{tracks}} \sum_{j=1}^{\text{hits}} d^2_{ij}/e^2_{ij} + \theta^2_i/s^2_i$$

where the summation is now also over the three tracks being fitted to the vertex. The minimization was performed numerically using analytic expressions for the first and second derivatives of the χ^2 with respect to the fit parameters. The minimization procedure, if successful, gave the position and error matrix of the vertex.

The increase in χ^2 due to the vertex fit is given by:

$$\Delta\chi^2 = \chi^2_v - \sum_{t=1}^{\text{tracks}} \chi^2_t$$

This change in χ^2 should have the χ^2 distribution for the extra number of degrees of freedom due to the vertex fit. The extra number of degrees of freedom is equal to the number of tracks in the fit minus two, as each track can be described by three parameters and the common vertex, instead of the usual four parameters $(\phi_0, d_0, r_0, \theta)$. This fact will be used later when checking the error matrix produced from this fitting procedure.

6.7 LIFETIME MEASUREMENTS ON MONTE CARLO EVENTS

6.7.1 Introduction

Having found an expression for the decay length, the method was first used on Monte Carlo events to check that a known lifetime could be reproduced without bias and that the errors given by the fitting programs were reasonable. Effects on the lifetime measurement due to a possible error in the measured position of the beam spot or vertex detector with respect to the large drift chamber were also studied.

6.7.2 Events Generated

Monte Carlo events were generated which decayed into a 1+3 charged track topology. Three groups of events were generated with tau lifetimes of 0.0 s, 2.7×10^{-13} s and 5.4×10^{-13} s. At a centre of mass energy of 42.5 GeV, this corresponded to mean decay lengths of 0 μm, 925 μm and 1850 μm respectively. Radiative corrections were included in the generator. The tau production point lay within the beam envelope that had an error ellipse with a diameter of 1000 μm in the x direction and 200 μm in the y direction. The decay products were passed through the full TASSO detector simulation program.

Charged tracks were reconstructed using the MILL, PASS5 and FELIX track finding programs. Those events that were to be used in the vertex fitting were selected using the same selection procedure as used with the experimental data. Around 500 events were generated in each lifetime group.

6.7.3 Vertex Fitting

The vertex fitting program tried to reconstruct the decay vertex for each selected event. As discussed earlier, the increase in χ^2 for a 3 track vertex fit ($\Delta\chi^2$) has the χ^2 distribution for one degree of freedom. Only events with a $\Delta\chi^2 < 5.0$, which should include 97.5 % of all good vertices, were used in the lifetime measurement. From a visual scan of displayed event vertices, it was noted that events with a larger $\Delta\chi^2$ than this value usually had wrong hit association to the tracks and the reconstructed vertex was not reasonable.

If $\Delta\chi^2$ has a χ^2 distribution for one degree of freedom, the probability (P_χ) that $\Delta\chi^2$ would have a higher value is a flat distribution. Figure 6.11 shows this probability distribution for events with a reconstructed vertex. The fact that the distribution is not skew with an excess of events with a low (high) P_χ indicates the errors used in the vertex fit were not under (over) estimated.

As a further check that the errors were reasonable, the distribution of $1/\sigma_1$, for the zero lifetime group of events, was fitted with a Gaussian function. If the errors were correct, the distribution should be a Gaussian with unit width. Figure 6.12 shows the distribution together with the fitted Gaussian and a superimposed unit Gaussian. The standard deviation of the fitted function was 1.07 ± 0.06 showing the errors were in fact reasonable.

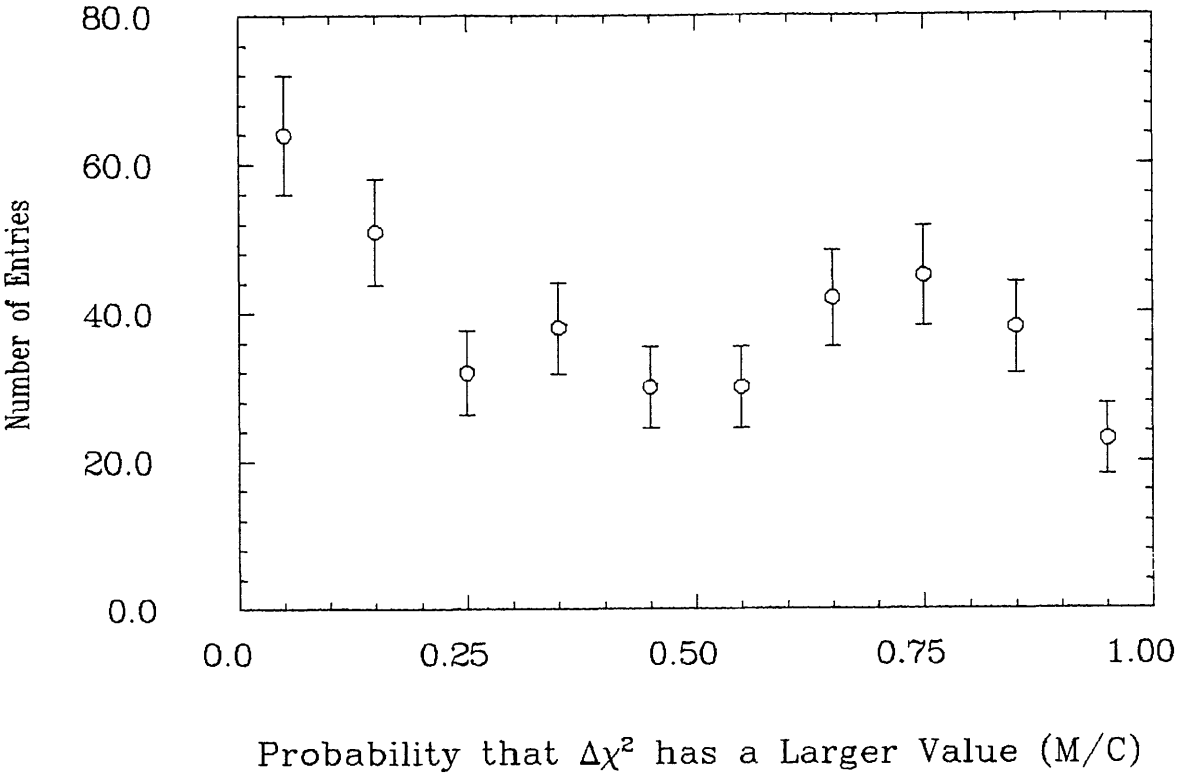

Figure 6.11: Probability that Vertex Fit has a Larger χ^2

The vertex fitter was able to reconstruct vertices for 77 % of events when using MILL/PASS5 tracks and 86 % of events when using FELIX tracks. The failure rate was higher with PASS5 tracks because the track-finder had not always been able to reconstruct all tracks in the 3 track system. Reconstruction failed or there was incorrect hit association when the opening angle of the 3 track system was so small that two or three tracks went through the same drift cell in the vertex detector. The FELIX track-finder was more successful in reconstructing closely spaced tracks as the search in the vertex detector was just extending the tracks found in the large drift chamber.

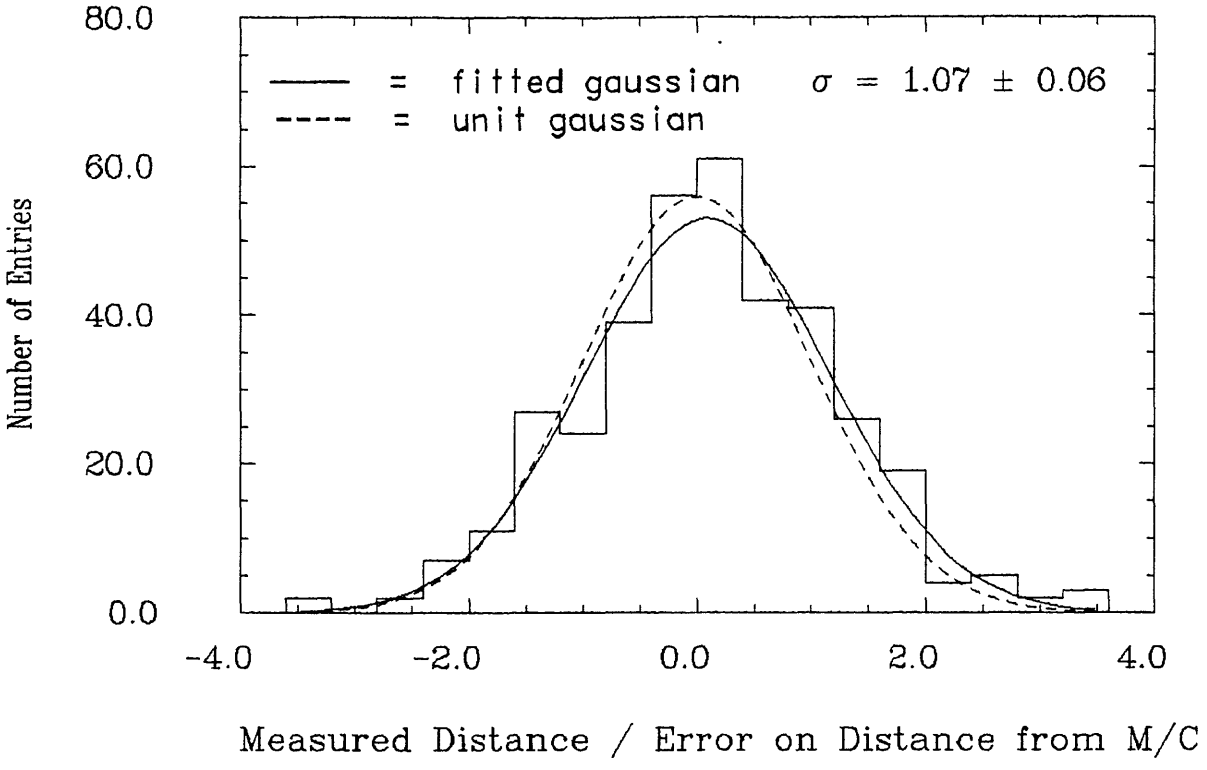

Figure 6.12: Distance / Error for Events with Zero Lifetime

6.7.4 Likelihood Functions

The lifetime for each group of Monte Carlo events was obtained from the measured decay times and errors using maximum likelihood fits. The fitted function for each group of events with a finite lifetime was the convolution of an exponential and Gaussian that was discussed earlier. Unfortunately, this function is numerically unstable when the lifetime is much smaller than the errors. To overcome this problem, a power series expansion of the function /37/ was used when ever the argument of the error function exceeded 5.7. If the likelihood function is plotted as a function of lifetime for the zero lifetime group of events, its value is

least around zero. However, as the function is undefined for negative lifetimes, its minimum and the error on the lifetime cannot be found. Instead, for this group of events, the large error limit was taken and only the Gaussian resolution function was fitted, with the lifetime being the mean value of the function found from the fit.

6.7.5 Monte Carlo Results

The lifetime input into the Monte Carlo and the lifetime found by these fits are summarized in Table 9 for each group of events. The times are in units of 10^{-13} seconds.

TABLE 9

Monte Carlo Lifetimes Using PASS5 and FELIX

Generated Lifetime	Measured Lifetime PASS5	Measured Lifetime FELIX
0	0.3 ± 0.2	0.3 ± 0.2
2.7	2.8 ± 0.2	3.0 ± 0.2
5.4	5.2 ± 0.3	5.8 ± 0.3

The distribution of lifetimes for each group of events from PASS5 tracks is plotted in Figure 6.13. The fitted curves were obtained by taking the maximum likelihood esti-

mate of the lifetime as fixed and fitting the width of the resolution function and normalization factor by a least squares method.

After the lifetime has been obtained from the decay time data, a radiative correction is made to its value which takes account of the average 3.5 % loss in the tau energy. The calculation of this correction was discussed earlier. Hence the radiative correction has not been made on the data shown in the diagrams, but has been made on the times discussed in these results.

There is no significant bias in the measured lifetimes with the use of either track-finder. All measured lifetimes lie within $\pm$ 0.4 x 10^{-13} s of the generated lifetime. The width of the resolution function in all groups of Monte Carlo events is around 3.6 x 10^{-13} s, which corresponds to a vertex resolution distance of 1240 μm.

Similar results were obtained when considering Monte Carlo events in which the tau was allowed to decay to a π^0 and 3 charged pions. A lifetime of (2.9 $\pm$ 0.3) x 10^{-13} s was measured when using PASS5 tracks. The effect of the missing neutral particles on the measured lifetime is negligible.

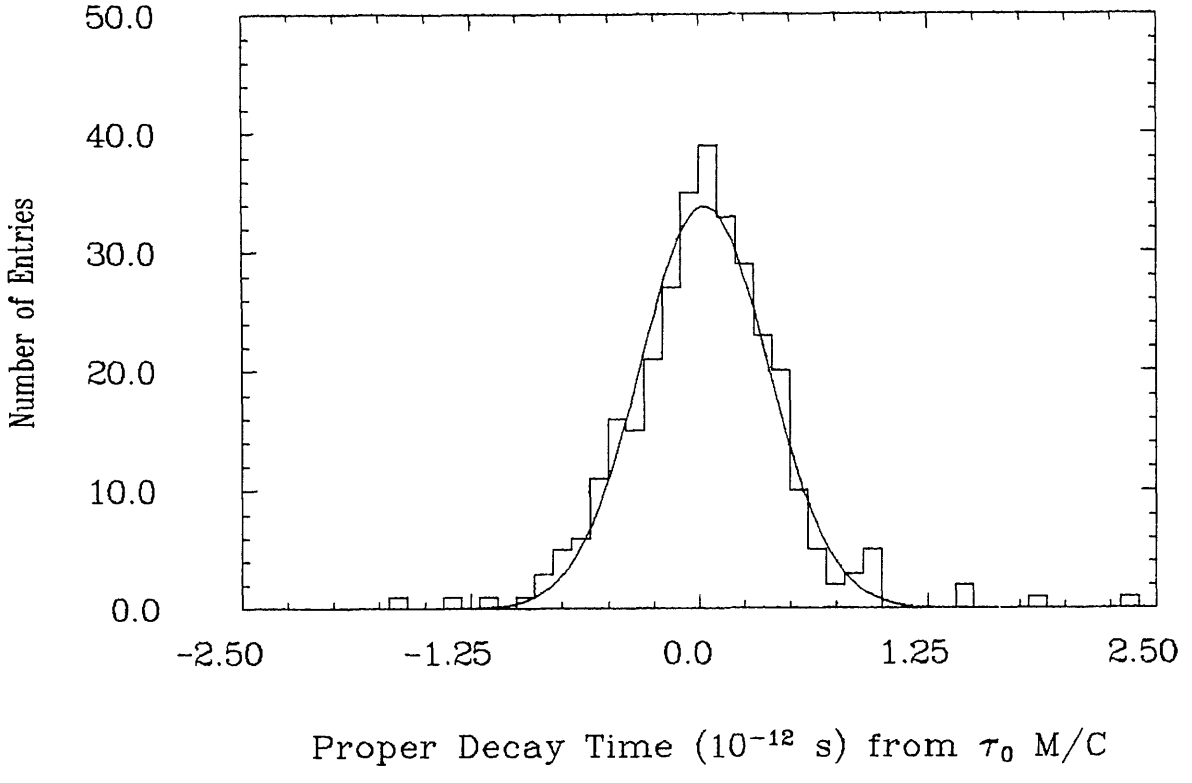

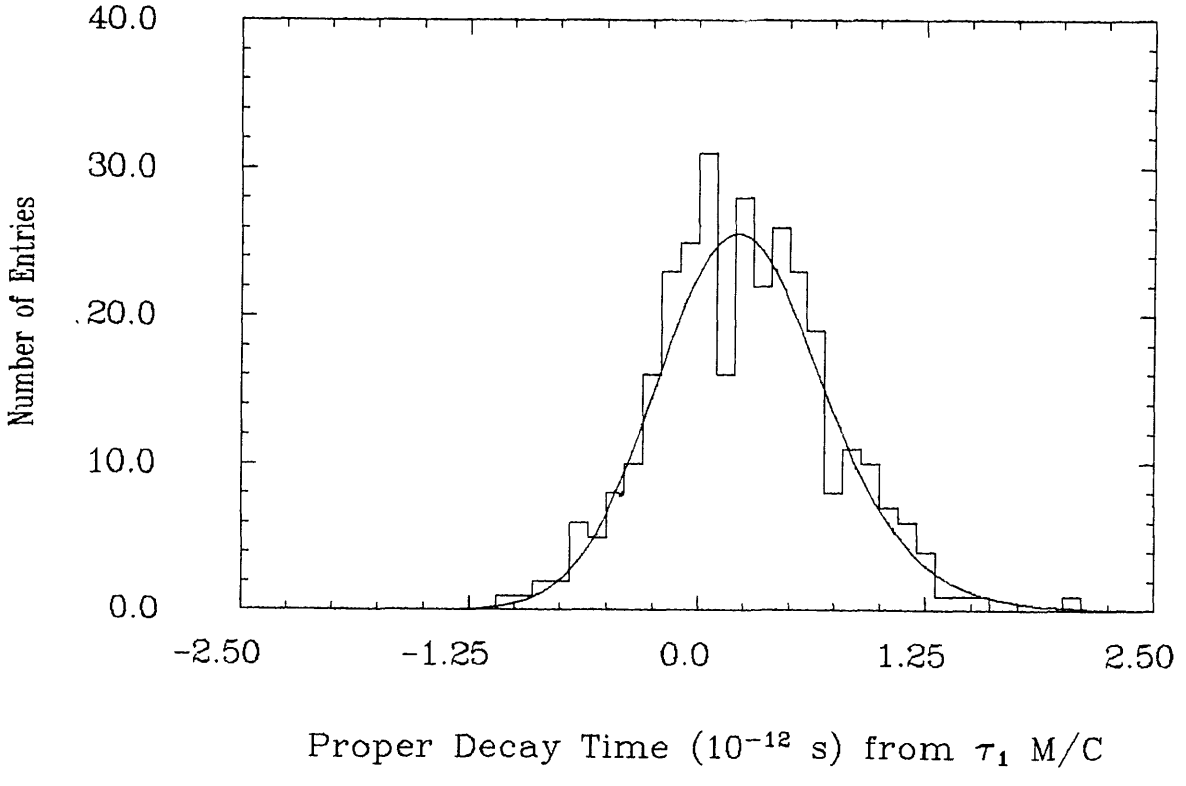

Figure 6.13: Lifetime Distributions from Monte Carlo Events

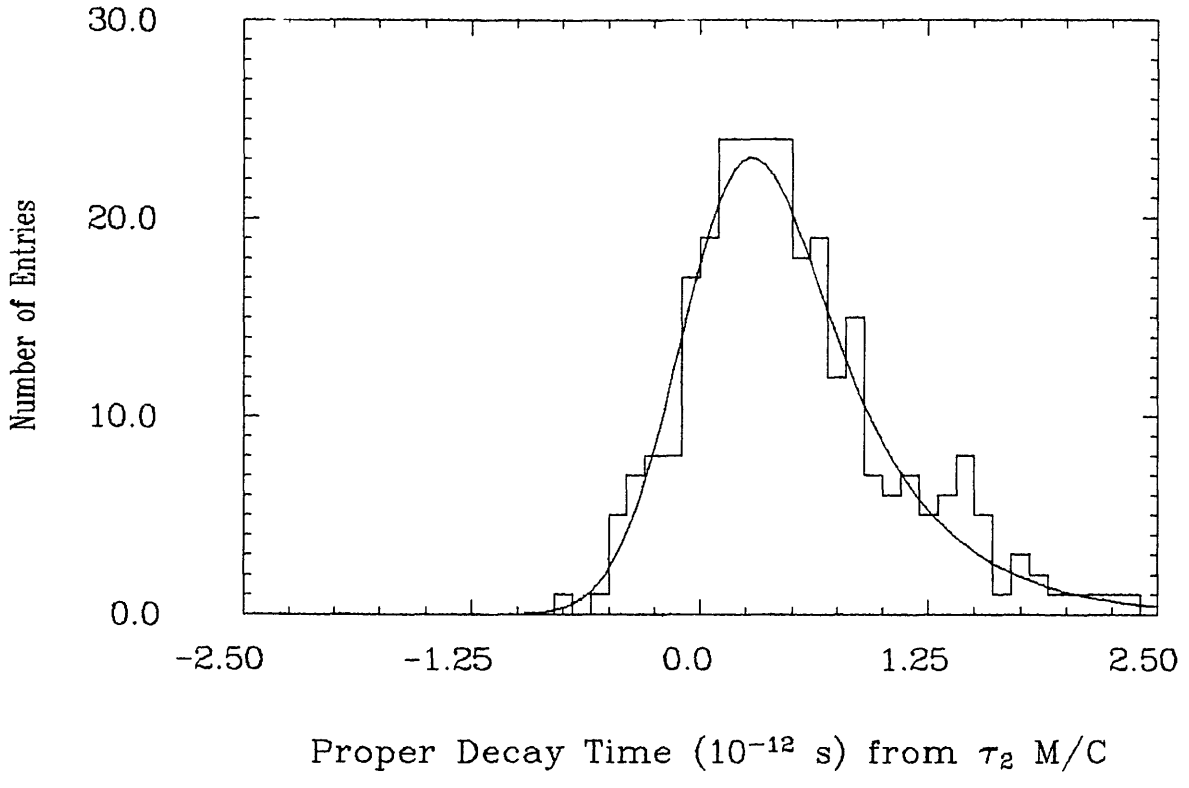

Figure 6.13: Lifetime Distributions from Monte Carlo Events

6.7.6 Effect of Error in Detector or Beam Position

So far in these Monte Carlo events, the relative position of the vertex detector to the drift chamber and the centre of the beam envelope have been known exactly. The effect of possible errors in the determination of the relative alignments were studied by giving both the track reconstruction program and vertex fitting program the relative (x,y) shifts incorrect by 150 μm and the relative rotation incorrect by 0.4 mrad. These incorrect values corresponded to approximately 1.5 and 4.0 standard deviation movements respectively when considering the accuracy with which the position of the real detector had been determined.

Similarly, the effect of an error on the position of the beam envelope centre was studied by randomly changing its position from event to event such that it lay within ± 200 μm of the correct position. These movements lay within about 2.5 standard deviations of the correct position when considering the accuracy of the beam spot determination for the real data.

The results of this study are shown in Table 10 for the PASS5 tracks and the three groups of Monte Carlo events. Again the times are in units of 10^{-13} seconds. The results from the FELIX tracks were similar.

TABLE 10

Measured Lifetime from Monte Carlo Events

Generated Lifetime	x-y Shift	Rotation	Beam Shift
0	0.3 ± 0.2	0.3 ± 0.2	0.4 ± 0.2
2.7	2.7 ± 0.2	2.7 ± 0.2	2.8 ± 0.2
5.4	5.1 ± 0.3	5.0 ± 0.3	5.1 ± 0.4

All reconstructed lifetimes are compatible with the generated values. Most importantly, the effect of giving an incorrect relative detector position or beam spot position to the track finding and vertex reconstruction programs did

not result in a significantly finite lifetime being found for events generated with zero lifetime.

6.8 LIFETIME MEASUREMENTS ON THE TAU DATA

6.8.1 Introduction

The method of extracting a lifetime from a set of events has been shown to work successfully in Monte Carlo studies. A similar analysis was then repeated using the real tau data. Particular attention was given to checking that the errors on the decay times were reasonable, and that a finite lifetime was not measured due to the resolution function having a mean offset from zero.

6.8.2 Vertex Fitting

The number of events with a reconstructed vertex was smaller than the number of tau events. Basically, there were three reasons: the vertex detector was not operational due to hardware problems, three tracks were not always reconstructed within the detector, or the vertex constraint program failed to find a vertex such that the increase in χ^2, $\Delta\chi^2$, was less than 5.0. The number of events remaining after each of these steps is given in Table 11 for FELIX tracks. Throughout this analysis with real data, the results from the use of FELIX tracks will be quoted as there are more events and consequently smaller errors.

TABLE 11

Number of Tau Events Reconstructed

	1+3 Topology	3+3 Topology
Tau Events	45	11
Events with Vertex Detector Operational	34	10
3 Track Systems	34	19
Vertices Found	26	15

The probability distribution P_χ that $\Delta\chi^2$ would have a higher value is shown in Figure 6.14. Although the error bars are large due to the small number of events, the roughly flat distribution across the whole range of P_χ shows that a reasonable estimate of the errors has been made. Figure 6.15 and Figure 6.16 show tau events in the vertex detector with the tracks constrained to a vertex. Figure 6.17 and Figure 6.18 show close-up views of the vertices of these events. The small solid cross represents the position of the beam spot. The horizontal and vertical lines that make up the cross represent a distance of 1 cm.

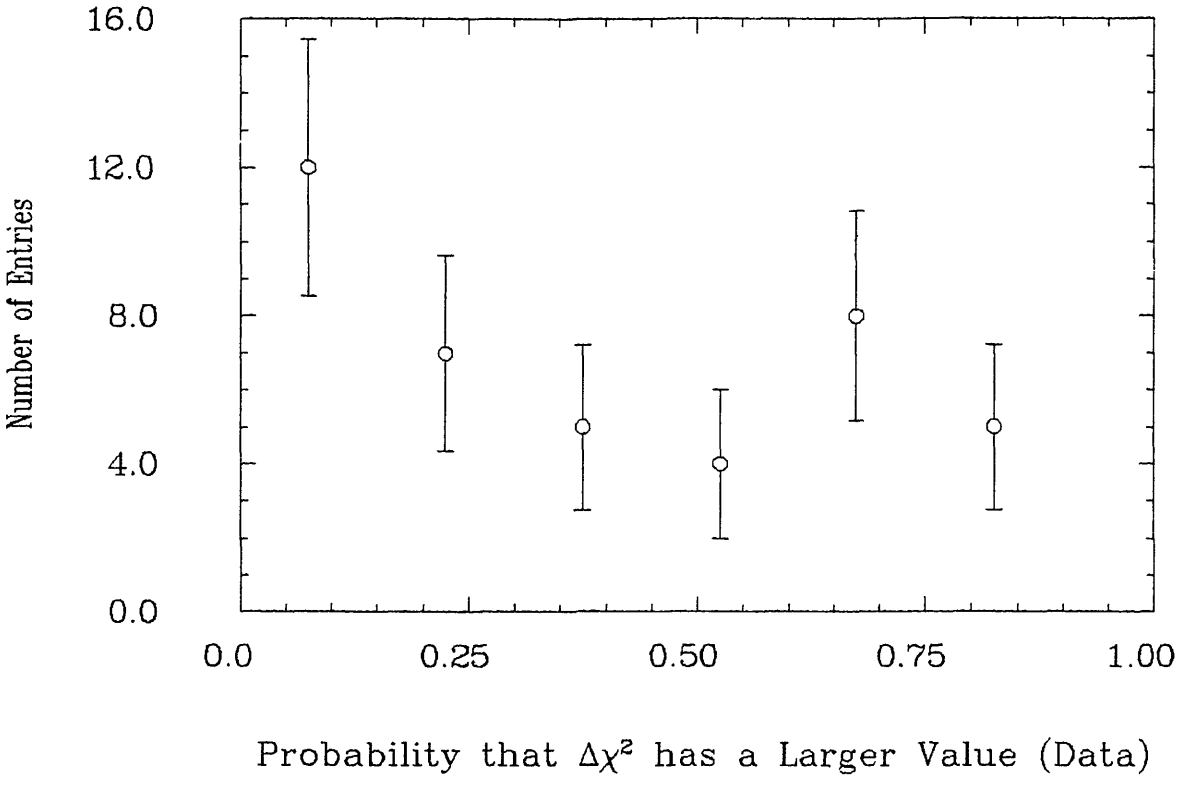

Figure 6.14: Probability that Vertex Fit has a Larger χ^2

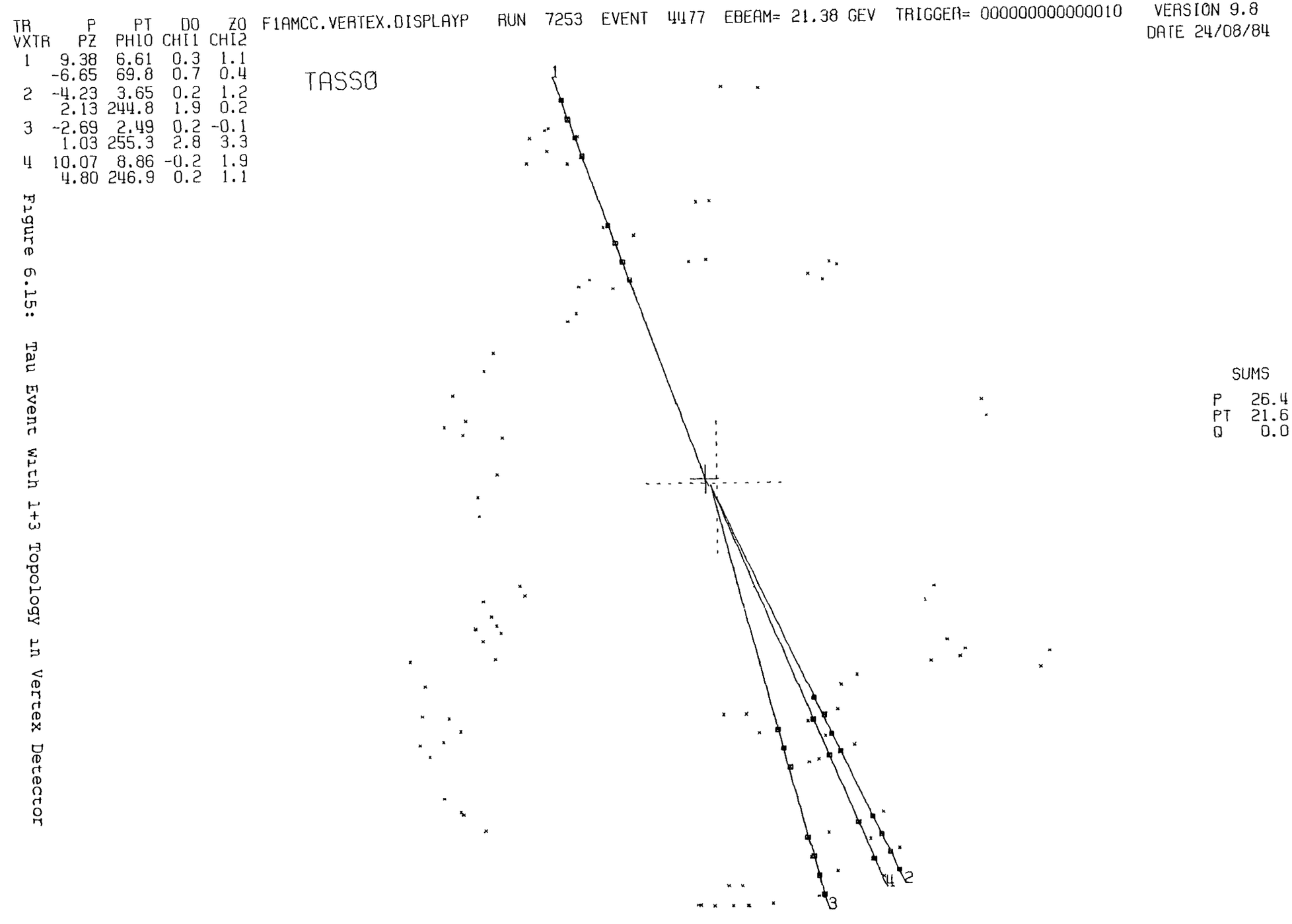

Figure 6.15: Tau Event with 1+3 Topology in Vertex Detector

Figure 6.16: Tau Event with 3+3 Topology in Vertex Detector

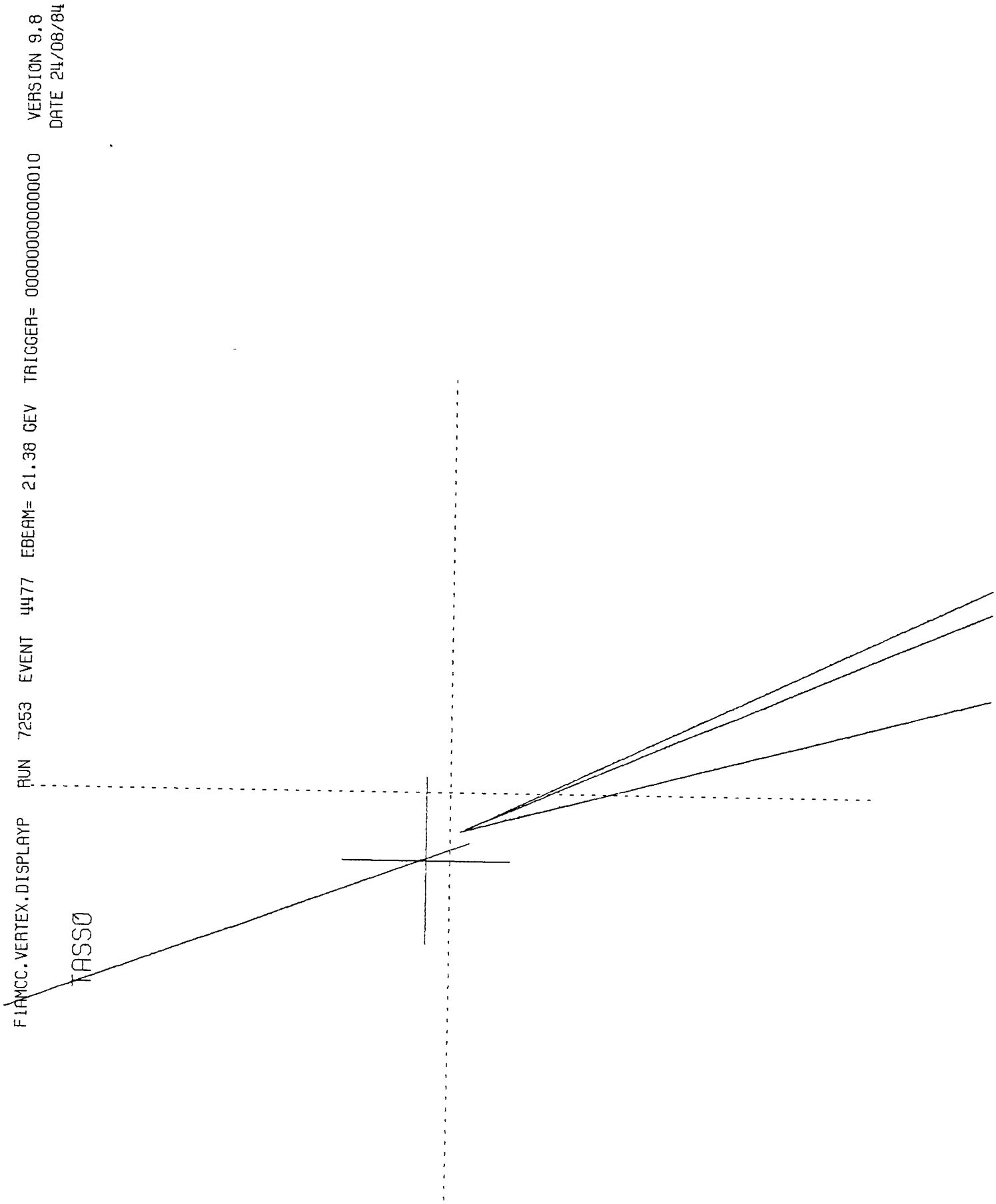

Figure 6.17: Close-up of Tau Event Vertex with 1+3 Topology

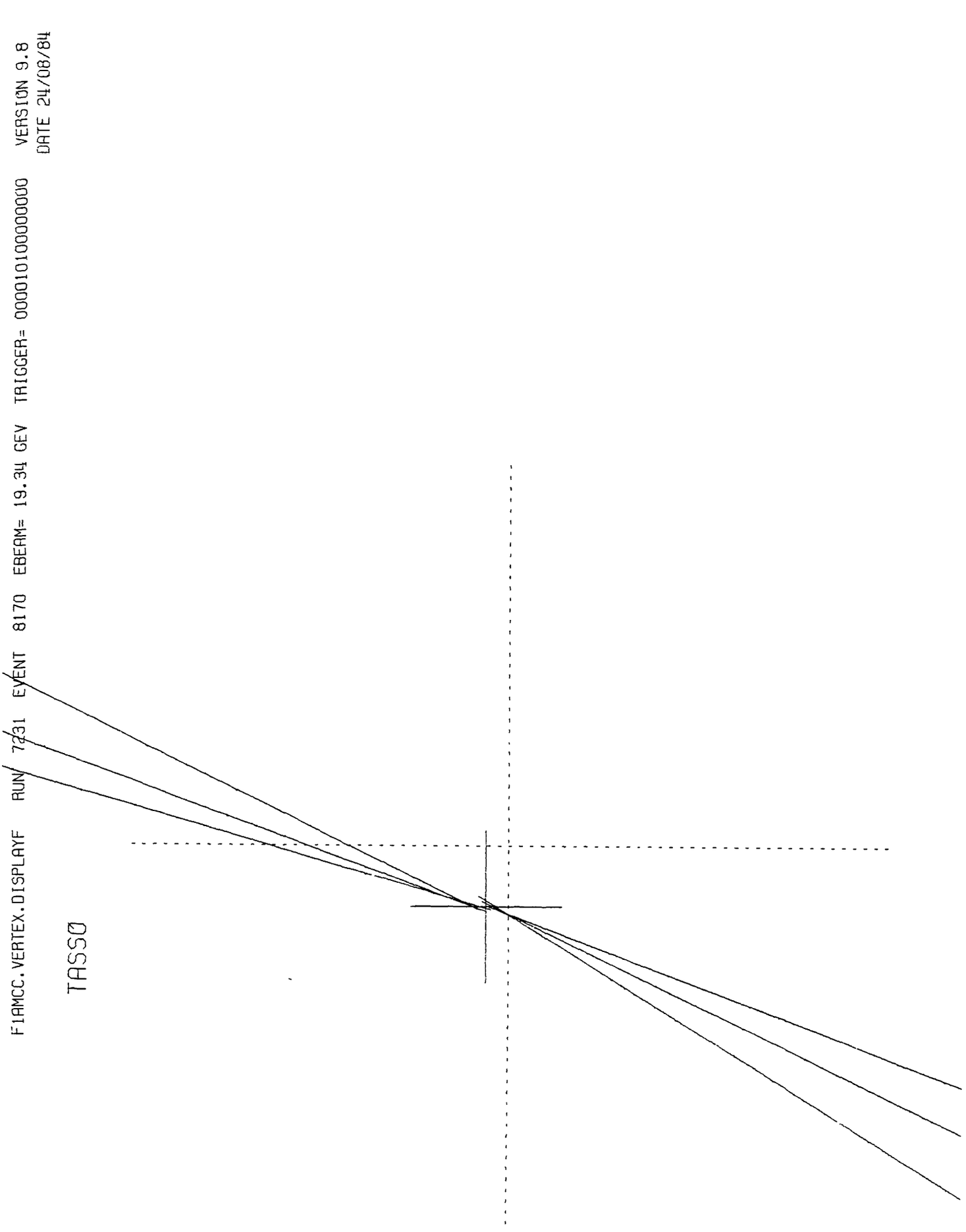

Figure 6.18: Close-up of Tau Event Vertex with 3+3 Topology

6.8.3 Likelihood Functions

As discussed earlier, the lifetime (τ) was the free parameter in a maximum likelihood fit to the lifetime distribution function, a convolution of a Gaussian resolution distribution and an exponential decay distribution. The measured decay time (t) and its error (σ) were calculated for each event and used as input parameters in the fit.

In this fit, the weight of each decay time depended on its error. To investigate the effect of giving all decay times equal weight, both the lifetime (τ) and the width of the resolution function (σ), which was now assumed to be the same for each event, were fitted as free parameters in the maximum likelihood fit.

So far, the resolution function has been assumed to be centred at zero decay time. To check for a possible offset in the resolution function, each decay time (t) was allowed to vary by a constant offset (μ). A maximum likelihood fit was performed with the decay time and its error as input parameters, the free parameters were τ and μ.

As a check that the errors calculated for each event were reasonable, each error was allowed to vary by a constant scale factor (k). A maximum likelihood fit was performed with the decay time and its error as input parameters, the free parameters were τ and k.

6.8.4 Data Results

After rejection of events with an error on the measured decay time greater than 9 x 10^{-13} s, 23 events with a 1+3 topology and 15 vertices from events with a 3+3 topology remained. This removed events with bad vertices, a visual scan of such events showed hits had been incorrectly associated within the vertex detector. Table 12 shows the lifetime found after these various maximum likelihood fits. All parameters, except k, are in units of 10^{-13} s.

The radiative correction to the measured lifetime has not been made on the data shown in the diagrams, but has been made on the times discussed in the results. The estimation of the 3.5 % loss in the mean tau energy due to radiation of photons in the initial state was discussed earlier.

The distribution of decay times for events with both topologies, 1+3 topology and 3+3 topology are shown in Figure 6.19, Figure 6.20, and Figure 6.21 respectively. The fitted curve was produced by keeping the lifetime found from the maximum likelihood fit fixed and fitting the resolution and normalization of a lifetime distribution function. The distribution of the errors on the decay times for all events are shown in Figure 6.22.

Figure 6.23 shows the likelihood function for all events as a function of lifetime. Figure 6.24 shows a contour plot of the lifetime against the width of the resolution function, Figure 6.25 shows a contour plot of the lifetime

TABLE 12

Results of Fits to Tau Data

Type of Fit	Input Parameters	Free Parameters
FELIX all events	t σ	τ = 2.7 + 0.7 - 0.6
FELIX 1+3 topology	t σ	τ = 2.2 + 0.8 - 0.7
FELIX 3+3 topology	t σ	τ = 3.6 + 1.4 - 1.0
PASS5 all events	t σ	τ = 2.7 + 0.8 - 0.7
All times equal in weight	t	τ = 2.1 + 0.8 - 0.7 σ = 4.8 + 0.7 - 0.6
Offset in resolution function	t σ	τ = 2.8 + 1.1 - 1.0 μ = 0.1 + 1.1 - 1.2
Errors scaled by constant	t σ	τ = 2.6 + 0.8 - 0.7 k = 1.1 + 0.2 - 0.2

against a possible offset in the resolution function and Figure 6.26 shows a contour plot of the lifetime against a possible scale factor in the errors on each decay time.

No significant offset has been measured in the resolution function. The errors used are reasonable as the error scale factor does not differ significantly from 1.0.

The value of the lifetime obtained is independent of whether the event was reconstructed using the PASS5 or FELIX track-finder, although the error when using PASS5 tracks is slightly larger due to the smaller number of events in the fit. When the events are split into the two different topologies; the lifetime obtained from the events with a 1+3 topology is smaller, and the lifetime obtained from the events with a 3+3 topology is larger than the lifetime found using all the events, by around one standard deviation. The fact that all but one of the events in the 3+3 topology data have positive decay times is noted, especially because of the large excess of these events over the number expected by theory and background calculations. However, due to the small number of events and the large errors, it is not possible to reject these events as taus.

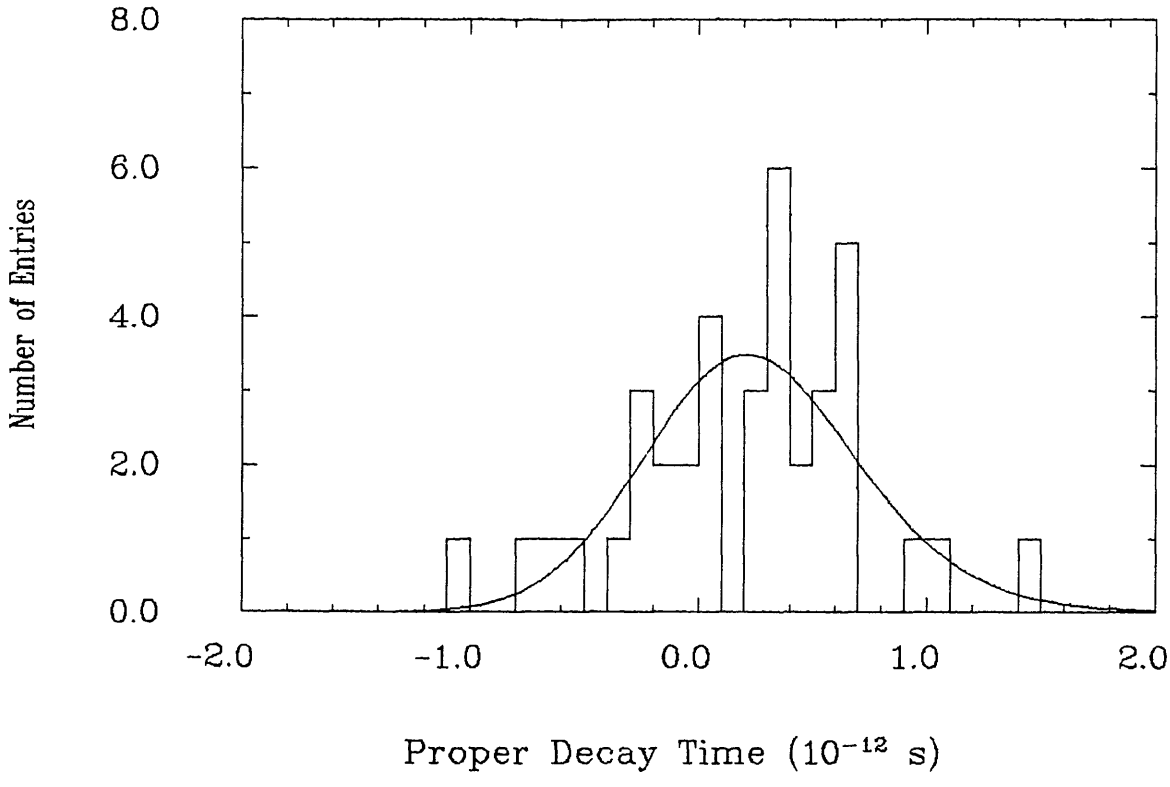

Figure 6.19: Tau Decay Times all Events

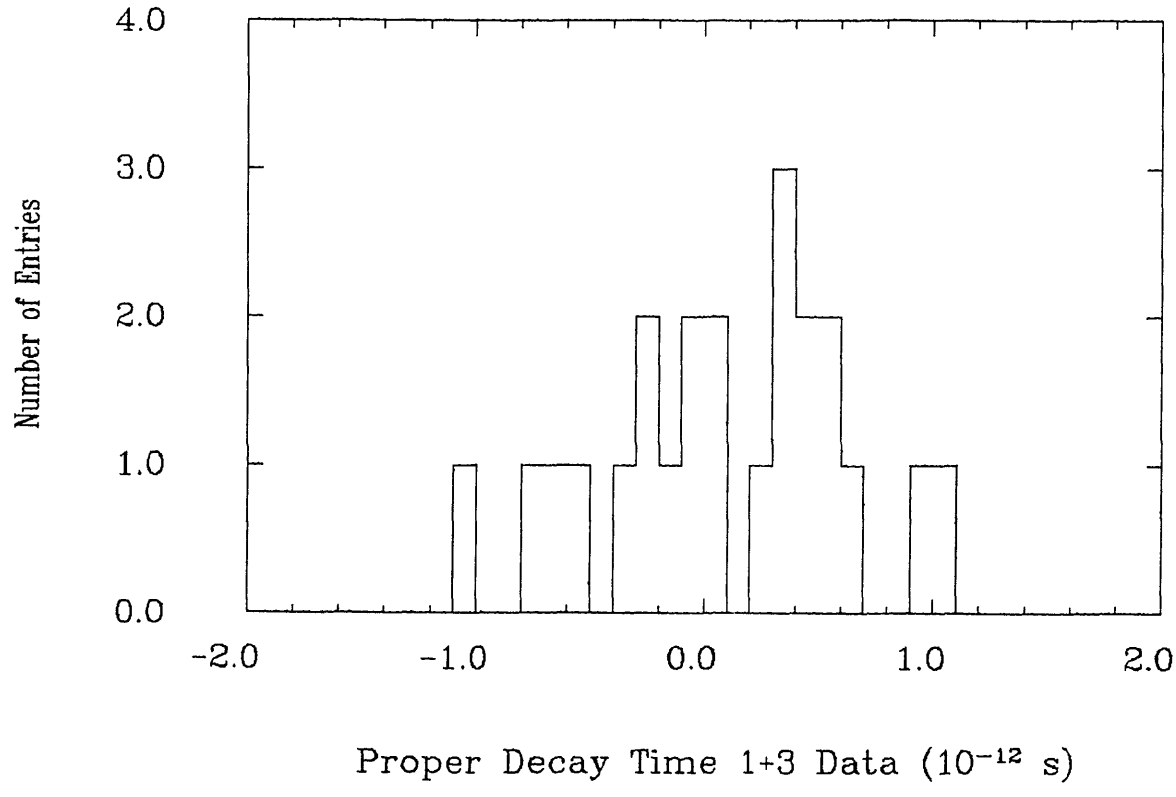

Figure 6.20: Tau Decay Times 1+3 Topology

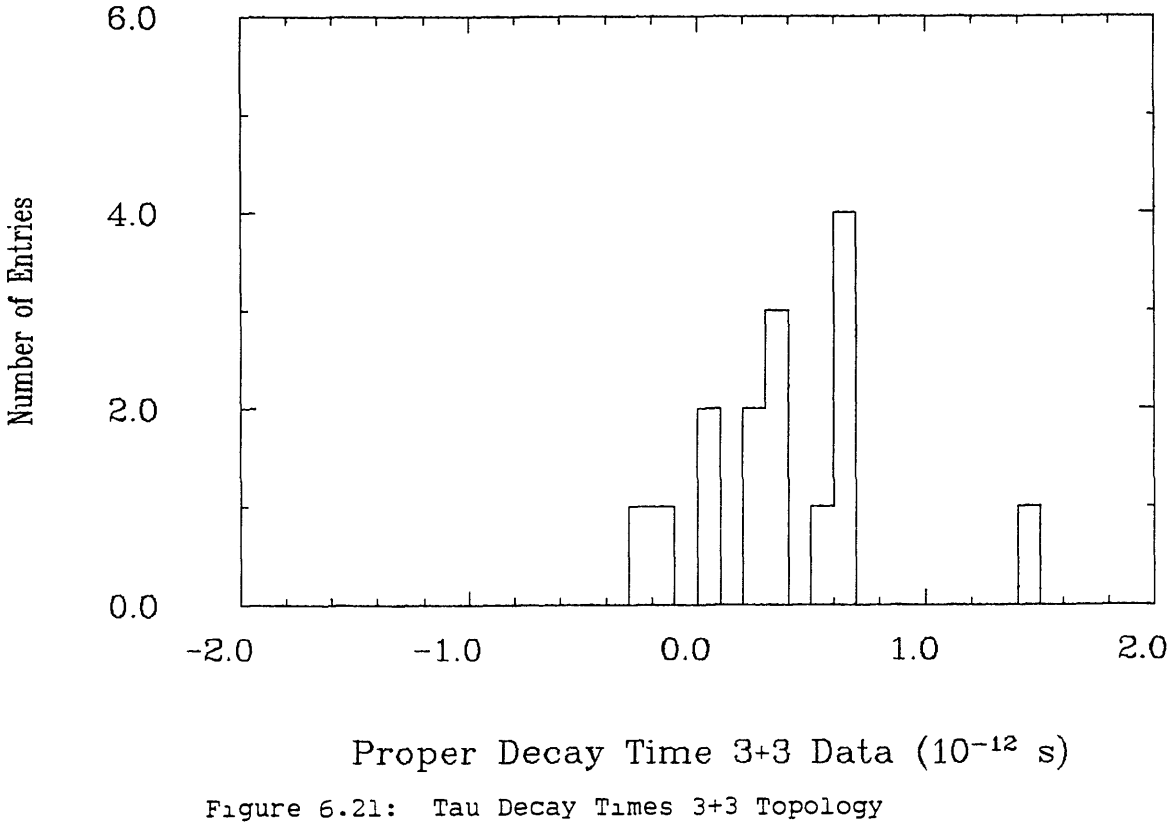

Figure 6.21: Tau Decay Times 3+3 Topology

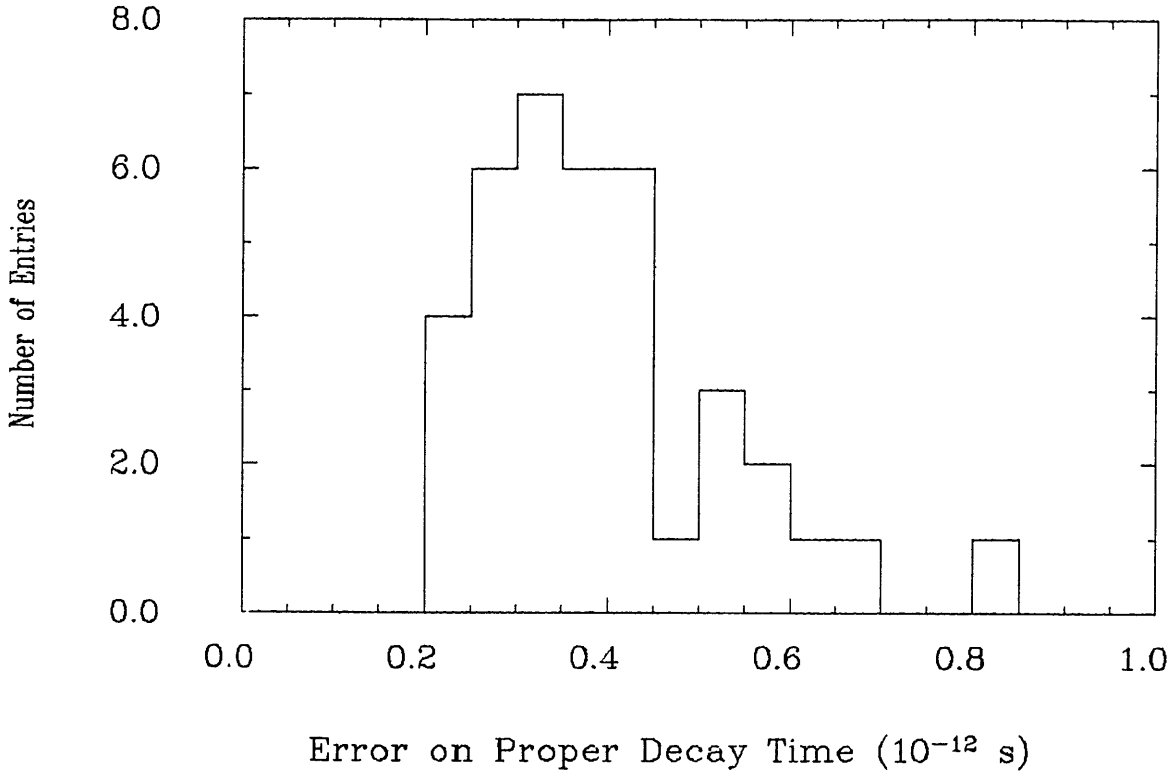

Figure 6.22: Errors on Tau Decay Times

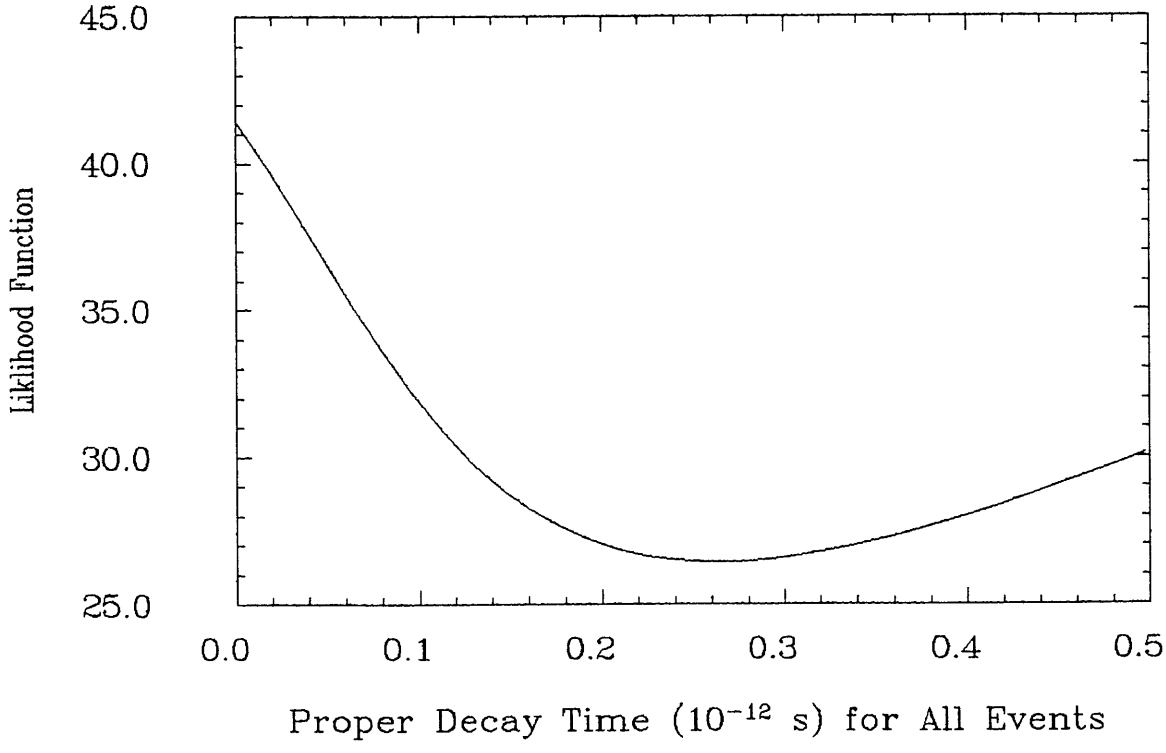

Figure 6.23: Likelihood Function for Lifetime Fit

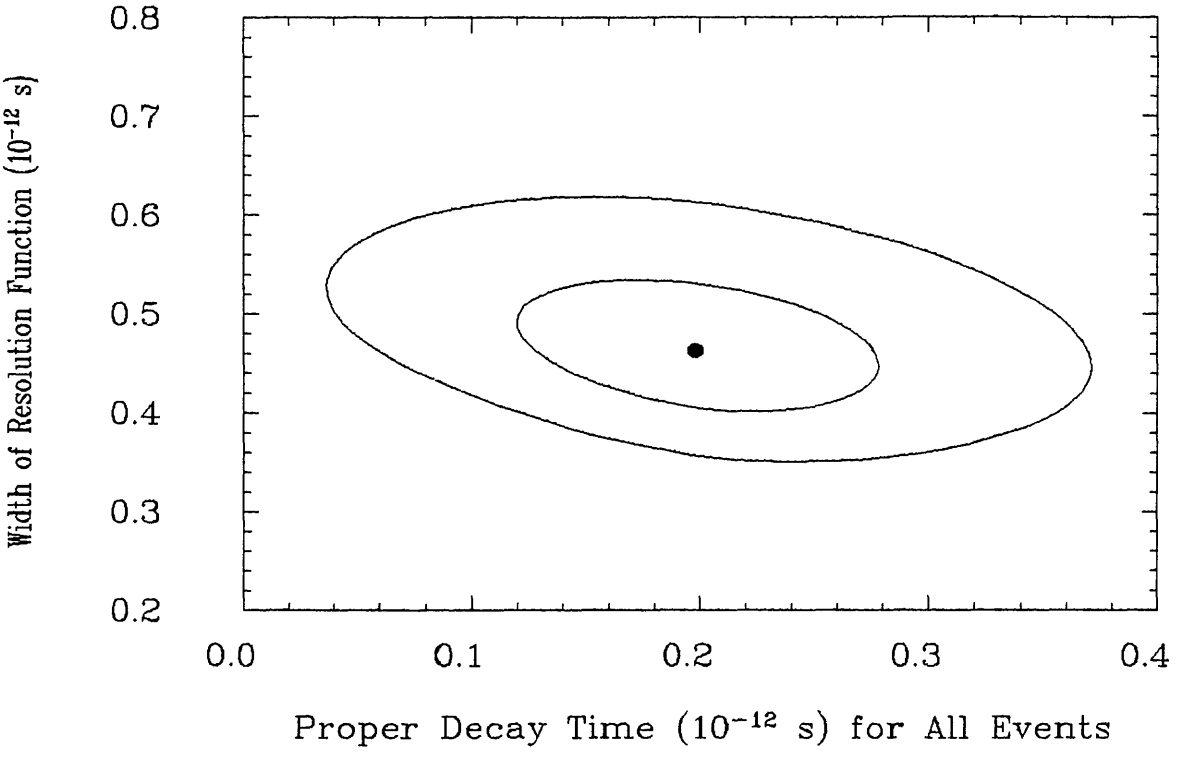

Figure 6.24: Contours of Lifetime against Resolution

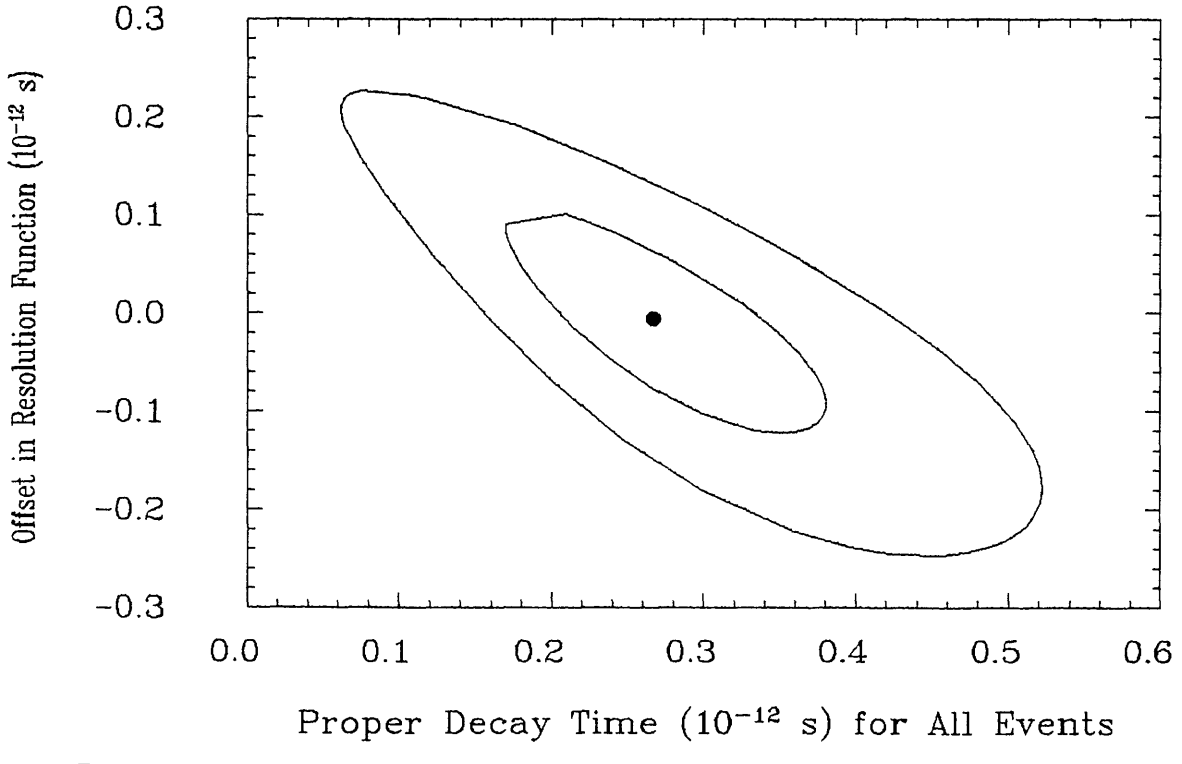

Figure 6.25: Contours of Lifetime against Resolution Offset

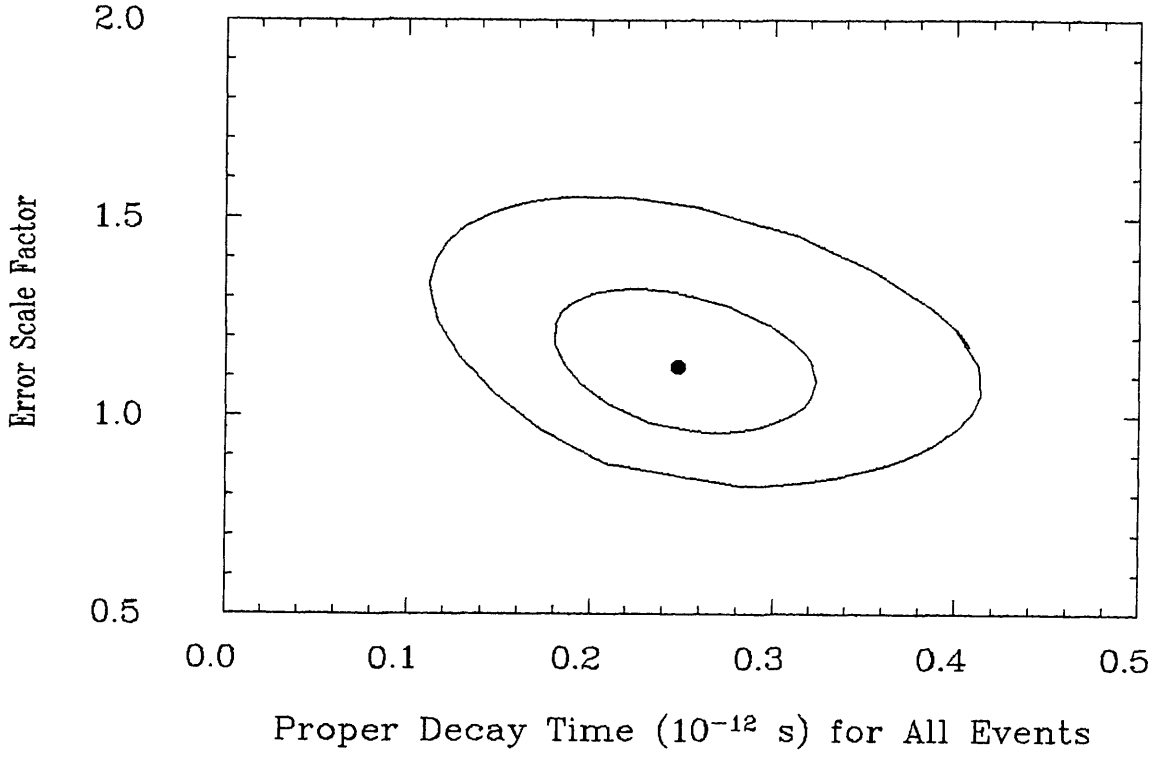

Figure 6.26: Contours of Lifetime against Error Scale Factor

6.8.5 Effect of Error in Detector or Beam Position

As previously done with Monte Carlo events, the track-finder was given the incorrect relative position of the vertex detector to the large drift chamber by 150 μm in the (x,y) direction, and by 0.4 mrad rotation about the z-axis. There was no change in either the measured lifetime or its error.

The skew position of the vertex detector was taken into account by refitting FELIX tracks in 3 dimensions before the vertex fitting procedure. The measured lifetime was not effected by making use of this refit procedure. The probable reason is that a skew detector position causes a displace-

ment of the reconstructed track from its true position that is proportional to z. As the z position of the vertex is almost zero, the skew does not effect the measured lifetime.

The beam spot position was moved randomly from the measured position from event to event within an envelope of ± 200 μm. There was only a slight change in the measured lifetime by -0.1×10^{-13} s.

6.8.6 Effects of Background Events

The background has been calculated to be 3.1 ± 0.9 events, two events were due to tau production via two photon collisions and one event was due to a low multiplicity hadronic event.

The measured lifetime of tau events produced via two photon collisions will be smaller than for other tau events due to their relativistic boost being smaller than the assumed value. The removal of the three events which have decay times closest to zero results in a measured lifetime of $(2.9 + 0.7 - 0.6) \times 10^{-13}$ s.

The lifetime of the hadronic event is uncertain, however, the effect of removing one event at random from the data sample resulted in changes in the fitted lifetime of $\pm 0.2 \times 10^{-13}$ s.

6.8.7 Systematic Errors

The systematic error on the lifetime needed to be estimated. The undetected neutral particles have been shown, through Monte Carlo studies, to have a negligible effect on the lifetime measurement. Small changes, comparable to the measurement errors, in the assumed alignment of the vertex detector relative to the large drift also have a negligible effect on the lifetime measurement.

The uncertainty in the correct position of the beam spot gave an error of $\pm$ 0.1 x 10^{-13} s. Due to the effect on the measured lifetime of the background events with zero or random decay time, an error of $\pm$ 0.3 x 10^{-13} s was estimated. In Monte Carlo studies, the vertex fitting procedure has been used to estimate the generated lifetime to within $\pm$ 0.3 x 10^{-13} s. The errors were shown in these studies to be known to within 7 %. The effect of underestimating or overestimating the errors on the decay time by 7 %, was to change the measured lifetime by $\pm$ 0.15 x 10^{-13} s.

A finite lifetime could have been measured due to the effect of an offset in the resolution function. No evidence for such an offset was found when both the lifetime and offset were simultaneously fitted to the data but the errors on these fitted parameters were large. An offset in the resolution function would have also affected the d_0 distribution of the horizontal and vertical tracks that were used to measure the beam size. A tracking bias would have resulted

in a shift from zero in the mean of this distribution or a depletion of events around small d_0 values. As no such effect was observed, errors from this source were assumed to be negligible.

All these errors were combined in quadrature give a systematic error of 0.5×10^{-13} s.

6.9 MEASURED TAU LIFETIME

In conclusion, the tau lifetime has been measured to be:

$$(2.7 \pm {}^{0.7}_{0.6} \pm 0.5) \times 10^{-13} \text{ s.}$$

where the first error is statistical and the second error is systematic. The result is in good agreement with the values measured by other experiments /24,25/. The result is also in good agreement with the lifetime of $(2.8 \pm 0.2) \times 10^{-13}$ s expected from theoretical predictions.

Using this measured value of the lifetime, the charged weak tau coupling constant relative to that of the muon is found to be:

$$G_\tau/G_F = 1.04 \pm {}^{0.24}_{0.28} \pm 0.20$$

This is consistent with G_τ and G_F being equal, and hence in agreement with lepton universality.

Appendix A

TASSO VARIABLES

The TASSO co-ordinate system, as shown in Figure A.1, was chosen so that the x-axis points towards the centre of PETRA, the y-axis points vertically upwards and the z-axis is in the direction of the positron beam.

The track in Figure A.2 has the following associated parameters:

d_0 is the distance of closest approach of the track to the origin in the x-y plane.

z_0 is the distance from the track to the origin in the z direction at the point where d_0 was measured.

ϕ_0 is the angle between the x-axis and the tangent to the circle at the point where d_0 was measured.

r_0 is the radius of the track circle.

θ is the angle between the track and the z-axis.

Q is the charge of the track charge (Q = ±1).

P is the track momentum.

P_t is the track momentum component in the x-y plane.

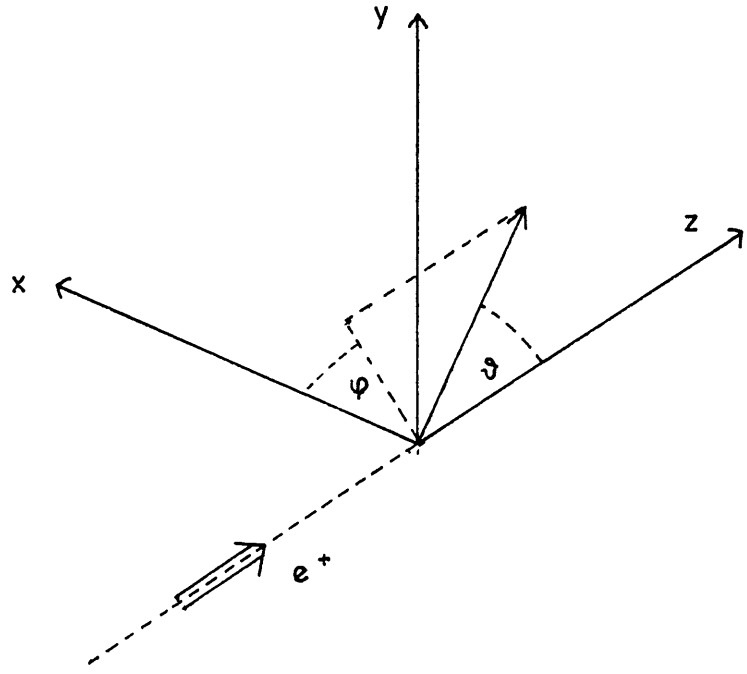

Figure A.1: The TASSO Co-ordinate System

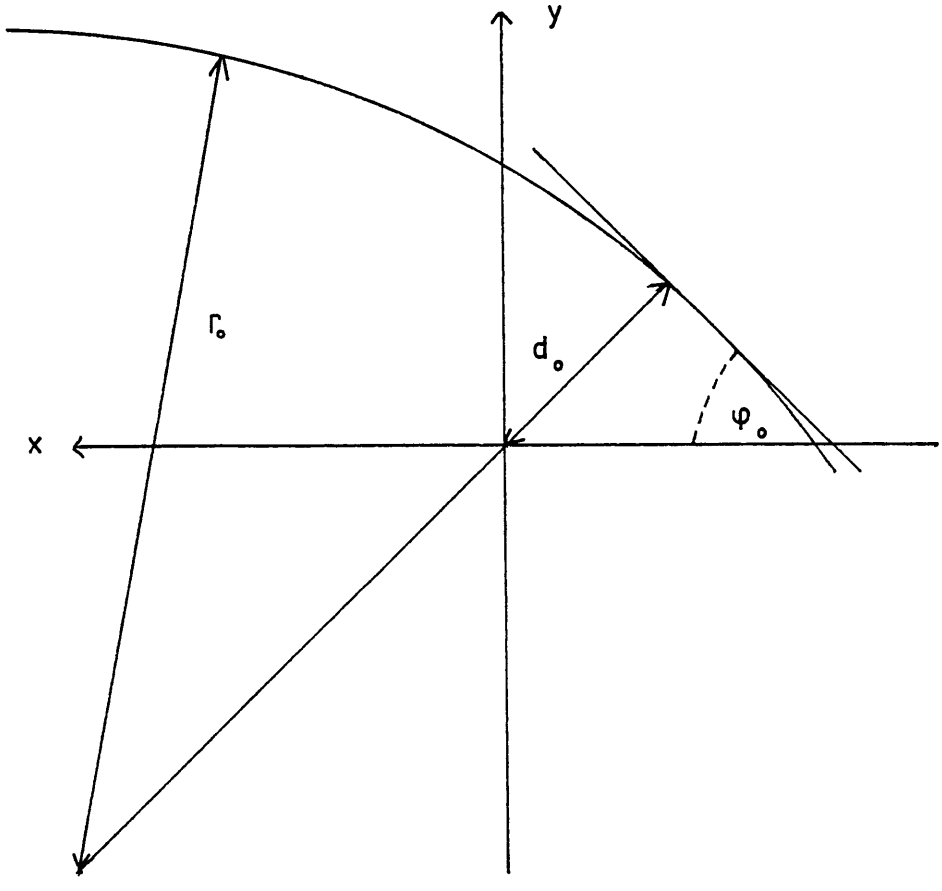

Figure A.2: Track Projected into x-y Plane

REFERENCES

1. C. Youngman, Ph.D. Thesis, University of London (1980), RL-HEP/T/82.

2. H. Boehner et al., DESY 80/27 (1980).

3. H.U. Martyn, TASSO Note 201.

4. H. Burkhardt et al., Nucl. Inst. & Meth. 184 (1981) 319.

5. K.W. Bell et al., Nucl. Inst. & Meth. 179 (1981) 27.

6. T.R. Wyatt, D.Phil. Thesis, University of Oxford (1983), RL-HEP/T/110.

7. TASSO Collab., R. Brandelik et al., Phys. Lett. 108B (1982) 71.

8. M. Ogg, D.Phil. Thesis, University of Oxford (1981), RL-HEP/T/89.

9. A. Jocksch et al., TASSO Note 298.

10. S. Jaroslawski, Nucl. Inst. & Meth. 176 (1980) 263.

11. D.R. Quarrie, RL-81-048 (1981).

12. D.G. Cassel, H. Kowalski, DESY 80/107 (1980).

13. H. Burkhardt et al., TASSO Note 190.

14. D.M. Binnie et al., DESY 84/60 (1984).

15. M.L. Perl et al., Phys. Rev. Lett. 35 (1975) 1489.

16. W. Bacino et al., Phys. Rev. Lett. 41 (1978) 13.

17. J. Kirkby, Proc. 1979 Int. Symp. Lepton Photon Interact. High Energies.

18. S.L. Glashow, Nucl. Phys. 22 (1961) 579;
A. Salam, Proc. Eigth Nobel Symp., p.367, ed. N. Svartholm, (Almquist and Wiksell, Stockholm, 1968);
S. Weinberg, Phys. Rev. Lett. 19 (1967) 1264.

19. J.D. Bjorken, S.D. Drell, Relativistic Quantum Mechanics, (McGraw Hill New York, 1964).

20. W. Bacino et al., Phys. Rev. Lett. 42 (1979) 749.

21. For Review see:
M.L. Perl, Ann. Rev. Nucl. Part. Sci. 30 (1980) 299.

22. Mark II Collab., C.A. Blocker et al., Phys. Rev. Lett. 49 (1982) 1369.

23. PLUTO Collab., G. Alexander et al., Phys. Lett. 81B (1978) 84;
DELCO Collab., W. Bacino et al., Phys. Rev. Lett. 42 (1979) 749;
TASSO Collab., R. Brandelik et al., Phys. Lett. 92B (1980) 199.

24. MARK II Collab., G.J. Feldman al., Phys. Rev. Lett. 48 (1982) 66;
MAC Collab., W.T. Ford al., Phys. Rev. Lett. 49 (1982) 106;
CELLO Collab., H.J. Behrend et al., Nucl. Phys. B211 (1983) 369.

25. MARK II Collab., J.A. Jaros et al., Phys. Rev. Lett. 51 (1983) 955.

26. TASSO Collab., R. Brandelik et al., Phys. Lett. 92B (1980) 199;
TASSO Collab., DESY 84/91 (1984).

27. F.A. Berends and R. Kleiss, Nucl. Phys. B177 (1981) 237.

28. B. Foster and S.L. Lloyd, SIMPLE Write-Up, Unpublished.

29. F.A. Berends, P.H. Daverveldt and R. Kleiss, contributed paper 5th Intern. Colloq. Lecture Notes in Physics, Vol.191, (Springer, Berlin, 1983).

30. B. Andersson, G. Gustafson and T. Sjoestrand, Phys. Lett. 94B (1980) 211.

31. A.J. Campbell, Ph.D. Thesis, University of London (1983), RL-HEP/T/117.

32. W. Schuette, TASSO Note 243.

33. A.G. Frodesen et al., Probability and Statistics in Particle Physics, (Universitetsforlaget, Oslo, Norway, 1979).

34. F. James and M. Roos, CERN Computer Centre Program Library Long Write-up MINUIT, 1977.

35. D.H. Saxon, RAL-84-044 (1984).

36. Particle Data Group, Rev. Mod. Phys. 52(1980) No.2 Part II.

37. G. Arfken, Mathematical Methods for Physicists, pg 295, (Academic Press, London, 1970).